

Lehrstuhl fuer Maschinen-und Apparatekunde

Theoretical and experimental studies on fracture mechanics of spices as model food material

Bhadravathi Shivaramaiah Sridhar

Vollstaendiger Abdruck der von der Fakultaeet Wissenschaftszentrum
Weihenstephan fuer Ernaehrung, Landnutzung und Umwelt
der Technischen Univeristaet Muenchen
zur Erlangung des akademischen Grades eines
Doktor-Ingenieurs
genehmigten Dissertation.

Vorsitzender: Univ.-Prof. Dr.-Ing. R. Meyer-Pitroff

Pruefer der Dissertation: 1. Univ.-Prof. Dr.-Ing. K. Sommer
2. Univ.-Prof. Dr.-Ing. W. Peukert

Die Dissertation wurde am 14.01.2005 bei der Technischen Universitaet Muenchen eingereicht und durch die Fakultaeet Wissenschaftszentrum Weihenstephan fuer Ernaehrung, Landnutzung und Umwelt am 03.03.2005 angenommen.

Acknowledgements

I place on record my deepest sense of gratitude to Professor Dr. Ing. Karl Sommer, for his interest in my work, valuable suggestions, constant encouragement and constructive criticism throughout the period of this work and for being Guide, advisor and mentor.

I wish to thank Professor Dr. Ing. Wolfgang Peukert, for having helped me to plan and restructure my work so that it would not go in a different direction.

I thank Dr. V.Prakash, Director Central Food Technological Research Institute for granting me permission and providing necessary facilities to carry out the research work.

I thank Professor Dr. Srinivasan for his guidance, interest, support and for the freedom with which I could plan and execute my research studies.

I am grateful to Dr. Ing. Gerhard Hauser for his constant moral support and for inspiring me to carry out research.

I am profoundly grateful to Dr. S.Divakar and Mr. B. Manohar for their open discussions and permanent interest in the work.

I thank Dr. Dastur for proof reading this thesis.

Finally, I wish to express my greatest gratitude to all colleagues of Central Food Technological Research Institute, Mysore who contributed to this work by their interest and helpful discussion.

Chapters	Contents	Page
1.	Introduction	1
2.	General background	3
2.1	Morphology and structure of Turmeric	3
2.2	Size reduction methods of spices	4
2.2.1	Conventional grinding	5
2.2.2	Cold grinding	7
2.3	Fracture phenomena: Review	8
2.3.1	Fracture mechanism	8
2.3.2	Thermal effects	16
2.4	Measuring fracture resistance	19
2.4.1	The Fracture surface energy – Fundamental concept	20
2.4.2	The Plane strain fracture toughness	21
2.4.3	The Strain energy release rate	26
2.4.4	The Maximum principal stress	28
2.4.5	Thermal effects characterization	29
2.5	Finite elements in fracture mechanics : Review	30
2.5.1	Crack tip singularity modeling	31
2.5.2	Fracture prediction	31
2.5.3	Crack extension simulation	34
2.5.4	Temperature distribution	34
3.	Objectives and scope of the work	36

4.	Material and methods	38
4.1	Materials	38
4.2	Methods	40
4.2.1	Size reduction mills	40
4.2.2	Particle size and shape analysis	45
4.2.3	Engineering properties	47
4.2.4	Thermal effects prediction	58
4.2.5	Parametric Finite element studies	59
5.	Results	72
5.1	Engineering properties of turmeric	72
5.2	Finite element fracture mechanism predictions	90
5.3	Fracture under different size reduction mills	99
5.4	Thermal effects prediction of fracture particulates	111
5.5	Specific energy consumption	128
5.6	Liquid nitrogen consumption and throughput	128
5.7	Quality evaluation	129
5.8	Development of scale-up procedure	134
6.	Discussion	141
6.1	Engineering properties of turmeric	141
6.2	Finite element prediction of fracture mechanism	142
6.2.1	Effect of interface bond strength	142
6.2.2	Effect of residual stress state	144
6.2.3	Effect of fiber orientation	144
6.3	Fracture mechanism under different size reduction methods	147
6.4	Thermal effects of fracture particulates	154

6.5	Specific energy consumption	155
6.6	Liquid nitrogen consumption and throughput	156
6.7	Quality evaluation	157
7	Summary	158
8	Appendix A	166
9	Appendix B	175
10	Appendix C	178
11	Symbols and abbreviations	181
12	References	190

1. Introduction

Food materials are difficult to grind because of their varying proportions of moisture, fat and fibrous structure. Practically every solid food material undergoes size reduction at some point in the processing cycle. The main reason for unacceptable food quality of food products especially spice powders are due to non uniformity in shape and size distribution, flavour and colour. Grinding forms a very important unit operation especially in the post harvesting of spices requiring special attention as it involves additional problems of volatility and loss of aroma from essential oils, apart from obtaining smaller particle sizes. Since particle breakage represents an elementary process in comminution a scientifically based approach could only be possible with a comprehensive knowledge of this process through the investigations of aspects such as fracture mechanism, crack propagation, stress intensity distribution, thermal effects, size reduction under different conditions and similar problems relating to particle breakage behaviour (Rumpf, 1965, 1990).

In the 19th century spices were eagerly sought and the wealth and power of nations were involved in the control of the spices trade. Despite their economic importance in the world trade (worth \$ 1.5 billion), they have not received the attention they so richly deserve, notably in their processing and quality aspects. Value added products such as ground spices, mixes, oleoresins and spice oil extracts have vast industrial applications and with improvements in processing, could improve their share in the market.

Sizes and shapes of particles formed during size reduction processes depend on crack growth or how fracture path run through the original stressed material. Some of the key factors that influence the fracture mechanism are mechanical and physical properties of the product, their behavior under ambient and low temperature conditions and geometry and dimension of the product.

The present study investigates the effects of controllable parameters on the fracture mechanism, crack propagation and particle shape formation during size reduction under ambient and cryogenic conditions of turmeric (*Curcuma Longa*). The approach taken combines experimental mechanical property determinations,

quality evaluation including shape and size characterization and fracture surface analyses with finite element structural modeling.

Experimental studies give valuable, analytically indeterminable information about the possible effects of different comminuting mechanism on the fracture behaviour of the spice, turmeric. However events of the fracture process must be inferred from the fracture surface. It is generally not possible to isolate the individual effects of each structural parameter. In comminution, one can proceed from the fact that fractures start from structural defects at the particle surfaces and the conditions of stable or unstable crack propagation resulting in either ductile or brittle fracture. Since unstable crack propagation occurs both with and without previous stable propagation during comminution of the most of the solid food materials (Bluemenauer und Pusch, 1993) such as spices, grains and cereals, the present study is confined to impact-fracture behaviour (Rumpf, 1990).

The goal of the finite element modeling is to understand the finer mechanical interactions between the growing crack and constituent material properties of turmeric. The mechanical modeling allows the determination of the effects of individual parameters such as morphology, orientation and properties of the fiber and the strength of the interfacial phase on the fracture processes. Knowledge gained from such studies can be used to predict fracture mechanism in a given food material and efficiently design and optimize processes of food size reduction systems.

2. General Background

2.1 Morphology and chemical composition of turmeric

Turmeric is dried rhizome of *Curcuma Longa* L. (Zingiberaceae), an herbaceous plant native to tropical South East Asia. Its cultivation extends from India to Bangladesh, Indonesia, Srilanka, Taiwan and part of China. Turmeric grows best in a tropical humid climate. It is propagated by small portions of the rhizomes which are planted at about 30cm intervals. The plant grows to a height of about a meter, with long and broad light green leaves. The yellowish –white flowers are borne on spikes arising from leaf tufts. No viable seeds are obtained from the fruits.

The primary and secondary branches of the rhizomes are known as “fingers”, while the thickened portion of the rhizome represents ‘bulb’. The West Asian countries prefer the bulbs, while the Americans and Europeans markets take “fingers”. Dried turmeric usually has a low moisture content of about 6%. It gives a metallic sound when broken. The “fingers” are broken and milled to a fine powder (200-500 microns) for use as spice .

World production of turmeric estimated to be about 2,60,000 tons, of which India alone accounts for only 80 percent, but only some 20,000 tons of turmeric are exported from India, the rest being consumed within the country (Thomas,2000).

Turmeric is fibrous and starchy, has a deep yellow color and pungent flavor. It contains, on average 6 % moisture, 6% protein, 3.5% fixed oil, 4.5% volatile oil, 50.4% crude starch, 3% fiber and curcumin 3.5%. Standards require ground turmeric to contain not more than 7% total ash, 1.5% acid insoluble ash and 60% starch. More than 50% of the oil is composed of a mixture of sesquiterpene ketones, known as turmerone or tumerone and about 25% sesquiterpenes like zingiberene. Other constituents reported include α -phellandrene (~1%), cineole(~1%), sesquiterpene alcohols (~ 6-9 %), and traces of alpha and gamma atlantone. Dihydroturmerone, sometimes seen in the oil, is

not a natural component but is formed as an artifact. (Max, 1992; E.O.A.⁴ specification 1995).

The most valued constituent of turmeric is its yellow pigment, curcumin. The colouring matter is extractable by solvents like methanol, ethanol, acetone and dichloroethylene but not by petroleum solvents. Ground turmeric (size: ~200 – 425 microns) extracted with acetone by cold percolation gives high yields of extractives with high curcumin content. Turmeric oleoresin is an orange red product, consisting of an upper oily layer and a lower crystalline layer. The non pungent residues present include some waxes and resins which have not been studied in detail (Govindarajan, 1990;Khanna,1999).

Uses

Turmeric is consumed mostly in the ground form. As a natural coloring agent, turmeric and its oleoresin are quite popular in the food industry. They are mainly used in the pickle industry and in other products where a rich yellow color is desirable, such as processed cheese and mustard paste. Turmeric is an essential ingredient of all types of curry powder and paste. It is used in flavoring of poultry, seafoods and rice dishes. It is estimated that 40 – 45 tons of turmeric oleoresin are produced annually. Various turmeric oleoresin based products are marketed in different grades of color strength (Max, 1992).

2.2 Size reduction methods of spices

The true value of most spices comes from their inherent etheric oils. Most spices have their characteristics aroma and therefore their true value as spices is due to enclosed etheric oils that constitute the ingredient of spice. Etheric oils are metabolic substances which are not recycled in the metabolic process. They are excreted by the plant or deposited on certain plant parts like exogen and endogen oil containers. These oil containers are oil cells or intercellular containers of ball or elongated shape out of which in most cases can only be obtained after crushing. This is the reason why almost all spices are marketed in a ground state.

The main aim of grinding in particular spice grinding is to obtain smaller particle sizes, with good product quality in terms of flavour and colour. Many studies have been devoted to investigation of the size of particles resulting from comminution, but studies including particle shape formation during comminution has received very little attention, despite the improvements in imaging and computing techniques and the importance of particle shape to the technological properties of collections of comminuted particles. The effect of particle size and shape on technological properties is no less pronounced when the comminuted particles are food products or of biological origin. In creating fiber boards, if density is maintained at a constant level the shape of comminuted wood particles dictates the breakage load of the fiberboard (Otani et al., 1995). The capacity of particulate foods to disperse upon wetting (a desirable attribute in “instant” food powders) is also dependent on particle shape (Palmowski, 2000). Storage and flow ability problems of foods and foodstuffs are strongly influenced by the shape of comminuted particles (Seville et al., 1997), a prime example being the shape difference between particles created from milling of hard and soft wheats. The irregular shape of soft wheat particles hinders flowability, lowering flour production capacity when milling soft wheats, and so increasing unit costs (Nussabaumer, 1990). Certain shapes and sizes have also been known to concentrate energy inside a food material much like an optical lens, concentrate light waves, while other shapes are known to have variations along the edges and corners of foods (Datta, 1990).

2.2.1 Conventional grinding

The optimum size of the grind for each spice depends on its end use and accordingly the conventional methods normally employ either a hammer mill (coarse grinding), plate mills (domestic use) or pin mills (fine grinding). Table 2.1 gives a brief list of size reduction mills used in food processing (Kukla, 1991). The particle size may vary from 850 microns to 50 microns of soft to medium-hard materials according to the standards of comparison of Mohs scale between 1 to 6 (Rumpf, 1990).

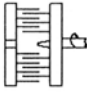
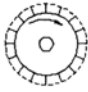

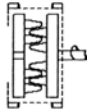
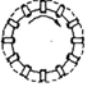
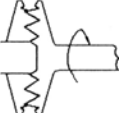
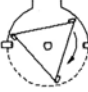
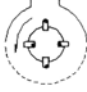
Type of equipment	Schematic	Method of size reduction	Peripheral speed (m/s)
Pinned Disk Mill		Impact	80 - 160
Blast Mill		Impact	40 - 110
Wing Beater Mill		Impact and shear	50 - 70
Disk Beater Mill (Lug beater)		Impact and shear	70 - 90
Hammer Cage Mill		Impact	70 - 90
Toothed Disk Mill		Abrasion and shear	5 - 16
Cutting Granulator		Section	5 - 18
Hammer Mill		Impact	40 - 50

Table 2.1: Size reduction mills used in food processing

During conventional grinding that is grinding without cooling the spices, the temperature increases to over 90°C can occur in fast rotating mills which leads to substantial losses in light evaporative etheric oils which leads to loss in quality. In an effort to decrease the loss in etheric oils by using cooling agents, an indirect water cooling system has been developed. The indirect cooling methods have not achieved the desired expectations since cooling is limited to machine parts only and oil losses remained high (Strasser, 1995). Conventional grinding with slow rotating roller mills, loss of etheric oils are low but results in lower production rate. Also these conventional methods suffer from various disadvantages like: (i) low efficiency (ii) not suitable for heat sensitive, high fat content and fibrous materials (iii) gumming of grinding walls and sieves resulting in frequent stoppage of mill for cleaning (iv) reduction of grinding rate (v) consumption of enormous energy especially during spice grinding (Roberts, 1998).

2.2.2 Cold grinding

Recently, low temperature grinding of spices using liquid nitrogen has achieved increasing importance. Nitrogen is a colourless, odourless and tasteless gas which is not specially reactive to other elements. Nitrogen accounts for 78.1% by volume of the surrounding air and the fact that we live in this atmosphere proves its non-toxicity. With substantial cool down, this liquid nitrogen can be liquified (it boils at atmospheric pressure at – 195.8°C and has a specific gravity of 0.808 kg per litre). If heat is applied to liquid nitrogen (evaporative heat 38.8 kcal/kg) it evaporates and increases its volume approximately 700 times. That is out of one litre of liquid approximately 700 litres of gas is obtained (Schaub, 1993). Most of the difficulties and degradations experienced in conventional grinding are overcome by grinding spices in liquid nitrogen (Pruthi, 1987). Some of the advantages of cryogrinding are: (i) reduced oxidation of spice oils and increased stability due to pasteurizing effect on spices (ii) extreme fine grinding due to brittleness and fine grinding of difficult materials (iii) more uniform dispersal of flavour, reduced visual speckling and settling rates in liquid preparations (iv) increased throughput and reduced grinding power

consumption (v) reduced loss of volatile oils and increased flavour strength (vi) reduction in microbial load (vii) lower cost of powder when the flavour strength is taken into account (viii) absolute control of particle size, shape and distribution (Schaub, 1995). A schematic view of the cold grinding is shown in Fig.2.1.

2.3 Fracture phenomena: Review

2.3.1 Fracture mechanism

The origin of fracture can be understood as a crack propagation ranging from submicroscopic to macroscopic dimensions under the action of stresses generated by external forces (Rumpf, 1965; 1973;1990). Unless existing flaws (structural defects) or micro-cracks at the particle surfaces are available for the beginning of a fracture, submicroscopic crack nuclei can form as a result of local slip mechanisms (dislocation motion) during mechanical stressing (Blumenauer und Pusch, 1993). This stage is referred to as crack formation. Crack initiation is the transition from resting to a propagating crack followed by the growth of a crack or crack propagation to end up finally with the fracture (Blumenauer und Pusch, 1993). A stable crack propagation occurs under continuous external energy supply and results in a macroscopic ductile fracture where as an unstable crack propagation occurs under continuous transition of elastic deformation energy, which has been stored in the solid body during stressing, into surface energy of the fracture areas resulting in macroscopic brittle fracture. Unstable crack propagation can occur both with and without previous stable crack propagation. (Schonert, 1995). Crack propagation is also influenced by the type and rate of stress, temperature and shape of the body in which the fracture phenomena takes place (Blumenauer und Pusch, 1993).

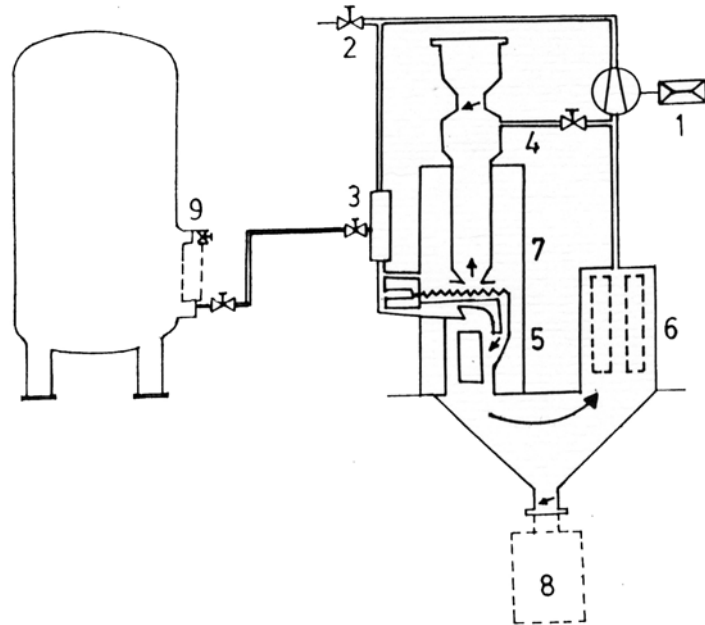


Fig. 2.1: A schematic view of cold grinding system

1. Blower
2. Nitrogen outlet
3. Liquid nitrogen evaporator
4. Refrigerated hopper
5. Mill
6. Filter
7. Screw feeder
8. Product container
9. Tank for liquid nitrogen

A particle fractures when the internal molecular binding forces are overcome to an extent sufficient to admit a certain minimum depth of cleavage (or “splitting”). The major break-through develops from extension of this initial minor cleavage (Schonert, 1993). The theoretical fracture stress σ_{th} required for overcoming the atomic bonding forces can be determined on the assumption of ideal lattice structure (Blumenauer und Pusch, 1993) as :

$$\sigma_{th} = \sqrt{(E \gamma_A / a_0)} \quad (2.1)$$

where a_0 = lattice constant, E = Young’s modulus, γ_A = specific surface energy

Professor Rumpf has classified mechanical cleavage inducement systems into three basic types: a) Compression shear stressing involving crushing between the rigid faces (e.g. hammer and anvil, nutcracker plier etc.), (b) Impact stressing involving fracture by concussion with a single rigid face (e.g. by dashing the material against a wall or floor) and (c) Shearing the material in a viscous stream (e.g. shredding by swirling).

The theoretical force or power required to achieve the minimum essential cleavage is actually very large indeed but fortunately most materials fracture after expenditure of as little as one-tenth or even one-hundredth of the theoretically necessary energy (Blumenauer und Pusch, 1993). The cause is that truly flawless materials are very rare. When there is a flaw in the structure of a particle, cleavage is induced a great deal more easily. With regard to stress distribution these flaws are loci of inhomogeneity (notches, primary cracks). Here the local stress intensities are several times higher than the mean values of stresses in the solid body. The fracture therefore start at these loci of weakness and propagate from there (Rumpf, 1990). The stress increase occurring at flaw can be calculated on the basis of the notch stress theory (stress intensity concept of fracture mechanics). The smaller the particle size attained at any time, the lesser the probability of a flaw in the remaining unfractured pieces. Hence the power requirement for further cleavage increases sharply as the particle size comes down. There must inevitably come a time when the force available for initiating cleavage is equal to or less than the force required, after which there can be no further reduction of particle size (Rumpf, 1990).

Fundamentally, in the process of comminution, a particle is not stressed up to the breakage point, but is continued on the fragments. A distinction has to be made between these two. Data related to primary breakage describes particle behaviour in terms of material testing and the post breakage relates the particle breakage to the comminution. A particle can be stressed either isolated or together with others in a particle layer or bed (Rumpf, 1990). The spectrum of spatial arrangement of particles is governed by single particle stressing and interparticle stressing. (Schubert and Hoberg, 1997). The difference between impact and non-impact breakage is that in impact breakage a reduction ratio is a function of energy imparted to the particle (impact speed) but in compression breakage, the amount of imparted energy is a function of a reduction ratio determined by the smallest gap between the crushing surfaces. (Rumpf, 1990). Spatial arrangement differs strongly depending upon brittleness. All these factors are strongly influenced by the feed particle size which in turn depend on the particle strength, shape and the absorbed specific energy during the post breakage stage and in interparticle breakage. Hence it is not possible, in principle to apply data of coarse particles to finer ones based on geometry only on the whole except within a limited size range (Schubert and Hoberg, 1997).

The crack pattern is determined by the stress field, which depends on the homogeneity and the deformation behaviour of the particle. Both of these change with the particle size (Schonert, 1995). So it can be understandable that the breakage function or the fragment size distribution depends on particle size and energy absorption and cannot be expressed in principle by one normalized master function. They become broader with increasing particle size and energy. The shape of the particles depends on material and mode of stressing. The breakage function can be expressed by a mixture of truncated logarithmic normal distributions (Senna, 1990; Schoenert, 1997).

Breakage probability has been found to be a measure of the strength of the material for that particle geometry and those loading conditions, and hence it would be also expected that the breakage probability would be related to the energy required for actual breakage that is the comminution energy

(Goepel,1992). Breakage probability within an assembly of particles increase with the number of contact points per particle up to a limited number of the order of ten. If more than this, the breakage probability decreases and the greater is the tendency for cracks to run near the periphery of the solid (Schubert, 1993). Peukert (2001), illustrated an approach to describe the interaction of material and machine by differentiating them for comminution. Breakage function describes the size distribution of fragments without taking into account the amount of undestroyed particles. Since similar distribution of cracks lead to similar distribution of fragments, the breakage function should be similar if the grinding takes place at a constant particle size and strain energy per unit volume of the particles (Weichert, 1992).

Schoenert (1993) have shown that there is a marked increase in the work of crushing related to mass as the size decreases, indicating increase in particle strength and an increase in the relative volumes of the contact zones with smaller particles. The crack can propagate only when a very high energy concentration exists at its tip. To obtain a crack, fine particles of high strength need to be stressed repeatedly for accumulating enough energy in the residual field around the inelastic deformation caused by each stress (Reichardt, 1994; Steiss, 1994). The particle strength here is referred to, as the quotient of the force acting on the particle at the breakage point divided by a nominal particle cross section. Because of the irregular shape of real particles and inelastic effects, the stress field cannot be calculated, but assuming contact area as a certain fraction of the particle cross section leads to an estimation of the same (Schubert and Hoberg,1997).

The product from any mill always contains a range of particle sizes (Rumpf,1990), since the size distribution tend to change as the grinding proceeds. Many studies have been devoted to investigations of the particle sizes resulting from comminution (Dominique et al., 1993; Schoenert, 1994;Seville et al., 1997;Kaye,1997).There are many averages which can be defined for a size distribution, each designed to represent it by a single figure. The average,

ofcourse gives no guide to the distribution spread. There are several definitions of mean particle size and their general form may be written (Schoenert, 1994) as:

$$g(\bar{x}) = \int_0^{\infty} g(x)f(x) dx \quad (2.2)$$

where $f(x)$ is the frequency distribution by number or density distribution by length, surface or mass and $g(x)$ is a particular function of particle size.

If no mathematical function for a distribution is known, the particle size distribution information can be tabulated or presented graphically using either cumulative distribution curves or frequency distribution curves. However it is much easier to handle mean sizes from analytical functions using modern computer techniques and hence fitting of mathematical expressions to size distribution curves is becoming increasingly important. There exists a wide range of mathematical functions which have been used to describe size distribution data such as Rosin-Rammler-Bennet (RRB), Gaudin-Schumann and log-normal distribution equations (Prasher, 1987).

The definition of particle shape is complex, since the general term 'shape' implies two distinct characteristics, namely geometrical form and the relative proportions of length L , width W and thickness T (Hawkins, 1993). In British standard 2955 an attempt has been made to define shapes qualitatively using the terms such as acicular (needles shaped), angular (sharp edged), spherical (globule shaped), which certainly have general descriptive value; but for scientific shape assessment, mathematical definitions are also needed. The most common shape factor that is being used is the one based on the concept illustrated by Heywood (Dodd's et al., 1995; Kaye, 1999; Brittain, 2000). Heywood conceived spheres of equal volume and of equivalent surface to the irregularly shaped grain. Starting with the projected image of the particle resting in its stable position, the area of the image is assessed and the diameter x_H of the equivalent circle is calculated. The volume V of the particle is then defined by:

$$V = k_H x^3 \quad (2.3)$$

where k_H is the volume constant for that particle.

Similarly the surface area 'A' of the particle is defined by:

$$A = f_H x^2$$

(2.4)

where f_H is the surface constant. The ratio f_H/k_H is used as a shape factor, combining the volume and surface constants.

Apart from Heywood diameter many have used statistical diameters such as x_M proposed by Martin (Dodds et al., 1995) or x_F proposed by Feret or a sieve size as discussed by Harris (Perry and Green, 1997). Buchen et al., (1993) have discussed the definitions of various statistical diameters and the range of shape indices (ratio of characteristic diameters). Kaya and Hogg (1997) have pointed out the relative effects of material and machine on the shape of the product particles. They stated clearly the machines and materials which were used, and product shape comparison was made in terms of the flakiness index and concluded that the smaller the ratio, the more cubiform the particle.

Energy utilization is independent of the applied energy over a wider range during the breakage of fully confined bed of particles, whereas for the partially confined case, both the specific surface and the energy utilization fall off from the respective levels of the fully confined case, as applied energy is increased (Kirchner et al., 1994). Increase in surface is directly proportional to the applied specific energy over a wide range in the case of single particle tests (Schubert, 1993). For single –particle impact breakage the utilization of applied energy is a function of initial particle size (Schubert, 1997). Reduction of utilization of energy from the maximum with increase of specific energy beyond the optimum is due to particle-to-particle friction as breakage proceeds during the impacting process (Schoenert, 1994).

Stored energy decreases proportionally with particle volume. However the energy needed for crack propagation diminishes proportionally with the cross section. As particle size is reduced, it can happen that less energy is stored than is required and the crack will stop. Then more energy must be fed in before final breakage occurs. Plastic deformation effects become increasingly important as particle size is reduced (Schoenert, 1995; 1997). As particle size is reduced higher impact velocity is required to cause breakage (Hrsg, 1991; Firus and Belter, 1999).

For a given material ground in a given mill, there appears to exist an equilibrium state of grinding, as conceived by Zwingelberg (1995), in which small particles are forming larger particles as fast as larger particles are being disintegrated. It is essential to differentiate between materials which behave predominantly elastically or plastically before any deformation behaviour or breakage phenomena encompassing particle stress patterns, under the action of applied forces is to be studied (Gross, 1999).

When very fine grinding is undertaken, effects occur which are not present in coarse grinding. These include aggregation and agglomeration, the influence of gas surrounding the particle and plastic deformation. The forces and processes which lead to aggregation and agglomeration have been considered extensively by Rumpf (1990). They include solid and liquid bridge formation between small particles, van-der Waals forces and electrostatic forces.

The properties at low temperatures are significantly different from those at ambient temperature and there is no substitute for test data especially for biological materials such as turmeric, examining the common indices of strength of materials such as elastic constants, ultimate stress, hardness and toughness needed for any fracture analysis. Thus the fracture of many solid food materials is a combination of complex events, which occur at the micro structural level of the solid. It is important to know which of the micro structural features determine the operation of fracture mechanism.

The principal conclusions drawn by Prof. Rumpf (1990) on the fracture of materials, which impinge directly on practical comminution, were:

(a) More energy is needed to break small particles than large. It is the breaking strength of the particle up to the moment of fracture, rather than the magnitude of the externally applied impact energy, which really decides the resulting size distribution. The externally applied energy is obviously necessary, but all of it is not used for fracture.

(b) When a brittle material is stressed by an applied force, underneath the area of force of contact there develops a cone –shaped zone of stress concentration in which particle degradation is intense compared with the space outside the

zone. Hence fines are derived chiefly from these cone- shaped zones and a much coarser grade from the rest of the particle. Repeated fracture produces more fines than single fracture for the same expenditure of applied energy.

(c) The rate of application of breakage forces is more important for visco-elastic materials than for brittle materials. Increasing the speed of a single impact has the same effect on the pattern of size distribution change as increasing the time of grind.

(d) The size distribution from primary breakage is complex and is usually bimodal. If sufficiently high levels of elastic strain energy per unit volume of materials (energy density) can be developed within the material by the application of an external force, the material disintegrates into particles of range of sizes, including submicron particles. This happens for both slowly and rapidly applied forces and for tensile and compressive forces.

(e) The density distribution is multimodal In primary breakage,. A monomodal pattern gradually emerges with grinding beyond primary breakage. For a given material, whatever the feed size, after continuous grinding the distributions tend to coincide.

(f) This fracture behaviour is consistent with current knowledge of fracture mechanics and with observed rates of crack propagation, as well as with correlations of fracture surface area with energy dissipated in the material. Fracture behaviour depends on mechanical properties and not on chemical properties and there is no significant difference between the axial and diametral impact of materials.

2.3.2 Thermal effects

During the comminution of solid food materials, intensive energy degradation into heat takes place due particle motion and frictional contact. Thermal effect prediction during fracture of food materials is important, in many industrial processes like modifying and controlling the size and shape distribution

of a population of particles, minimizing energy in order to have an acceptable quality and yield as well as preventing degradation of particles that can cause serious problems elsewhere in the system. The overall energy balance is

$$\text{kinetic energy} \rightarrow \text{elastic energy} \rightarrow \text{heat} \quad (2.5)$$

This description is consistent with the fact that the amount of fracture surface formed correlates with impact energy and not with collision velocity. The simplest relation between elastic energy and stress is given by the expression for uniform stress, σ , in a body of volume V_n as a result of energy input, W_o as

$$W_o / V_n = \sigma^2 / 2 E \quad (2.6)$$

where E is the Young's modulus of elasticity. According to the principle of dimensional analysis (Szirets and Rozsa, 1997), the dimensions W_o / V_n , E , and σ are the same: energy per unit volume, termed as energy density. Energy density as well as stress can be considered as the driving force for fracture. Also the correlation of energy and fracture surface area is given by (Timoshenko and Goodier, 1987)

$$\varepsilon W_o = \gamma_f S_n \quad (2.7)$$

where W_o is the energy input, ε is the fraction of input kinetic energy actually dissipated, S_n , the measured total fracture surface area and γ_f the material fracture strength. In general the eq. (2.6) defines a mean stress for the mean energy in any part of part of the compressed body.

The overall energy conversions shown in eq. (2.5) may be measured and calculated in the usual ways. But the results of fracture cannot be calculated from continuum mechanics since fracture is a rate process with random stress fluctuations. So the characterization has to be done empirically and statistically. The log-normal analysis has been developed and applied for characterizing small particles. The mathematics of the log-normal probability distribution (Herdan, 1960, Wanibe and Itoh, 1999, Limpert et al., 2000) can be summarized as follows:

1. The normal probability density function, $p(u)$, is defined in terms of the standard normal variate, u , normally distributed with mean zero and standard deviation one as

$$p(u) = (1/2\pi)^{1/2} e^{-u^2/2} \quad (2.8)$$

2. It can be seen that

$$-d \ln p(u) / du = u \quad (2.9)$$

eq. (2.9) shows that $p(u)$ varies fractionally in inverse proportion to the absolute value of u ; $p(u)$ has a maximum value and is symmetrical about $u=0$.

3. Variate, X , is said to be distributed normally, with mean m and standard deviation σ_n , when

$$u = u(X) = (X - \mu) / \sigma_n \quad (2.10)$$

where $u(X)$ measures the difference of the variate from the mean in units of the standard deviation.

4. Variate, D , is said to be distributed log-normally with geometric mean, D_g , and geometric standard deviation, σ_g when

$$u = u(D) = (\ln D / \ln \sigma_g) - (\ln D_g / \ln \sigma_g) \quad (2.11)$$

an equivalent of (2.11) is

$$D/D_g = \sigma_g^u \quad (2.12)$$

which also shows the relation between u and D .

It can be seen that $u(D)$ measures the ratio of the variate to the mean in terms of a power of the standard deviation σ_g . This is the basic log-normal distribution, as distinguished from the normal.

5. The cumulative normal or log-normal distribution is $P(u)$, where

$$P(u) = \int_{-\infty}^u p(u) du \quad (2.13)$$

as required by probability function

$$P(\infty) = \int_{-\infty}^{\infty} p(u) du = 1 \quad (2.14)$$

6. In small-particle statistics, the log-normal distribution of D is defined by measured cumulative volume (or mass) fraction $V(D) / V_n$.

$$P(D) = V(D) / V_n = P(u_v); u_v = (\ln D / \ln D_g) - (\ln D_g / \ln \sigma_g) \quad (2.15)$$

7. The distribution of D in terms of cumulative surface-area fraction $S(D) / S_n$ is

$$S(D) / S_n = P(u_s); u_s = u_v + 3 \ln \sigma_g \quad (2.16)$$

8. The distribution of D in terms of cumulative particle-number fraction $N(D)/N_n$

$$N(D) / N_n = P(u_n); u_n = u_v + 3 \ln \sigma_g \quad (2.17)$$

9. The differentials dS and dV of the distribution are

$$dS = dS(D) = S_n dP(u_s) = S_n p(u_s) \quad (2.18)$$

$$dV = dV(D) = S_n dP(u_v) = V_n p(u_v) \quad (2.19)$$

Therefore, at a given D, the “point” value of the surface/volume ratio is

$$dS/dV = S_n p(u_s) / V_n p(u_v) \quad (2.20)$$

10. For a given log-normal particulate, the overall surface/volume ratio S_n / V_n is related to the parameters, D_g and σ_g , and to a surface/volume shape factor,

$$\alpha = a_s / a_v ; \quad S_n / V_n = \alpha (\sigma_g^{0.5 \ln \sigma_g}) / D_g \quad (2.21)$$

2.4 Measuring fracture resistance

The separation of a stressed solid into two or more pieces is the end result of a complex series of interacting events. The process of fracture in most materials can be summarized as :

1. Damage accumulation
2. Nucleation of one or more cracks
3. Propagation of a crack to the complete separation of the material.

Damage accumulation and crack nucleation are associated with material properties, such as atomic and crystal structure, and the boundaries between grains and phases. Though the discipline of fracture mechanics has been and being addressing the problems associated with crack propagation, it does not involve crack nucleation, but seeks to answer the question: Given a certain stressed solid containing a crack whether induced or pre-existing, when and what rate does failure occur. Two related phenomena need to be studied to determine the fracture behaviour of a fibrous material like turmeric. The first is to investigate

the influence of the fibers on the crack tip stress field and the second is the mechanism of crack growth past the fibers (Aicher,1993).

“Toughness” is a general term used to describe a material’s resistance to fracture and “Hardness” is the term used to describe resistance to deformation. In short, toughness may be sufficient to describe the resistance to fracture initiation from an induced or pre-existing flaw in the material. Fracture criteria based on this concept assume that failure occurs when the “applied” parameter exceeds a critical value characteristic of the material. Criteria of this type include the Plane strain fracture toughness (K_{Ic}), the critical strain energy release rate (G_c), and the critical maximum principal stress (σ_{1c}). Toughness may also be used to describe the resistance to stable crack propagation after the fracture initiates. Methods of measuring this type of toughness include Crack growth resistance curves (G_R -curves) and the Fracture surface energy or Work of fracture (Γ_{wof}).

2.4.1 The Fracture surface energy - Fundamental concept

Griffith (1921) published a theoretical criterion for rupture, based upon the assumption that the equilibrium state of a stressed elastic body is such that the potential energy of the system is minimized. He postulated that:

Just as in a liquid, so in a solid the bounding surfaces possess a surface tension which implies the existence of a corresponding amount of potential energy. If owing to the action of a stress a crack is formed, or a pre-existing crack is caused to extend, therefore, a quantity of energy proportional to the area of the new surface must be added, and the condition that this shall be possible is that such addition of energy shall take place without an increase in the total potential energy of the system.

This means that crack propagation will occur if the energy released upon crack growth can provide all the energy required for crack growth.

2.4.1.1 Measuring fracture surface energy

In a brittle material like, turmeric, the energy for crack growth consists entirely of the surface energy to form the new surfaces. This energy can be estimated from the slow, stable propagation of a crack completely through a prenotched specimen (Hutchinson and Evans, 2000). The total energy consumed by the fracture process (the work -of - fracture) is determined from the area under the load displacement curve. The specific fracture surface energy is then the work-of-fracture, divided by the planar projection of the crack surface area $2A$, or

$$\Gamma_{\text{wof}} = \text{Work of fracture} / 2. A \quad (2.22)$$

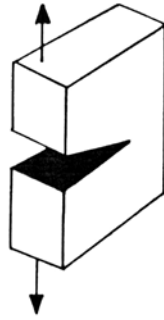
Γ_{wof} is a material property if the only energy –absorbing process in fracture is the production of new surface.

2.4.2 The Plane strain fracture toughness

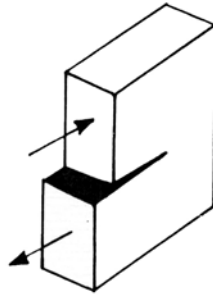
The plane strain fracture toughness measures the resistance of the propagation of an existing crack. The basic assumption is that crack extension occurs in a self similar manner, when the crack tip stress intensity factor reaches a critical value, which is a material property.

2.4.2.1 Crack tip stresses

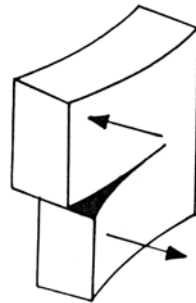
The three principle modes of crack opening in a solid are shown in Fig. 2.2. In Mode I, the opening mode, the applied stress are normal to the leading edge of the crack. Mode II, the sliding mode, is caused by shear stresses acting normal to the crack plane. Mode III, the tearing mode, has shear stresses parallel to the leading edge of the crack (Anderson, 1995). A superposition of these three principle modes can completely describe the opening of any crack.



(a) Mode I



(b) Mode II



(c) Mode III

Fig. 2.2: Crack opening modes (a) Mode I, the opening mode (b) Mode II, the sliding mode (c) Mode III, the tearing mode

Consider an infinite, homogeneous and elastic plate containing a crack of length $2a$ and subjected to a stress field far from the crack, as shown in Fig. 2.3. The crack tip stress fields for each fracture mode can be calculated from linear elasticity theory, by differentiating an appropriate Airy stress function, such as the Westergaard complex stress function (Xia et al., 1994).

The stresses acting on the material element $dx \cdot dy$, located at a distance r and angle θ from the crack tip for each of the three crack opening mode are given by (Tada et al., 2000):

Mode I :

$$\begin{bmatrix} \sigma_{xx} \\ \sigma_{yy} \\ \sigma_{xy} \end{bmatrix} = K_t / \sqrt{2\pi r} \cos \theta/2 \begin{bmatrix} 1 - \sin \theta/2 & \sin 3\theta/2 \\ 1 + \sin \theta/2 & \sin 3\theta/2 \\ \sin \theta/2 & \sin 3\theta/2 \end{bmatrix}$$

$$\begin{array}{ll}
 \sigma_{xz} = \sigma_{yz} = 0 & \\
 \sigma_{zz} = 0 & \text{plane stress} \\
 \sigma_{zz} = \nu (\sigma_{xx} + \sigma_{yy}) & \text{plane strain}
 \end{array}$$
(2.23)

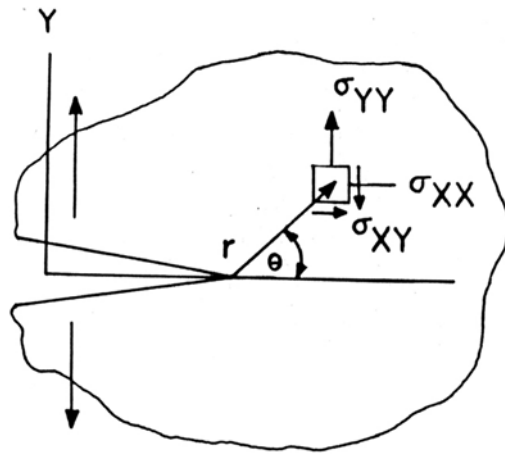


Fig. 2.3: Definition of crack tip stresses

Mode II :

$$\begin{bmatrix} \sigma_{xx} \\ \sigma_{yy} \\ \sigma_{xy} \end{bmatrix} = K_{t1} / \sqrt{2\pi r} \begin{bmatrix} -\sin \theta/2 & 2\cos \theta/2 & \cos 3\theta/2 \\ \sin \theta/2 & \cos \theta/2 & \cos 3\theta/2 \\ \cos \theta/2 & [1-\sin \theta/2 & \sin 3\theta/2] \end{bmatrix}$$

$$\begin{aligned}
 \sigma_{xz} = \sigma_{yz} &= 0 \\
 \sigma_{zz} &= 0 \quad \text{plane stress} \\
 \sigma_{zz} &= \nu (\sigma_{xx} + \sigma_{yy}) \quad \text{plane strain}
 \end{aligned}$$

(2.24)

Mode III :

$$\begin{bmatrix} \sigma_{xz} \\ \sigma_{yz} \end{bmatrix} = K_{t2} / \sqrt{2\pi r} \begin{bmatrix} -\sin \theta/2 \\ \cos \theta/2 \end{bmatrix}$$

$$\sigma_{xx} = \sigma_{yy} = \sigma_{zz} = \sigma_{xy} = 0$$

(2.25)

The parameters K_t , K_{t1} , K_{t2} in these equations are known as the stress intensity factors for Mode I, Mode II, and Mode III loading respectively. Because the stresses become infinite as $r \rightarrow 0$, the K 's measure the stress singularity at the crack tip. It can be shown by elastic theory (Timoshenko and Goodier, 1987) that

$$K_t = \sigma_{\max} / \sigma_{\text{nom}} \quad (2.26)$$

where σ_{\max} applied maximum stress and σ_{nom} is the nominal stress.

2.4.2.2 Measuring fracture toughness

In isotropic materials under essentially elastic conditions, cracks tend to grow in Mode I irrespective of their initial orientation (Smith and Chui, 1994). Also, under plane strain conditions the fracture toughness is essentially constant and independent of sample thickness. This makes the opening mode plane strain fracture toughness K_{Ic} , one of the most important measures of fracture resistance. The steps involved in the determination of plane strain fracture toughness are in principle, quite simple. First, a precrack is initiated in a calibrated specimen. As the crack grows under applied load, the crack front extension is measured. K_{Ic} is calculated from an equation of the form of (2.26), using the specimen dimensions and load required to extend the crack (ASTM standard, 1995).

2.4.3 The Strain energy release rate

The mathematical form of Griffith's fracture criterion is called the "Energy release rate". Considering the crack plate, with unit thickness, as shown in Fig. 2.3, if U is the total elastic energy and W is the energy required for crack surface formation, then an additional crack of size ∂a can be formed when

$$\partial U / \partial a = \partial W / \partial a \quad (2.27)$$

The quantity $\partial U / \partial a$ is called the elastic energy release rate, and is usually designated by the symbol G . From a physical point of view, G represents the difference in potential energy (per unit thickness) of identical bodies containing cracks of length 'a' and of length 'a+ ∂a '.

2.4.3.1 Criterion for crack growth

Crack extension can occur when the applied G reaches a critical value, G_c . For a completely brittle material, the energy required for crack growth, W , is the surface energy to form new free surfaces:

$$W = 2\Gamma \Delta a \quad (2.28)$$

where Γ is the surface energy and Δa is the length of the crack formed. The factor of 2 is included because during crack extension, two fracture faces are formed. Employing this definition and eq. (2.27) one obtains the critical energy release rate, G_c :

$$G_c = \partial (2\Gamma \Delta a) / \partial a = 2\Gamma \quad (2.29)$$

Fracture is predicted when the applied G equals G_c .

The energy criterion is equivalent to the stress intensity criterion discussed above. Using the stress field calculations for an elliptical flaw, Griffith calculated the strain energy release rate per unit thickness in terms of the applied stress, σ , the material's elastic modulus, E , and the crack length, a , to be (Griffith, 1924):

$$G = \partial U / \partial a = \pi \sigma^2 a / E \quad (2.30)$$

$$G = \pi \sigma^2 a / E \quad \text{for plane stress and}$$

$$G = (1-\nu) \pi \sigma^2 a / E \quad \text{for plane strain} \quad (2.31)$$

2.4.3.2 The Crack-resistance curve

The crack-resistance, or G_R - curve, characterizes the resistance of a material to slow, stable fracture. The G_R - curve is another version of the Griffith energy balance, and is essentially a plot of the strain energy release rate versus crack extension. Crack resistance curves for a material can be determined experimentally by two methods. The first method consists of measuring the critical G of multiple specimens with different crack lengths (ASTM standard, 1995). The primary disadvantages of this technique are the large number of specimens required, and the inability to correct the determined G value for crack extension (Anderson, 1995). G_R - curves can also be determined from a single load displacement record (Bush, 1999). The total potential energy stored in a solid, U , is equal to area under the load displacement diagram,

$$U = P \cdot \delta / 2 \quad (2.32)$$

then,

$$G = P/2 \cdot (\partial \delta / \partial a) \quad (2.33)$$

As long as the deformations are elastic and there is no crack growth, the displacement δ is proportional to the load P : $\delta = C \cdot P$, where C is the specimen compliance. For this case, G becomes

$$G = P^2/2 (\partial C / \partial a) = P \delta / 2C (\partial C / \partial a) \quad (2.34)$$

$$\eta_{EL} = b/C (\partial C / \partial a) \quad (2.35)$$

where b is the remaining material in front of crack. With this definition, G can be written as

$$G = 1/b \eta_{EL} \delta P / 2 \quad (2.36)$$

Eq. (2.36) is completely general, and can be used for complex structures which cannot be treated analytically.

2.4.4 The Maximum principal stress

The maximum principal stress criterion predicts the direction of crack growth as well as when it will occur. The criterion assumes that a crack will proceed in a direction perpendicular to the maximum principal stress, when that stress reaches a critical value at some distance from the crack tip, that is fracture occurs when applied stress \geq critical maximum principal stress. The critical stress value is the same value as that at fracture in a mode I case:

$$\sigma_{1c} = K_{Ic} / \sqrt{2\pi r_0} \quad (2.37)$$

The maximum principal stress criteria and the energy release rate are equivalent (Cocks et al., 1999).

2.4.5 Thermal effects characterization

The input energy density shown in eq. (2.6) can also be applicable to thermal effects; that is

$$W_o / V_n = C_v \Delta T \quad (2.38)$$

where W_o / V_n is the energy density, C_v is the heat capacity of the material and ΔT is the temperature rise.

For a typical material and fracture tests, the overall average temperature rise is small, the order of 1°C. However, local energy densities can be larger than the average, with much higher temperatures. Based on the energy/surface area correlation of eq. (2.7), it can be supposed that portions of the material producing very small particles (with very high surface/volume ratios) are also portions that have very high energy densities discharged into heat, with resultant local high temperatures.

Representing local energy densities and local surface/volume ratios as the differential form dW/dV and dS/dV respectively, from eq. (2.7),

$$dW/dV = (\gamma_f / \varepsilon) dS/dV \quad (2.39)$$

where (γ_f / ε) is the combined strength parameter that can be determined from eq. (2.7). The local surface /volume ratio, dS/dV , is given mathematically, as in eqs (2.18) – (2.20).

The calculation of the local temperature rise ΔT in terms of the log-normal parameters and material properties is,

$$\Delta T = 1/ C_v (dW/dV) \quad (2.40)$$

where (dW/dV) is given by eq. (2.39) and

$$dS/dV = S_n p(u_v + l_n \sigma_g) / V_n p(u_v) \quad (2.41)$$

where $p(u_v)$ is the normal probability density function, evaluated for u_v , a function of particle diameter, D , described in items 5 and 6 of the section 2.3.2 and S_n / V_n given by eq. (2.21). For a given D , log-normal parameters allow ΔT to be calculated for a particular fracture particulate.

The finite element method is a computer- aided mathematical technique for obtaining approximate solutions to the equations of calculus that predicts the response of a physical system to external influences. The salient features of any finite element analysis are (Zienkiewicz and Taylor, 2000):

- Divide the domain into a mesh of discrete elements. Governing equations are associated with each element, which determine the response of the element to node point quantities.
- Assemble the element governing equations to form the system equations. These characterize the response of the entire system.
- Impose the boundary conditions, which define the external loads, by modifying the system equations.
- Solve the system equations using conventional numerical analysis techniques. These are chosen to take advantage of the form of the equations.
- Derive meaningful quantities from the solution. These can be displayed in tabular, graphical or pictorial forms. In a solid mechanics analysis, these quantities include the displacement and stress fields in the solid.

The general purpose program used in this study is based on the displacement method. First order element shape functions are used; the displacements vary linearly between node points. Appendix A contains a complete description of the assembly of the governing equations and their solution. The finite element method for predicting fracture mechanics parameters is well established (San et al., 1997). The application of the method to crack propagation problem involves three interrelated, but distinct considerations: crack tip singularity modeling, fracture prediction and crack extension simulation.

2.5.1 Crack tip singularity modeling

There is a fundamental incompatibility between the theoretically infinite stresses at a crack tip and the finite element method. Adequate representation of the crack tip singularity can be achieved either by using a very fine element mesh in the crack tip region, or by the incorporation of the $1/\sqrt{r}$ stress singularity in the shape function of the crack tip element (De Borst et al., 1993). The advantage of the latter approach is that coarser, and hence fewer, elements are required to attain an equal level of accuracy. The disadvantage of special elements is that when the location of the crack tip changes, the shape function of the element at the new crack tip must be modified to include the stress singularity. The system equations then must be completely reassembled.

The use of a fine element mesh in the crack tip region overcomes this limitation. When the location of the crack tip changes, the system equations are altered slightly by modifying the appropriate terms. The drawback is that a relatively large number of elements must be used, which increases computation time and requires sufficient computer storage. The simplicity of modifying the system equations for crack growth overwhelms these impediments. This approach is used in the parametric finite element studies performed as part of this study.

2.5.2 Fracture prediction

The techniques developed to measure the fracture resistance of a material can also be applied to predict crack growth in a finite element model. The finite element method provides approximations of the displacement and stress fields in the solid. Two approaches have been followed to obtain the crack tip stress intensity: the direct method and the indirect method.

In the direct method, the stress intensity is calculated by substituting stress or displacement values, at points in front of the crack, into the general analytical solutions of the crack problem. The stress intensity at the crack tip is

then estimated by extrapolation. This method relies on the assumption that the body is linearly elastic, homogenous and isotropic. If the solid contains material discontinuities (e.g. inclusions, fibers or holes), then the direct method cannot be used to evaluate the crack tip stress intensity.

The maximum principal stress criterion can also be applied directly to predict fracture in the finite element model. This method involves calculating the magnitude and direction of the maximum principal stress in front of the crack tip. When maximum principal stress, σ_1 reaches a critical value, crack growth proceeds in a direction perpendicular to σ_1 . This method is easily implemented, because most finite element codes can calculate the principal stresses as part of their solution. The limiting factor here is determining the appropriate critical value of σ_1 .

In an indirect method, the stress intensity is determined from its relation with other quantities such as the compliance or elastic energy. Indirect methods can be used for a body of arbitrary geometry for which the analytical solution is unknown, or for one which contains material discontinuities. A widely used indirect method of evaluating the strain energy release rate is called the “virtual crack extension technique”. Consider a crack of length a which advances by an incremental amount ∂a , as shown in Fig. 2.4. The strain energy in each of the two configurations can be evaluated as

$$U = [d]^T \cdot K \cdot d \quad (2.42)$$

where d and K are the global displacement vector and stiffness matrix, respectively, of the finite element model. The strain energy release rate was defined as (Section 2.4.3):

$$G = \partial U / \partial a \quad (2.43)$$

The evaluation of eq. (2.43) involves performing two finite element analyses for two crack lengths which differ by an incremental amount. Numerical differentiation yields the strain energy release rate (Erbe et al., 1994). Crack growth will take place in the direction of the maximum energy release rate, when G a critical value.

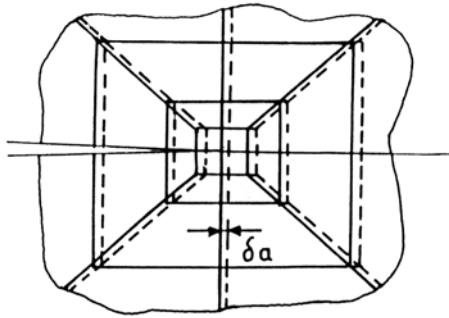


Fig. 2.4: The virtual crack tip extension

The indirect methods have the advantages that no extrapolations are required and there is no need for a particularly fine crack tip mesh (Erbe et al., 1994). The disadvantage is that in mixed mode fracture, it is generally not possible to separate G into its modal components G_I , G_{II} and G_{III} .

2.5.3 Crack extension simulation

Once crack growth is predicted, the mesh geometry must be changed to represent the new crack tip location. One method is to redefine node locations and element connections in the crack tip region. This can be extremely time consuming and computationally expensive, because the system equations must be completely reassembled for the new geometry.

Another technique is known as “slicing nodes”. Here, the node at the crack tip is replicated and the associated element connections are redefined. The disadvantage is that the nodes must be renumbered to keep the stiffness matrix well banded, and the system equations, starting from those for the split node, must be reassembled.

A more efficient alternative is Tvergaard’s element vanish technique (Tvergaard and Hutchinson, 1992), which is used in this study. Here crack growth is simulated by releasing connections between nodes through either a zero input for the element stiffness or by deleting the element from the mesh. This method has two advantages. First, the node point locations and numbering need not be changed. Only the terms in the governing equations which need to be changed are those associated with the deleted element. Second, the method can be easily applied to simulate microcracking ahead of the crack tip.

2.5.4 Temperature distribution

During the size reduction of food materials such as turmeric, there tends to be variation of the quality of the end product due to non-uniformity in temperature

distributions. The temperature distribution inside a turmeric is a very complex, physically unobservable phenomenon. So for a given condition (steady or unsteady), it is desirable to map the temperature distribution zones inside the turmeric. This mapping can be computed through finite element simulation technique.

One of the first applications of finite element method to non-structural problems was in the area of heat transfer by conduction and convection. (Zienkiewicz and Taylor, 2000). The solutions of heat transfer problem using finite element method can also be applicable for analysis of thermal problems. The solution of the heat transfer problem becomes input to the stress analysis problems and the same grid can be used to solve both problems.

The governing differential equation for steady-state heat transfer by conduction from a one-dimensional body, is given by (Zienkiewicz and Taylor, 2000).

$$k A d^2\phi / dx^2 = 0 \quad (2.44)$$

where k is the thermal conductivity, A is the cross sectional area and ϕ is the temperature. The temperature has a single value for all points on the cross section for a particular value of x and is normally known at one or both surfaces. The boundary conditions associated with (2.44) are usually a specified temperature at $x = 0$.

Now assuming a single element conductivity matrix, the element stiffness matrix ($k^{(e)}$) is given by

$$k^{(e)} = k A / L \begin{bmatrix} 1 & -1 \\ -1 & 1 \end{bmatrix} \begin{bmatrix} T_i \\ T_j \end{bmatrix} = 0 \quad (2.45)$$

where L , is the length of the specimen and T_i and T_j are the corresponding temperatures at two nodes. The element force vector matrix becomes zero when the conduction heat transfer is assumed or neglected when temperature is specified at both surfaces.

3. Objectives and scope of the work

The objectives of the present study were :

1. Investigations on the study of fracture mechanism, crack propagation, thermal effects of fracture particulates and particle shape formation arising from the comminution of turmeric (*Curcuma Longa*) as a model spice food material under ambient and low temperature conditions substantiated with theoretical approach.
2. Development of a Finite model for crack growth, to simulate and analyze the fracture mechanism including the generation of necessary experimental data needed for the prediction of fracture mechanism.
3. Studies on the effect of material properties and size reduction method along with the examination of fracture surfaces to ascertain whether propagating fractures interacted with the structural features of the food material to produce specific particle shapes and sizes.
4. Experimental studies to analyze, characterize and compare sizes and shapes along with the quality evaluation comprising microstructure, essential oil yield and gas chromatographic analysis of turmeric powder particle ground by conventional and cryogenic method.

Scope of the present work

1. The fracture behavior in a material is influenced by the material properties and its behavior under different temperature conditions. Knowledge of such properties and behavior of materials is very essential for proper design and fabrication of a size reduction system.

2. Particles of specific shapes and sizes can be produced by comminution, by studying the fracture progress in a given material. Information on size and shape effects during size reduction will prove useful to the industry, especially in the development of new products, product containers and attainment of satisfactory product quality. For a given product with known properties, the most desirable size and shape combination can be predicted for any given volume without changing the product formulation, to achieve a desired product quality.
3. Generally, the grinding machine manufacturers do not guarantee particle shape. With the help of the present study, it is possible to have a choice of suitable size reduction method as well as examine the causes of cracks and material properties to obtain a controlled particle size, shape and distribution.
4. Development of fracture models can serve as a methodology for measuring critical material properties and be used to improve or develop novel alternatives in size reduction.
5. The present study helps in exploring the inter-relationship between the fracture mechanism of the properties of the food material and material to matrix interface. It also enables prediction of fracture paths for individual fibers at discrete locations with respect to primary crack plane.
6. The study also provides practically useful quantitative information, wherein it is possible to predict the maximum temperature rise that could occur for a particle of a given diameter fractured under grinding and similar unit operations and as a principled basis for modeling effects in a field where deterministic thermodynamics and continuum mechanics is not possible to apply.

4. Materials and Methods

Materials

Turmeric

Fresh dried turmeric (*Curcuma Longa*) from local market was used. Sample of whole spice was taken before grinding for analysis. The turmeric samples are taken to be cylindrical in shape with a mean length of 52.5×10^{-3} m and mean diameter of 10.6×10^{-3} m (means of 12 turmeric stalks) for grinding experiments. For simulation and estimation of engineering properties three different sample sizes categorized as small (length, 28.23×10^{-3} m and diameter, 6.41×10^{-3} m), medium (length, 42.67×10^{-3} m and diameter, 8.92×10^{-3} m) and large (length, 52.5×10^{-3} m and diameter, 10.6×10^{-3} m) were used. A typical microstructure of turmeric is shown in Fig. 4.1. The average moisture content of the turmeric samples (mean of three replications) was found to be 12.5% and was determined by the oven method (Jia et al., 2000)

Liquid Nitrogen

Liquid Nitrogen procured from air separation plant (Mysore Oxygen Ltd, Mysore, India), was stored in 'Dewar' (capacity:33.5 L, brand name cryocan, make; IBP company Limited, Ahmedabad, India) and kept in cold room maintained at 4°C to prevent evaporative loss of liquid nitrogen. Liquid nitrogen in the cryo-grinding process serves two purposes- (i) to cool the raw material and the mill to operating temperatures and (ii) to remove the heat liberated during grinding. The liquid nitrogen supply to the cryo-grinder is done through the Dewar. The Dewar is kept reasonably close to the mill to reduce the losses from the pipe lines.

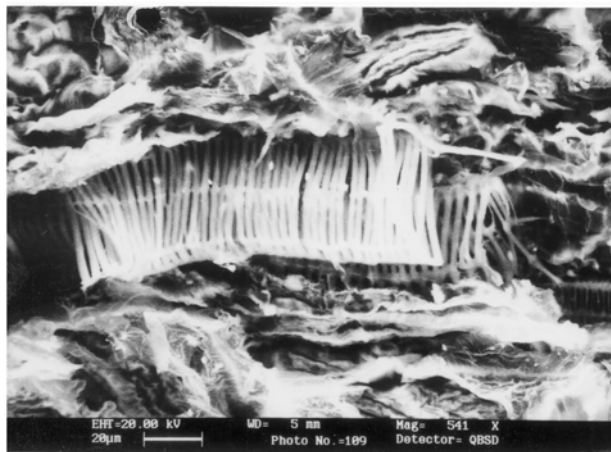
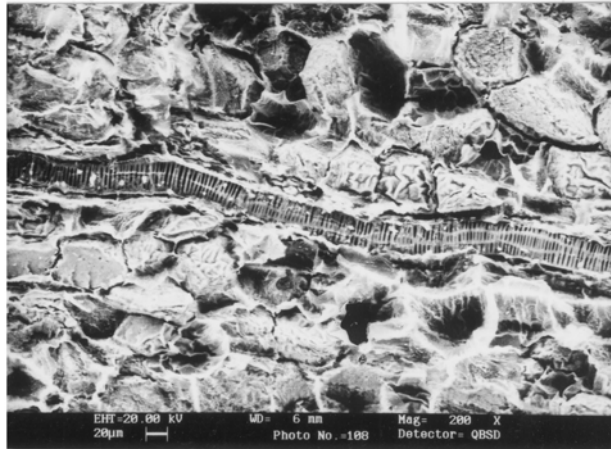


Fig. 4.1: The microstructure of turmeric

4.2 Methods

4.2.1 Size reduction mills

Conventional grinding

A hammer mill (M/s Apex Corporation, USA) was employed for this purpose without any cooling arrangement. The hammer mill has a cylindrical grinding chamber, which contains 6 hammers and powered by a 7.5h.p AC motor. The round screen nos. AP 0.027 (Tylor series no. 24), AP 0.0098 (Tylor series no. 60), AP 0.0035 (Tylor series no. 170), were used in hammer mill. On entering the mill the material is ground by repeated impact against the rotating hammers and the multiple strike back. The speed of the mill is 10000 r.p.m. The velocity of the tip of the hammer is 30 – 60 m/s. Grinding trials were done with and without using the screens. Mill was operated with the product from one milling becoming the feed material for the next milling up to a total of five passes.

Cryogenic grinding

An indigenously designed and developed pilot scale equipment at Central Food Technological Research Institute, Mysore, India was used. The schematic diagram and the picture depicting the grinding zone of the cryo-grinding system is shown in Fig.4.2 (a) and (b). From the filling hopper (1) the spice to be ground enters the vibratory feeder (2) which has provision for feed rate control. The material falls into screw conveyor (3) driven by motor, reduction gear and inverter control. Liquid Nitrogen from Dewar (4) is sprayed into the screw conveyor and the time of spraying on the material inside the conveyor is adjusted by the speed of the drive. Liquid Nitrogen injected (5) combines with the product thereby cooling and embrittling the product. The product is then transported, along with the cold gas generated by the evaporation of the liquid nitrogen to the grinding mill (6,7) where it is pulverized (Model: UPZ 160 from M/S Alpine AG, Germany). A sensor monitors the temperature of the grinding zone and the liquid nitrogen spray is optimized using automatic feed back control by a digital signal

processing (DSP) system and associated electronics. The ground product is collected in collecting bin (8). The pilot plant is totally designed and fabricated using stainless steel and other food quality materials. The feed material was subjected up to two passes. The mill was operated without using cryogen also.

The rate of liquid nitrogen consumption was determined by placing the Dewar (capacity: 35 litre) on a platform scale and noting the change in weight of the Dewar content.

Blender mill

It is a sharp bladed mill (Model: 2601 Cianflone Scientific Corporation, U.S.A) that achieves particle size reduction by impact action. It consists of a tubular vial which is fitted with removable end caps for easy cleaning. End caps are tightly sealed by means of 'O' rings. The mill is also provided with the timer and tachometer to vary the time and speed respectively. The mill was operated dry for 3,5,10 and 15 minutes.

Specific energy consumption

A three phase wattmeter (Make: Larsen & Toubro; Type – MP/MEI; range 0-3 kW, least count 5 W) was connected with the machine to measure the power consumed and ultimately measure the energy required in grinding. The specific energy consumed in grinding was calculated as:

Specific energy consumption = Power consumed (W) x 3.6 / Feed rate (kg/h)

Sampling

A 5 kg batch of turmeric was ground by using conventional mill and cryo-grinder. The ground powder was packed and sealed immediately after grinding in aluminium foil-polythylene laminate pouches and stored in the cold room at 4°C for subsequent analysis. Representative samples in triplicate from each grinding method were taken after grinding. An indigenously made sampling glass tube (1 m -long by 0.38 m -diameter) was used to collect the samples.

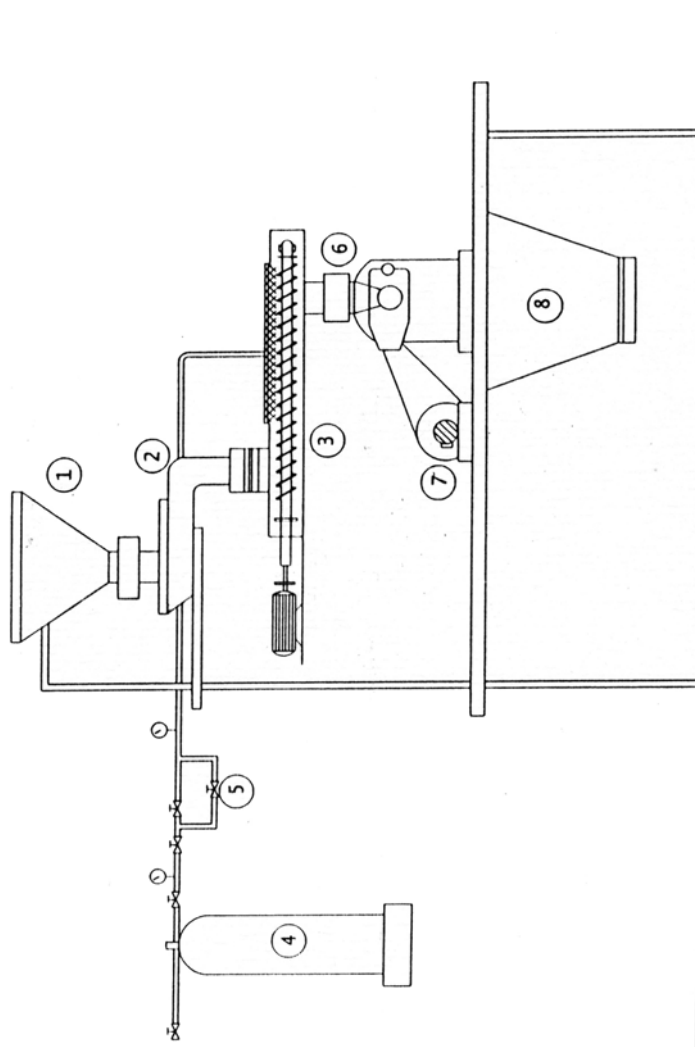


Fig. 4.2 (a): Schematic diagram of the cryo-grinding system

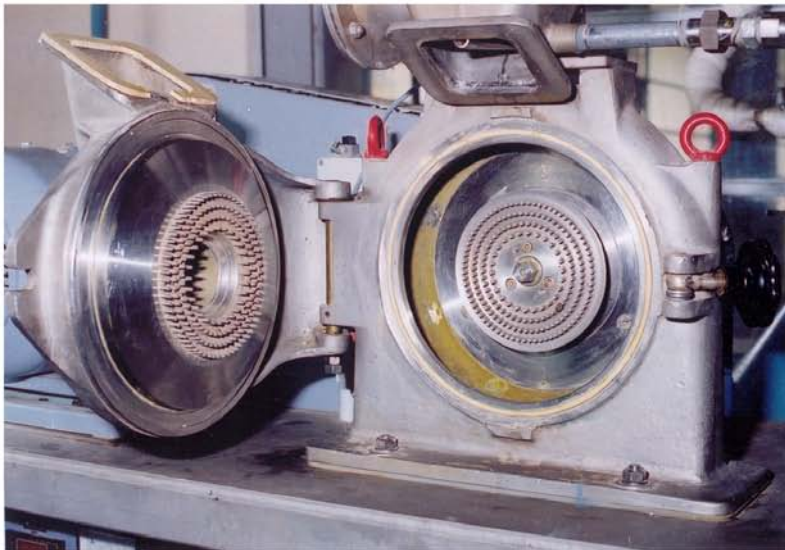


Fig. 4.2 (b): Picture showing the detail of the grinding zone employed in the cryo-grinding process

Statistical analysis

An analysis of variance was performed on particle shape data using the general linear models (GLM) procedure of SAS, Version 6.07 (SAS Institute Inc., Cary, NC). The analysis was carried out separately on each of the four size reduction methods (screened and unscreened hammer milling, blender mill and cryogenic mill), the purpose being to elucidate differences between particle shape for various sizes and treatments. Treatments for the blender were time of milling; and for the hammer mill and cryogenic mill, number of passes. The significance of any differences between means arising from the analysis of variance was tested by paired t-test comparisons.

Quality evaluation

Photomicrographs of the ground particles were obtained using scanning electron microscope (SEM: Model Leo 435VP,UK).

Essential oil and oleoresin estimation of conventional & cryo ground turmeric powder was done using Clavenger's apparatus and soxhlet apparatus respectively. Toluene distillation method was used to analyze the moisture contents of cryo ground and conventionally ground samples. Gas chromatographic analysis of essential oil obtained from cryo ground and conventionally ground turmeric powdered samples were carried out using Gas chromatograph (Model-Shimadzu-15A) fitted with stainless steel column (3m*3mm) packed with 10% SE-30 chromosorb W. The injection port and detector temperatures of the Gas chromatograph were maintained at 220° and 250°C respectively. The column temperature was programmed from 75°C (2 minutes) to 220°C (8 minutes) with an increment of 4°C / minute. The essential oil samples were diluted 5 times with acetone (10 µl oil in 40 µl acetone) and 1 µl was injected for the analysis.

4.2.2 Particle size and shape analysis

Computerized inspection system model CIS – 100 (M/s Galai Production Ltd., Israel) capable of measuring particles in the range 0.2 to 3600 microns was employed. The particle size analysis channel uses laser 2 mW HE-Ne with wave length 632.8 nm. The detector used was silicon PIN photo diode. Reliability of the instrument is up to two decimals.

For size analysis, the glass cuvette (3.5 ml) was filled with isopropanol and placed in the laser path. A representative sample of the ground material was put in the cuvette. A magnetic stirrer keeps the particles under suspension. The system software automatically generates the particle size distribution in graphical or tabular mode. Acquisition times for size analysis are less than 1 minute.

Different techniques generate a different mean diameter as well as measure different properties of the particles (Galai, 1994). Thus determination of mean diameters depends upon a particular application. As the present work involves grinding studies, measurement of the weight of particles in a particular range are significant. So volume mean diameter, as a single parameter in order to have an overall representation of the size of ground powders, had been used. Volume mean diameter = $\sum (x^4 dN) / (\sum x^3 dN)$ where x is the mean particle size corresponding to the range and dN denotes number of particles in that range. If all the particles are of same density, volume mean diameter is equal to the weight mean diameter.

Mathematical functions of size distribution

Particle size distribution data of turmeric powder obtained by both grinding methods are attempted to be represented by mathematical functions. These are described below.

Among the several commonly used functions to describe the size distribution data, the well known Rosin-Rommler-Bennett (RRB) equation (Prasher 1987) which is given below was employed.

$$F(x) = 1 - \exp(-x/x'_R)^n \quad (4.1)$$

where $F(x)$ is the cumulative undersize weight fraction, x'_R and n' are the parameters of the function. The above can be rearranged to give:

$$\log_e \log_e [1/(1-F(x))] = n' (\log_e x - \log_e x'_R) \quad (4.2)$$

When the left side of the above equation is plotted against $\log_e x$, a straight line is obtained with a slope n' termed as uniformity index of the distribution. Small values of n' indicate scattered well known distribution and large values imply uniform distribution.

Gaudin-Schumann function (Prasher 1987) given below is also used to describe the particle size distribution pattern:

$$F(x) = (x/x'_G)^n \quad (4.3)$$

where x'_G and n are the parameters of the function.

Another function which has been in wide use for the analysis of comminution is the log-normal distribution function (Prasher 1987) given as below:

$$dF(x) = \xi \exp(-b \log_e^2 (x/x_m)) dx \quad (4.4)$$

where b is the steepness constant $= 1 / (2 \ln^2 \sigma_g)$. σ_g is the ratio of the 84% size to the 50% size.

$$\xi = (b/\pi)^{1/2} \exp(-1/4b^*) / x_m \quad (4.5)$$

x_m represents the mode of the distribution which is equal to $c x_{50}$

$$c = \exp(-1/2b) \quad (4.6)$$

For Shape analysis, the cuvette with the particles suspended in the isopropanol was placed before the close coupled device (CCD) microscopic TV camera to produce images of the particles as they pass through the measurement zone. Shape parameters such as perimeter, shape factor, aspect ratio of 1000 focused particles were calculated from the system's software. Reliability of the instrument is up to two decimals (order of 0.01). Mean and standard deviation of the distribution of each parameter are also provided by the system's software. Acquisition times for shape analysis are less than 13 minutes.

Shape parameters are defined as below (Galai, 1994):

$$\text{Shape Factor (SF) or Sphericity } (\phi) = 4. \Pi A / P^2. \quad (4.7)$$

A and P are area and perimeter of the particles respectively. SF indicates the

sharpness of the object. A value of 1 for SF corresponds to a circle and 0.785 to a square whereas values approaching 0 indicate straight lines.

$$\text{Specific length} = (P + \sqrt{P^2 - 16. A}) / 4 \quad (4.8)$$

$$\text{Specific width} = (P - \sqrt{P^2 - 16. A}) / 4 \quad (4.9)$$

Specific length of the object is the estimated length of the object and specific width is the estimated width of the object. These parameters are significant mostly with reference to fibers or fiber-like objects. Spherical or near-spherical objects, have a specific length equal to the largest Feret's diameter (Galai, 1994). Since turmeric is fibrous in nature, the above shape parameters were determined in the present study.

Feret's diameter is the diameter of the projections of the object measured at specified angles. Here, average of four Feret's diameter is calculated for a particular particle and given as average Feret's diameter.

Martin's diameter is twice the distance from the centre of gravity to the edge of the object measured at 45 degrees interval starting from 0 degree to 315 degrees. The average of these values measured at these angles are calculated and given as average Martin's diameter.

Aspect ratio is the ratio between the minimum and maximum Feret's diameter.

4.2.3 Engineering properties

Material properties needed for fracture mechanism studies like the modulus of elasticity, Poisson's ratio, maximum breaking load, G_R -curve behaviour, fracture surface energy, fracture toughness of turmeric under ambient and low temperature conditions were determined, with the universal testing machine (UTM Model: H 50 KM Make: Hounsfield, UK, capacity: 50 kN). The test sample configurations are presented in Fig. 4.3. Density of turmeric samples was determined by using Pycnometer (Model 1000: Make: Quantachrome corporation, U.S.A.). Poission's ratio of the sample was determined as the ratio of lateral contraction (as a function of diameter) to the longitudinal strain.

To determine the above properties under low temperature conditions, same methods as described above was adopted except that the turmeric samples were dipped in cryo-can and taken out at every 15 minutes interval.

The temperature at the end of these intervals were recorded using platinum resistance temperature sensor (Model: 118 MF, Make: Rosemount Inc. U.S.A.).

All the experimental values reported are means of three replications; the probable error of the mean value was less than $\pm 5\%$.

Experimental and calculation procedures

Elastic modulus test procedures

The cylindrical turmeric stalks (length 52.5 mm; diameter 10.5 mm) were fabricated into modulus of rupture test samples measuring 3 mm x 6mm x 45 mm by carefully scraping and cutting on all sides. These samples were broken with the UTM in the four point bend test fixture shown in Fig. 4.4 at a cross head rate of 0.51 mm/min. Plots of the load versus cross head travel were recorded for all the tests.

Initially the tensile strain prevalent in the specimen was calculated by obtaining load-deformation values under ambient and cryogenic conditions which is given by

$$e = \delta L / L_1 \quad (4.10)$$

where 'e' is the tensile strain, $\delta L = (L_2 - L_1)$, L_2 , L_1 are the final and initial lengths of the specimen respectively.

The tensile stress induced over the specimen, ' σ ' is given by the equation:

$$\sigma = 32 M / \pi D^3 \quad (4.11)$$

where D , the diameter of the specimen, M , the moment at the center point over the specimen which can be calculated as:

$$M = F \times L / 4 \quad (4.12)$$

where F , load applied and L , the length of the specimen.

Since the lateral strain in the sample is negligible (Mohsenin, 1986), neglecting the strain along 'y' and 'z' directions, the tensile strain becomes equal to volumetric strain. Thus

$$\text{volumetric strain, } e_v = \delta L / L_1 \quad (4.13)$$

The slope obtained after plotting the calculated stress-strain from the different load-deformation tests yields 'Young's modulus' of elasticity which is given by,

$$E = \sigma / e \quad (4.14)$$

where E is the Young's modulus, σ , the tensile stress and e, the tensile strain.

In order to calculate the elastic stiffness or modulus of elasticity of each sample, the combined testing machine and sample fixture compliance was first estimated by loading the fixture, including the bearing supports to 30 kg. A linear regression analysis of the resulting load-deflection plot yielded the parameters necessary to correct the sample test records for system compliance. The elastic modulus of the sample was then determined from the initially linear part of the corrected sample load-deflection plots and the sample dimensions and the following equation:

$$E = S L^3 / 4 W B^3 \quad (4.15)$$

where S, is the initial loading slope, L, the outer span length, W, the sample width and B, the sample thickness

The parameters E, e_v and σ are used to obtain 'Poisson's ratio' which are related by,

$$\mu = 1 - [e_v - E / 3 \sigma / 2] \quad (4.16)$$

where μ , is the Poisson's ratio, E is the Young's modulus, σ , the tensile stress and e_v , the volumetric strain.

(Eqs (4.10) to (4.16), from Mohsenin, 1986)

The product of stress and strain is energy per unit of cross sectional area known as 'strain energy' and is given by

$$\begin{aligned} U &= f^2 / 2 E \times \text{volume of the specimen} \\ &= (f^2 / 2 E) \times A.L \end{aligned} \quad (4.17)$$

where U , is the strain energy, f , the maximum stress intensity, L and A , the length and area of cross section of the specimen respectively.

As the specimen is subjected to external forces, its deformation behaviour is characterized by the deflection. Since the loading pattern of the specimen is similar to a simply supported beam type, the magnitude of deflection is determined as

$$C = Fl^3 / 48 EI \quad (4.18)$$

where C , the deflection, F , the load applied, E , the Young's modulus, I , the moment of inertia which is given as

$$I = \pi d^4 / 64 \quad (4.19)$$

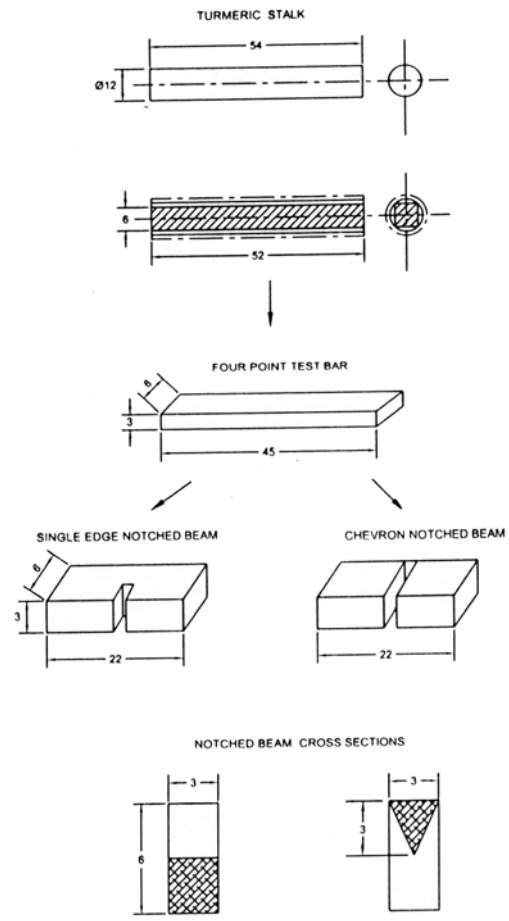
where d , the diameter of the sample

Maximum stress intensity – This is the stress induced over the specimen, given as force applied per unit area (Nash, 1998).

(Eqs (4.17) to (4.19), are from Nash, 1998)

Stress intensity distribution

Stress intensity distribution under different loads and temperature conditions, were done by using Finite element analysis software ANSYS (version 5.4). Variations of stress intensities under ambient and low temperature conditions were determined by i) varying the height to base ratio (0.25 – 1.00) keeping the volume constant and ii) under three different volumes (9.1×10^{-7} , 26.56×10^{-7} , $46.33 \times 10^{-7} \text{ m}^3$ - approximately closer to commonly available turmeric samples). The most commonly used cylindrical shape of turmeric was considered in the estimation of stress intensity. The following processing conditions were adopted for the analysis: Type of modeling – solid; Mesh – Tetrahedron solid; Degrees of freedom – all dimensions locked. Hyper- matrix calculation was used as solver to obtain deflection (mm) and stress intensity (Pa) values (Desalvo and Gorman, 1989).



All dimensions are in mm

Fig. 4.3: Test sample configurations

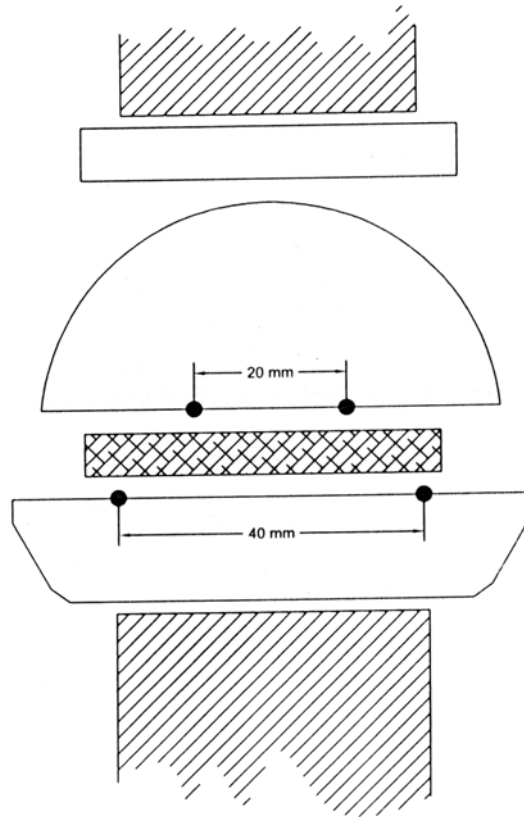


Fig. 4.4: The four-point bend test fixture

Stress intensity factor

The term stress intensity factor is defined as the ratio of actual maximum stress (σ_{\max}) to a corresponding nominal stress (σ_{nom}) which is given by

$$K_t = \sigma_{\max} / \sigma_{\text{nom}} \quad (4.20)$$

(Antunes et al., 1999)

The nominal stress is referred to an arbitrarily chosen area. The value of the nominal stress is calculated on the assumption of a hypothetical elementary stress distribution with respect to a particular reference area. Soon after the yielding at the point of maximum stress, the localized high-stresses are spread and their intensity is varied (Antunes et al., 1999). As the stress intensity factor depends on the type and relative size of discontinuity and also since the nominal stress is calculated referring to a hypothetical element having no geometrical deviation, in order to make a fair evaluation of the absolute effect of the stress intensity factor in the analysis, published stress intensity factor values, closer to the range of conditions pertaining to the present study were used.

In order to determine K_t , maximum stress (σ_{\max}) induced as well as radius of curvature (r) values pertaining to different force-deflection were calculated initially.

σ_{\max} was calculated using eq. (4.11) and radius of curvature 'r' was calculated as

$$r = L_1 / 2 \tan^{-1}(x / L_1 / 2) \quad (4.21)$$

(Antunes et al., 1999)

where x , the deflection corresponding to the applied force, L_1 , the length of the specimen.

Utilizing this known r and after calculating (r/c) values where 'c' is the radius of the specimen, stress intensity factor, K_t corresponding to these (r/c) values from the published graph were obtained.

Hardness, toughness and brittleness

Hardness, H is the resistance to deformation expressed as

$$H = F / \alpha_0 R^2 \quad (4.22)$$

where F, is the force applied, α_0 , the indenter constant and R, radius of force contact area

Toughness, K_c is the resistance to fracture given as

$$K_c = F \xi(a) \quad (4.23)$$

where F, is the force applied, $\xi(a)$, function of $a = \sqrt{\text{crack length} / 2}$

Brittleness, B is defined as the ratio of H / K_c and is independent of applied load.

Hence:

$$B = 1 / \alpha_0 R^2 \xi(a) \quad (4.24)$$

(Eqs (4.22) to (4.24), from Zeng et al., 1996)

Fracture toughness test procedures

The plane strain fracture toughness test measures the resistance to fracture from an existing crack. Single edge -notched beam (SENB) samples were fabricated from the fragments of elastic modulus test bars which were long enough to be tested in three point loading with a 20 mm outer span. Notching was done with a 0.15 mm thick circular saw. Plane strain fracture toughness values were obtained by loading the specimens at a cross head rate of 0.025 mm/min, with the test fixture shown in Fig. 4.5. The notch depth was measured after the sample was fractured completely. The linear elastic fracture mechanics equation was then used to calculate the mode I fracture toughness of the sample:

$$K_{tc} = 3 Y PL \sqrt{a} / 2 W B^2 \quad (4.25)$$

where P, is the peak load, L, the outer span length (20 mm), a, the machined crack length of sample, W, the sample width, B, the sample thickness and Y, the geometrical correction factor

$$Y = 1.93 - 3.07 (a/W) + 13.66 (a/W)^2 - 23.98 (a/W)^3 + 25.22 (a/W)^4 \quad (4.26)$$

To predict the the comminution process of turmeric as to, whether deformation controlled or through crack propagation, the universal deformation –

fracture diagram proposed by (Prasher, 1987) was adopted utilizing the generated hardness and toughness values. The curve is essentially an equilibrium curve, where in the intersection of deformation and fracture indicates a threshold condition for which F^* is the maximum load that a solid might sustain in a contact even without the onset of fracture and a^* the critical crack length corresponding to F^* .

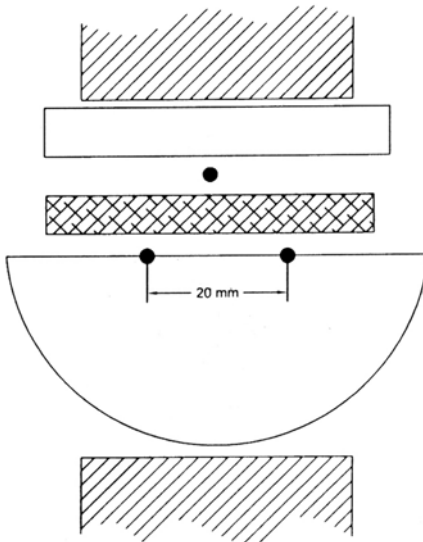


Fig. 4.5: The three-point bend test fixture

Crack resistance curve procedures

Crack resistance curves (G_R -curves) are essentially plots of the strain energy release rate as a function of crack extension. Using the methods outlined in 2.4.3.2, these were determined from the load-deflection plots from each single edged notch beam sample. The procedure followed for G_R – curve calculation consisted of two parts; finding the crack length and calculating G_R .

In order to find the crack length, it is assumed that unloading cycles would intersect the origin of the test record, as shown in Fig. 4.6. The crack length at any point on the test record is then found by the following steps:

1. Correct the sample load-displacement curves for machine deflection.
2. Calculate the initial compliance C_0 corresponding to the initial crack length a_0 .
3. Calculate $C(a_i)$ corresponding to crack length a_i from the inverse slope of the straight line which is drawn from the point (P_i, δ_i) on the load-deflection plot to the origin. Typically, 5 points are used for each test.
4. Substitute C_i into the following equation and using the trapezoidal rule for the integration, solve for the crack length, a_i :

$$C(a) = \underbrace{L^3 / 4EBW^3}_{\text{compliance of uncracked beam}} + \underbrace{9(1-\nu) L^2 / 2EBW^2 \int_0^a Y^2(a/W) d(a/W)}_{\text{compliance due to the crack}} \quad (4.27)$$

where E =experimentally determined elastic modulus, ν = Poisson's ratio of the material, L , a , B , W and Y are defined in eq. (4.25)

The instantaneous strain energy release rate is then calculated from:

$$G_R = b/C (\partial C / \partial a) \delta P / 2b \quad (4.28)$$

where $b/C (\partial C / \partial a) = \eta_{EL} = 2$ (For the case of the three-point bend specimen with span/width ratio = 4, $\eta_{EL} = 2$).

The G_R -curve is then created by plotting the instantaneous crack resistance versus the change in crack length, $a_i - a_0$.

Fracture surface energy procedures

The fracture surface energy, Γ , is a measure of the amount of work required to propagate an existing crack through the sample. If crack growth is completely stable, Γ can be determined by dividing the area under the load-deflection plot (the work of fracture) into the total fracture surface area, A .

$$\Gamma_{\text{wof}} = \text{Work of fracture} / 2 \cdot A$$

Chevron notched beam (CNB) were fabricated from elastic modulus test bars. Notching was performed with the same equipment used for the single edged notched beam samples. One side of the Chevron notch was cut, then the sample turned over to cut the other side. The resulting isosceles triangle had an average height of 3 mm and a base equal to the sample width, which is also 3 mm. As the crack encounters an ever increasing amount of material as it grows, this configuration results in stable, failure of the sample. The specimens were tested in three point bend fixture with an outer span of 20 mm and a loading rate of 0.025 mm/min. After complete specimen fracture, the area of Chevron shaped ligament was measured, and work of fracture was calculated. The fracture surface energy was also estimated from the work required to fracture the single edge notched beam samples, using the same procedure.

4.2.4 Thermal effects prediction

Cylindrical specimens (diameter, 6 mm x length, 7 mm) were impacted diametrically in the Clegg impact tester (Model: HM – 700, Make: Gilsons, Inc. U.S.A). The tester is equipped with a bellows-sealed impact chamber and a 20 kg steel ball with a drop of 525 mm. The resulting particle size distributions and cumulative volume fraction were measured by computerized inspection system analyzer (Model: CIS – 100, Make: Galai Israel). Similar procedure was adopted for cryo-treated samples except that the samples were dipped in liquid nitrogen for 15 minutes before any impacting experiments were conducted. The size

distribution data enabled to determine the two parameters of log-normal probability function, D_g and σ_g , where D_g corresponds to 50% of the cumulative volume fraction and σ_g is determined as the ratio of 84% size to 50% size.

The calculation of the local temperature rise ΔT in terms of the log-normal parameters and material properties is

$$\Delta T = 1/ C_v (dW/dV) \quad (4.29)$$

where (dW/dV) is given by eq. (2.39) and

$$dS/dV = S_n p(u_v + \ln \sigma_g) / V_n p(u_v) \quad (4.30)$$

where $p(u_v)$ is the normal probability density function, evaluated for u_v , a function of particle diameter, D , described in items 5 and 6 of the section 2.3.2 and S_n / V_n given by eq. (2.21). For a given D , log-normal parameters allow ΔT to be calculated for a particular fracture particulate.

The various properties needed for the complete description of thermal effects of fracture particulates such as combined strength parameter, energy density and surface volume ratio were calculated respectively, from eq. (2.7), (2.39) and (4.30).

4.2.5 Parametric Finite element studies

One of the greatest weakness of analytical models of the fracture process is that they are mechanistic. That is they assume a certain type of crack-microstructure interaction and then calculate the effect on the material's resistance to fracture. The establishment of computer based fracture simulation helps to determine how the structure, stress state and crack geometry influence the fracture of food materials such turmeric. By modeling the composite structure with finite elements, the combination of fiber and fiber/matrix interface properties, the mechanism of resistance to fracture can be determined. It is easy to vary the properties of the fiber and the interface during model definition, and then assess the effect on the fracture behaviour of the matrix.

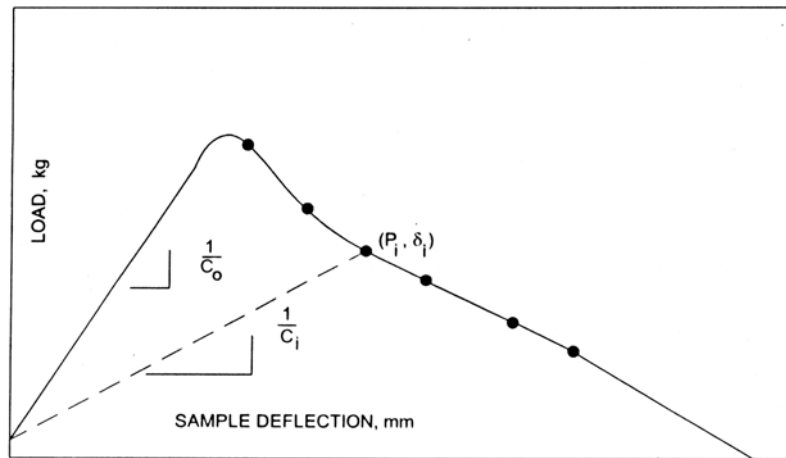


Fig. 4.6: Data analysis for G_R -curve calculation

4.2.5.1 Finite element procedures

As spices like turmeric, are fibrous and starchy (Max, 1992) the approach taken here is to consider turmeric as a composite structure of fibers and taking a two dimensional slice through a composite, containing a single fiber near the crack tip. The individual structural parameters which are varied are the fiber orientation, the residual stress state and the interface bond strength. This permits the isolation of the effects of each of these attributes on the material's fracture behaviour. Even though the micro mechanical studies do not result in quantitatively exact predictions of a material's fracture properties, they produce useful information regarding the behaviour of a crack as it approaches, intercepts and passes a fiber. The crack growth algorithm, which is based on the following procedures is summarized in Fig. 4.7.

4.2.5.2 Hardware and software

The parametric finite element studies were performed on a Pentium II based personal computer. The software used for the model generation and solution is the general purpose stress and vibration analysis program MSC/Pal 2 (1989). The MSC/Pal 2 package consists of a preprocessing program (MOD2), two matrix assembly programs (MSCPAL 2 and ASSEM2), a static solution/data output program (STAT2) and a graphical postprocessor (VIEW2). Because each subprogram is interactive, extensive use was made of DOS batch processing files to call each subprogram and to pipe in the required data. In addition, a Microsoft Fortran program (Appendix B) was written which reads MSC/Pal 2 data files and calculates the model's strain energy.

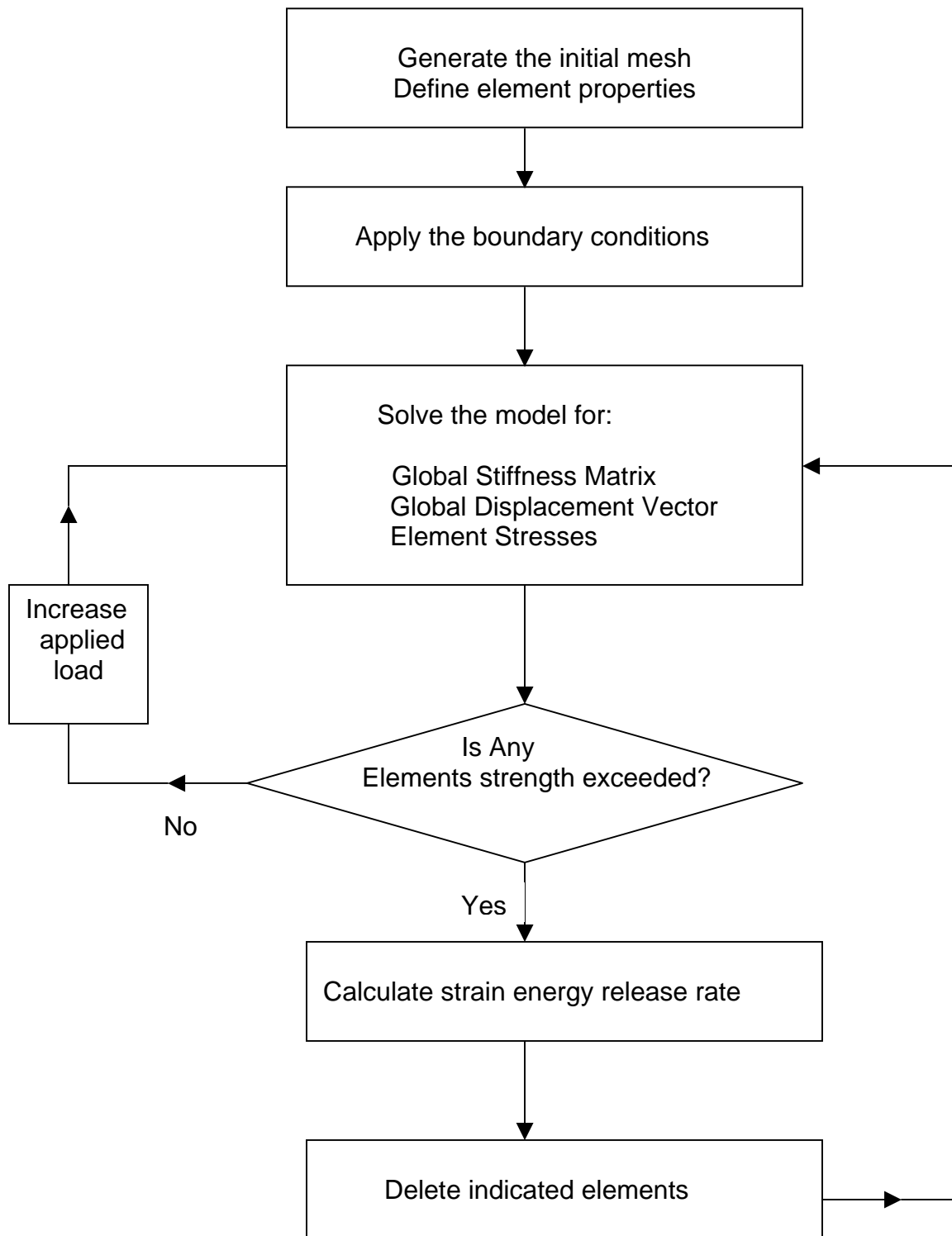


Fig. 4.7: The crack growth algorithm

4.2.5.3 Crack tip geometry modeling

Model definition

Linear, isotropic, plane strain elements are used exclusively in this study. No singular form crack tip elements are used so that progressive failure can be modeled without changes in the mesh. Use of special singular form crack tip elements would require a change in element configuration when the crack tip location changes.

Geometry

The model geometry used for the parametric micro mechanical crack growth studies is a 6mm long, 2mm wide, 10 μm thick single edge notched piece of turmeric, with a starting crack length of 0.84×10^{-3} m, as shown in Fig.4.8. A fine, uniform mesh of 10 x 10 μm quadrilateral elements is used in the crack tip core region. The remainder of the solid is modeled with coarser quadrilateral elements. Triangular elements are used for mesh size transition and for connecting an inclined fiber to the uniform crack tip mesh. The sides of the triangular fiber connection elements are approximately the same size as the core region quadrilateral elements. The choice of triangular and quadrilateral elements were arrived at after taking into account the computational time involved and the accuracy of the results with reference to the analytical results. Plots of the crack tip region finite element meshes are shown in Fig. 4.9.

The fiber is modeled with one row of elements whose length and cross sectional area are chosen to approximately simulate a fiber of turmeric. The fiber had an average diameter of 10 μm and the length of the fiber was 200 μm . The center of each fiber was located approximately 0.17×10^{-3} m in front of the crack. Five fiber orientations with respect to the crack plane are considered: 90, 60, 45, 30 and 0° . This required the generation of finite element mesh for each orientation. Individual element properties are defined so as to model the matrix, the fiber and fiber to matrix interface.

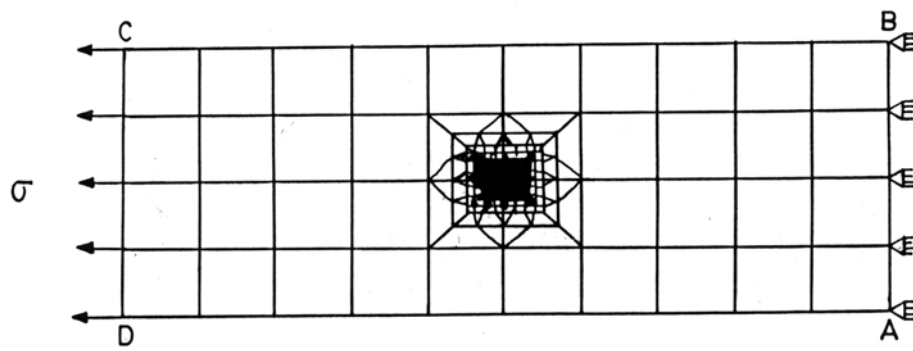


Fig. 4.8: The finite element model

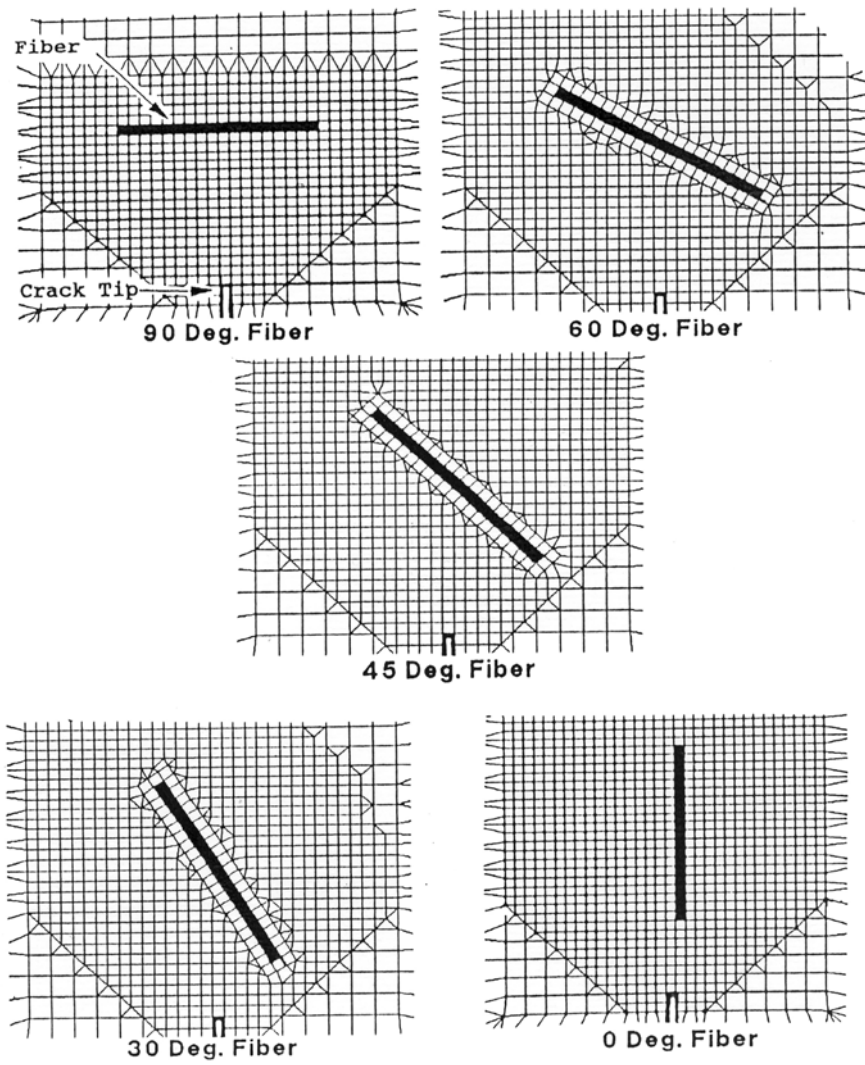


Fig. 4.9: Details of crack tip meshes

Mechanical properties which are not varied include:

- the matrix elastic properties, thermal diffusivity and fracture strength
- the interface elastic properties and thermal diffusivity
- the fiber elastic properties and fracture strength

Constituent material properties

The elastic modulus, Poisson's ratio of the matrix and interface elements and fibers are those of test data generated for turmeric. Thermal diffusivity values correspond to published experimental results (Kachuru and Alam, 1994). Studies were conducted by varying the thermo-mechanical properties of the fiber. The material properties used are tabulated in Table 4.1, along with the list of parametric analyses performed. Though the results based on the thermo-mechanical properties chosen are probably error prone, the basic purpose of selecting these constituent properties is to study and analyse the crack growth under the influence of two different elemental properties. Three different states of residual stresses are modeled by changing the thermal diffusivity values. Fiber A has a thermal diffusivity magnitude greater than that of the matrix. Fiber B has thermal diffusivity equal to that of matrix, and fiber C has a negative thermal diffusivity.

Three interface fracture strengths are considered. These are an interface with strength equal to the matrix strength, one equal to one-half of the matrix strength, and interface strength of zero. This last case represents a fiber that is completely debonded from the matrix and is crudely approximated as a hole in the mesh. The combination of three residual stress states and three interface strength levels results in the seven parametric case studies summarized in Table 4.2. Five fiber orientations per case yield a total of 35 different finite element methods.

	Matrix	Interface 1	Interface 2	Interface 3	Fiber A	Fiber B	Fiber C
E	2.50	2.50	2.50	2.50	4.87	4.87	4.87
ν	0.33	0.33	0.33	0.33	0.33	0.33	0.33
α_{th}	0.5	0.5	0.5	0.5	5.0	0.5	-1.1
S_c	14	14	7	0	28	28	28

Table 4.1: Matrix, interface and fiber properties *

* E ($\times 10^9$ Pa) – Young's modulus; ν - Poisson's ratio; α_{th} ($\text{cm}^2/\text{sec} \times 10^{-4}$) – Thermal diffusivity; S_c ($\times 10^6$ Pa) – Fracture stress

Case	Thermal diffusivity ($\text{cm}^2/\text{sec} \times 10^{-4}$)	Interface fracture stress ($\times 10^6$ Pa)
A – 1	5.0	14
A - 2	5.0	7
B – 1	0.5	14
B- 2	0.5	7
C- 1	-1.1	14
C – 2	-1.1	7
D	---	0

Table 4.2: Summary of parametric FEM case studies

Boundary conditions

The analyses that follow consider only plane (x-y) deformations, so that the translation in the z-direction and the rotations about the x-,y-, and z-axes for all of the nodes are set to zero. That is: $u_z = \theta_x = \theta_y = \theta_z = 0$ (all nodes). One end of the plate was fixed, so that the x-translation of the nodes on the line A-B is zero. For the model to be statically determinate, the y-translation of point A is also to be zeroed. These conditions can be expressed mathematically as:

$$\begin{aligned} u_x &= 0 \\ &\text{nodes on A-B} \\ u_y &\Big| = 0 \\ &\text{nodes on A-B} \end{aligned} \quad (4.31)$$

An uniformly applied stress is simulated by point forces at the nodes along the line C-D in Fig. 4.8. First, the magnitude of the stress and the cross sectional area of the turmeric test bar are used to calculate the total equivalent force. Next the total force is divided by 2 times the number of elements along the line, yielding the force to be applied to each node of the element. When two elements share a node, the total force at that node is the sum of the contributions from each element.. Using the mesh reported as before, a far field stress that would cause a K_t of 1 was applied and simply looked at the stress in the element at the crack tip. Although the values of K_t were estimated under different conditions, the literature values similar to such conditions show that a K_t of 1 would be sufficient to cause crack growth (Murakami, 1993). So the initial applied crack tip stress intensity factor used in this study was 1.0. The value of equivalent applied stress used for models containing the fibers A, B and C was 9.72 MPa. The residual stresses, which result from the cooling of turmeric from the ambient temperature, are simulated by applying a negative 10⁰C temperature differential to each node in the model.

Crack advance criterion and simulation

An iterative procedure is used to determine when and where the crack will propagate. After solution, the node point stresses and the element principle

stresses are output by the Pal2 program. Crack advance is based upon the maximum principle stress criterion, which states that fracture proceeds in the direction normal to the maximum principle stress at the crack tip (Shen, 1995). This assumes that the crack extends under a locally opening mode (Mode I). If the element principal stress at a distance of 5 μm from the crack tip exceeds a critical value, crack growth is simulated by deleting the element from the finite element mesh. The critical value of course depends on the element size as well as the material. This vanishing element technique was shown to give good results by Tvergaard (1996).

There is fundamental incompatibility between the theoretically singular stresses at the crack tip and finite element method. So the critical stress value for the fracture criterion is dependent on the finite element mesh size used. The strength value used in this study was obtained by calculating the far-field stress, for a known geometry, which results in a crack tip stress intensity factor K_I , which is equal to critical plane strain fracture toughness of each constituent material. This stress was applied to the finite element model with the 10 x 10 μm crack tip core region mesh size, and the stress at a distance of 5 μm from the crack tip (one-half the fiber diameter) was calculated to be 14 MPa. This was the value used for subsequent crack growth predictions. While this strength value is somewhat approximate, it is of the same order of magnitude as the stress predicted by linear elastic fracture mechanics theory. (Atkinson and Craster, 1995).

Strain energy release rate computation

The effect of the fracture path and the microstructure on the stress intensity at the crack tip is monitored by calculating the strain energy release rate parameter after each increment of crack growth. The strain energy release rates calculated for the finite element models are denoted as G' which is given by

$$G' = U_2 - U_1 / B (a_2 - a_1) \quad (4.32)$$

where B is the model thickness, U_1 and U_2 are the strain energies corresponding to crack lengths a_1 and a_2 respectively.

4.2.5.4 Temperature distribution simulation

Recognizing the fact that turmeric would experience stresses due to temperature gradient during size reduction and since it is difficult to view temperature distribution inside turmeric, a steady-state conduction situation is assumed in order to infer and analyze temperature distribution patterns in the turmeric based on simulation, despite the temperature distribution is non-linear or transient in the real sense.

The property values used in the finite element calculations are summarized in Table 4.3. Two sets of boundary conditions are considered: (i) Top face of the product, 25°C; Bottom face of the product, 25°C; Lateral surface, - 8°C and (ii) Top face of the product, 25°C; Bottom face of the product, 0°C; Lateral surface, 0°C. The average moisture content of the product was taken as 12.5%. Three product volumes (9.1×10^{-7} , 26.56×10^{-7} , and $46.33 \times 10^{-7} \text{ m}^3$) were chosen based on the average size of turmeric available. Cylindrical shape was considered in the study. For the shape considered, the length to diameter ratio was varied between 0.25 to 1.00, keeping the volume constant. This restriction on keeping the volume same, was to ensure that all the products (of same volume) have the same heat capacity, thus giving a standard for comparing the distributions obtained for different aspect ratios.

The FEM aspects of the simulations adopted are as follows:
Elemental configuration – SOLID 87, 3-D, 10 node tetrahedral thermal solid;
Degree of freedom – Temperature, single degree of freedom at each node;
Solver – Ansys Frontal. The elemental configuration of 665 elements was selected after considering the accuracy and computation time involved (Jia et al., 2000). The elemental temperatures were obtained by averaging the values at the ten nodes which comprise the element and the temperature distribution is predicted according to the nodal solution. The FEM calculated results were compared with the analytical solution for a simplified problem of different elemental configurations (Carslaw and Jaeger, 1996).

Property	Ambient sample	Cryo-treated (-8 °C) sample	Source
Thermal conductivity (W/m°C)	0.458	0.326	Kachuru and Alam, 1994
Specific heat (kJ/kg°C)	1.641	1.641	Kachuru and Alam, 1994
Density (kg/m ³)	1300	1800	
Length (m)	1×10^{-2}	1×10^{-2}	
Diameter (m)	7×10^{-3}	7×10^{-3}	

Table 4.3: Summary of material properties of turmeric used for the FEM simulation of temperature distribution

The deformation behavior in terms stress and strain for turmeric (size: diameter, 10.6×10^{-3} m and length, 52.5×10^{-3} m), under ambient and low temperature conditions as determined by the stress -strain test is shown in Fig. 5.1. Observations were similar for other sizes and conditions. The values of properties estimated, such as modulus of elasticity, deformation loads, fracture stress and strain energy values at different interface temperatures are summarized in Table 5.1 for (a) variation in volume and (b) variation in length-to-diameter (L/D) ratio keeping the volume constant. The maximum stress intensity values, as obtained from the finite element analysis under ambient and low temperature conditions are also included in the Tables 5.1 (a) and (b). Table 5.2 presents hardness, toughness and brittleness values of turmeric (size: diameter, 10.6×10^{-3} m and length, 52.5×10^{-3} m) under ambient and cryogenic conditions (-8°C). A descritized finite-element grid of turmeric is shown in Fig. 5.2 (a). Plots of stress distribution along with the deflection in the turmeric sample, categorized as large (size: diameter, 10.6×10^{-3} m and length, 52.5×10^{-3} m), under ambient and cryogenic conditions (-8°C) are shown in Figs 5.2 (b) and (c). Observations were similar for other volumes categorized as small (size: diameter, 6.41×10^{-3} m and length, 28.23×10^{-3} m) and medium (size: diameter, 8.92×10^{-3} m and length, 42.67×10^{-3} m). The pattern of stress distribution, along with deflection and stress intensity values under different L/D ratios (0.25,0.50 and 1.00) under cryogenic conditions (-8°C) are shown in Figs 5.3 (a) - (c). Similar observations were made for ambient conditions. Fig. 5.4 shows the load-deflection plot of the single edge notched beam test bar of turmeric under ambient and cryogenic conditions (-8°C). The values of Poisson's ratio under ambient and low temperature conditions were found to be 0.33. The range of densities were between $1190 - 1350 \text{ kg/m}^3$ under ambient conditions whereas under cryogenic conditions it was in the range of $1780 - 1812 \text{ kg/m}^3$.

The properties estimated (Tables 5.1 a, b and 5.2) reveal that strength and hardness are important parameters governing size reduction. It can be seen

that the modulus of elasticity and maximum stress intensity values increase with the decrease in size (Table 5.1 a) which means an increased particle strength under lower particle sizes. For example, modulus of elasticity and maximum stress intensity values under ambient conditions were found to be in the range of $2.1 \times 10^9 - 6.9 \times 10^9$ Pa and $5.5 \times 10^6 - 10.2 \times 10^6$ Pa respectively whereas under cryogenic conditions (-8°C) it was in the range of $4.9 \times 10^9 - 20.9 \times 10^9$ Pa and $9.2 \times 10^6 - 23.6 \times 10^6$ Pa when the size of the sample reduced from large (size: diameter, 10.6×10^{-3} m and length, 52.5×10^{-3} m) to small (size: diameter, 6.41×10^{-3} m and length, 28.23×10^{-3} m). Also modulus of elasticity and stress intensity values increase as the temperature is reduced. For example the increase in modulus of elasticity and stress intensity values respectively as the temperature was reduced from -8 to -62°C were: 4.9 to 6.3×10^9 Pa and 9.2 to 10.9×10^6 Pa (size: diameter, 10.6×10^{-3} m and length, 52.5×10^{-3} m). All these indicate more stiffness, which means less material deformation on application of fixed force.

For an increase in volume, there was an increase in strain energy indicating wider stress distribution throughout the material (Table 5.1 a). For example, it increased from 10.6 to 33.4×10^{-3} N-m under ambient conditions and under cryogenic conditions (-8°C) the increase was from 12.1 to 40×10^{-3} N-m. Strain energy also increased as the temperature is reduced. For example, the strain energy increased from 40×10^{-3} to 43.7×10^{-3} N-m (size: diameter, 10.6×10^{-3} m and length, 52.5×10^{-3} m) as the temperature was reduced from -8°C to -62°C . With the volumes remaining constant and for different length to diameter, ratios (0.25, 0.50 and 1.00), strain energy increased with an increase in L/D ratios under ambient and cryogenic conditions indicating more stress concentration (Table 5.1 b). For example, in the sample categorized as large, strain energy increased from 0.54×10^{-3} to 3.9×10^{-3} N-m under ambient conditions and under cryogenic conditions (-8°C) it increased from 1.1×10^{-3} to 5.1×10^{-3} N-m, as the L/D ratios increased from 0.25 to 1.00.

As indicated in Table 5.2, as the brittleness and hardness increases, toughness decreases which means, that resistance to deformation increases and

resistance to fracture decreases. Hardness is the resistance to deformation and toughness is the resistance to fracture (Prasher,1987). The ultimate stress, modulus of elasticity and stress intensity values, increase from ambient to low temperature conditions (Tables 5.1 a and b) indicating increase in hardness. For example, under ambient conditions (size: diameter, 10.6×10^{-3} m and length, 52.5×10^{-3} m), values of ultimate stress, modulus of elasticity and maximum stress intensity respectively were: 3.4×10^6 Pa, 2.1×10^9 Pa and 5.5×10^6 Pa and under low temperature conditions with the temperature range -8°C to -62°C , values of ultimate stress, modulus of elasticity and maximum stress intensity values respectively were in the range of 3.6×10^6 to 5.7×10^6 Pa, 4.9×10^9 to 6.3×10^9 Pa and 9.2×10^6 to 10.9×10^6 Pa. The threshold parameters such as critical load and corresponding critical length (Table 5.2) indicate that $F^* \ll F$, (applied load F , threshold load F^* and crack length 'a' under ambient and cryogenic conditions (Temp. -8°C), respectively were: F - 11.30 and 6.89 N, F^* - 0.7 and 0.5 N, a - 5 and 3 μm), and thus the process of breakage or damage of turmeric is essentially a fracture and is not deformation-controlled.

Table 5.3 shows the values of estimated stress intensity factors, K_t under ambient and cryogenic conditions for the turmeric sample (size: diameter, 10.6×10^{-3} m and length, 52.5×10^{-3} m). The values of (K_t) were to found be in the range of 1.1 - 3.9 under ambient conditions where as under cryogenic conditions (-8°C), it was found to be in the range of 1.3 – 3.4. For the other categorized samples it was found to be in the range of 1.4-3.6 under ambient conditions and 1.4 – 3.8 under cryogenic conditions. Similar observations were made for other temperatures. Considering the three volumes between 9.1×10^{-7} to 46.33×10^{-7} m^3 it was found that stress intensity factor increases as the deflection increases and radius of curvature decreases, indicating the presence of localized stresses. For example, as indicated in the Table 5.3, under ambient conditions stress intensity factor, K_t increases from 1.1 to 3.9, as the deflection increases from 0.01 to 0.07×10^{-3} m and the radius of curvature decreasing from 49.7×10^{-3} m to 4.7×10^{-3} m where as under cryogenic conditions stress intensity factor

increase was from 1.3 to 3.4, for an increase in deflection from 0.02 to 0.07×10^{-3} m and a decrease in radius of curvature from 17.3 to 4.9×10^{-3} m.

As seen from the Figs 5.3 (a to c), product volume and length to diameter dimension ratios (L/D) have pronounced effect on stress intensity. It appeared to be more concentrated at the outer layer or circumference of the product than the rest. It was observed that stress intensity values increased as length to diameter dimension ratio increased, whereas it decreased for an increase in volume. For example stress intensity values in the sample with a volume, $46.33 \times 10^{-7} \text{ m}^3$ (size: diameter, 10.6×10^{-3} m and length, 52.5×10^{-3} m) increased from 0.7×10^6 Pa to 1.9×10^6 Pa, under ambient condition (Table 5.1 b) and in cryogenic condition from 1.5×10^6 to 3.3×10^6 Pa (Figs 5.3 a to c) as the length to diameter increased from 0.25 to 1.0. Considering the three volumes, between 9.1×10^{-7} to $46.33 \times 10^{-7} \text{ m}^3$, categorized as small, medium and large, stress intensity value decreased from 2 to 0.7×10^6 Pa, 2.3 to 1.4×10^6 Pa and 2.7 to 1.9×10^6 Pa respectively under ambient conditions and during cryogenic conditions the decrease was from 4.4 to 1.5×10^6 Pa, 5.1 to 2.3×10^6 Pa and 7.4 to 3.3×10^6 Pa respectively as the length to diameter dimension ratio, increased from 0.25 to 1.00. Increasing the value of length to diameter dimension ratio keeping the volume constant, results in decreasing radius of the sample. Consider a product of volume equal to $46.33 \times 10^{-7} \text{ m}^3$, the radius decreases from 42×10^{-3} m to 26×10^{-3} m, when the height to base dimension increases from 0.25 to 1.0.

Ambient Conditions						
Category	Modulus of elasticity E' (x 10 ⁹ Pa)	Deflection (x 10 ⁻³ m)	Maximum Stress intensity (x 10 ⁶ Pa) ^a	Strain energy (x 10 ⁻³ N-m)	Ultimate stress (x 10 ⁶ Pa)	
Small: L-28.23 (x 10 ⁻³ m) D-6.41 (x 10 ⁻³ m)	6.9 ± 0.2	0.02 ± 0.01	10.2	10.6	16.6 ± 0.5	
Medium: L-42.67 (x 10 ⁻³ m) D-8.92 (x 10 ⁻³ m)	4.2 ± 0.1	0.02 ± 0.01	6.1	11.8	6.2 ± 0.1	
Large: L-52.5 (x 10 ⁻³ m) D-10.6 (x 10 ⁻³ m)	2.1 ± 0.1	0.04 ± 0.02	5.5	33.4	3.4 ± 0.3	
Cryogenic conditions						
						Temp (°C)
Small: L-28.23 (x 10 ⁻³ m) D-6.41 (x 10 ⁻³ m)	20.9 ± 0.2	0.01 ± 0.01	23.6	12.1	34.6 ± 2.3	- 8
	22.7 ± 0.2	0.01 ± 0.01	26.7	14.3	39.2 ± 2.1	- 20
	24.1 ± 0.2	0.02 ± 0.01	29.7	16.4	43.9 ± 1.6	- 42
	24.6 ± 0.1	0.02 ± 0.01	29.9	16.6	45.6 ± 1.3	- 62
Medium: L-42.67 (x 10 ⁻³ m) D-8.92 (x 10 ⁻³ m)	10.3 ± 0.1	0.02 ± 0.01	10.1	13.7	6.6 ± 0.03	- 8
	10.5 ± 0.1	0.03 ± 0.01	13.6	23.5	6.7 ± 0.02	- 20
	11.4 ± 0.1	0.03 ± 0.01	14.7	25.3	7.8 ± 0.1	- 42
	12.9 ± 0.1	0.06 ± 0.02	16.1	26.8	8.2 ± 0.1	- 62
Large: L-52.5 (x 10 ⁻³ m) D-10.6 (x 10 ⁻³ m)	4.9 ± 0.1	0.04 ± 0.02	9.2	40.0	3.6 ± 0.1	- 8
	5.1 ± 0.1	0.04 ± 0.03	9.6	41.9	3.8 ± 0.1	- 20
	5.7 ± 0.1	0.05 ± 0.04	10.2	42.3	4.1 ± 0.2	- 42
	6.3 ± 0.1	0.06 ± 0.04	10.9	43.7	5.7 ± 0.3	- 62

5.1 (a): Estimated engineering properties of turmeric under ambient and cryogenic conditions and different volumes. ^a By FEM analysis

Ambient Conditions						
Category	L/D ratio	Modulus of elasticity 'E' (x 10 ⁹ Pa)	Deflection (x 10 ⁻³ m)	Maximum Stress intensity (x 10 ⁶ Pa) ^a	Strain energy (x 10 ³ N-m)	
Small: L-28.23 (x 10 ⁻³ m) D-6.41 (x 10 ⁻³ m)	0.25	6.9 ± 0.2	0.09 ± 0.05	2	0.26	
	0.50	6.9 ± 0.3	0.04 ± 0.02	2.3	0.35	
	1.00	6.9 ± 0.3	0.03 ± 0.02	2.7	0.48	
Medium: L-42.67 (x 10 ⁻³ m) D-8.92 (x 10 ⁻³ m)	0.25	4.2 ± 0.1	0.09 ± 0.04	1.1	0.38	
	0.50	4.2 ± 0.2	0.03 ± 0.02	1.7	0.91	
	1.00	4.2 ± 0.2	0.01 ± 0.02	2.2	1.5	
Large: L-52.5 (x 10 ⁻³ m) D-10.6 (x 10 ⁻³ m)	0.25	2.1 ± 0.1	0.05 ± 0.02	0.7	0.54	
	0.50	2.1 ± 0.1	0.03 ± 0.02	1.4	2.2	
	1.00	2.1 ± 0.1	0.01 ± 0.01	1.9	3.9	
Cryogenic conditions						
						Temp (°C)
Small: L-28.23 (x 10 ⁻³ m) D-6.41 (x 10 ⁻³ m)	0.25	20.9 ± 0.8	0.03 ± 0.02	4.4	2.4	- 8
	0.50	20.9 ± 0.7	0.02 ± 0.01	5.1	3.0	
	1.00	20.9 ± 0.7	0.03 ± 0.01	7.4	7.3	
Medium: L-42.67 (x 10 ⁻³ m) D-8.92 (x 10 ⁻³ m)	0.25	10.3 ± 0.4	0.03 ± 0.01	2.3	0.7	- 8
	0.50	10.3 ± 0.3	0.01 ± 0.01	2.8	1.0	
	1.00	10.3 ± 0.4	0.01 ± 0.01	3.7	1.8	
Large: L-52.5 (x 10 ⁻³ m) D-10.6 (x 10 ⁻³ m)	0.25	4.9 ± 0.2	0.03 ± 0.02	1.5	1.1	- 8
	0.50	4.9 ± 0.1	0.03 ± 0.01	2.3	2.5	
	1.00	4.9 ± 0.1	0.04 ± 0.01	3.3	5.1	

Table 5.1(b): Estimated engineering properties of turmeric under ambient and cryogenic conditions (-8°C) and different height-to-base dimension ratios. ^a By FEM analysis

Material : Turmeric [L-52.5 x 10 ⁻³ m; D-10.6 x 10 ⁻³ m]	Deformation/ fracture parameters			Threshold parameters	
	Hardness H (x 10 ⁶ Pa)	Toughness K ₀ (x 10 ⁶ Pa m ^{1/2})	Brittleness H/K ₀ (μm ^{-1/2})	Critical load F* (N)	Critical Crack length a* (μm)
Ambient conditions	14 ± 0.4	3 ± 0.2	4.6	1.2	5
Cryogenic conditions (Temperature: (-) 8°C)	16 ± 0.7	3 ± 0.1	5.3	0.8	3

Table 5.2: Estimated hardness, toughness and brittleness values of turmeric under ambient cryogenic conditions (Temperature: - 8°C). Applied load, F - 11.30 N (ambient) and 6.89 N (- 8°C). Dimensions of the specimen – Length :52.5 x 10⁻³ m; Diameter: 10.6 x 10⁻³ m

Load N	Deflection δ (x 10^{-3} m)	σ max (x 10^6 m)	Radius of curvature(r) (x 10^{-3} m)	r/c ^a	Stress Intensity factor K_t	σ nominal (x 10^6 Pa)
			Ambient conditions			
3.1 4.7 8.9 13.3 18.9 50.2	0.01± 0.01 0.01± 0.01 0.01± 0.01 0.01± 0.01 0.01± 0.02 0.07± 0.04	0.2 ± 0.01 0.3 ± 0.01 0.5 ± 0.02 0.8 ± 0.03 1.1 ± 0.05 3.1 ± 0.2	49.7 34.1 20.9 15.6 11.8 4.7	9.4 6.4 3.9 2.9 2.2 0.9	1.1 1.1 1.3 1.4 1.5 3.9	0.17 0.26 0.43 0.59 0.74 11.9
			Cryogenic Conditions			
5.8 18.7 34.2 44.9	0.02 ± 0.01 0.04 ± 0.01 0.05 ± 0.02 0.07 ± 0.02	0.4 ± 0.02 1.1 ± 0.04 2.1 ± 0.1 2.7 ± 0.1	17.3 9.5 6.5 4.9	3.3 1.8 1.2 0.9	1.3 1.9 3.3 3.4	0.27 0.59 0.63 0.8

Table 5.3: Estimated stress intensity factors of turmeric under ambient and cryogenic conditions (-8° C). Dimension of the specimen: Length: 52.5×10^{-3} m; Diameter: 10.6×10^{-3} m. ^a c = (D/2) x 10^{-3} m.

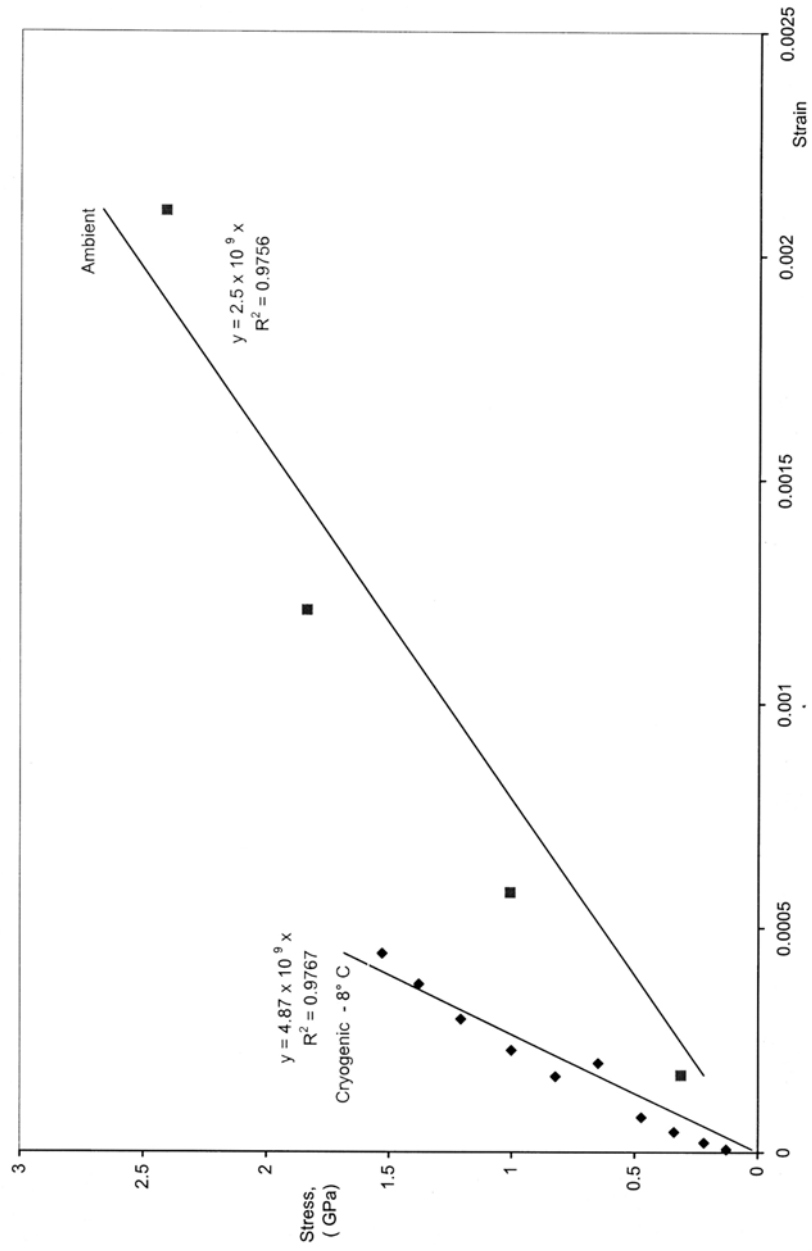


Fig. 5.1: Stress-strain relationship for turmeric under ambient and cryogenic conditions (- 8° C)

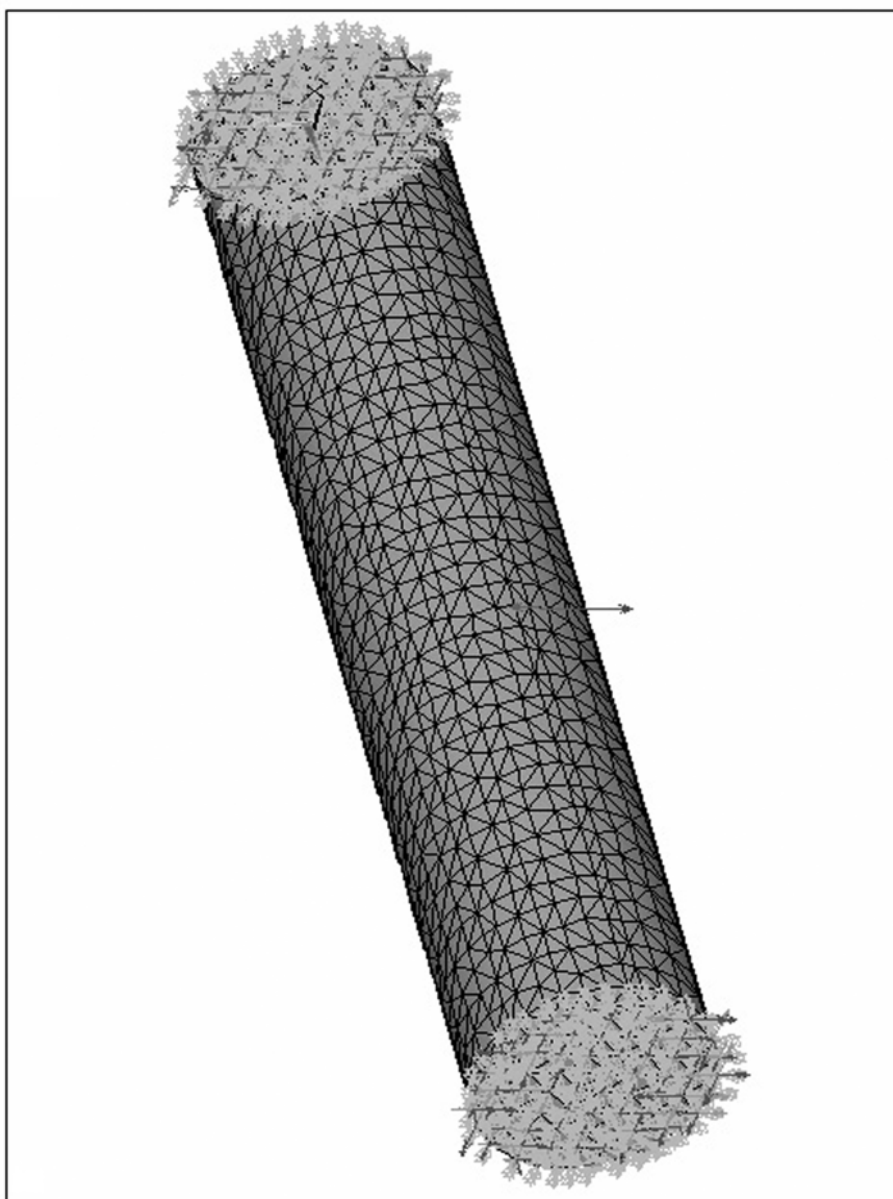


Fig. 5.2 (a): Finite element mesh for turmeric (3697 nodes and 17505 elements)

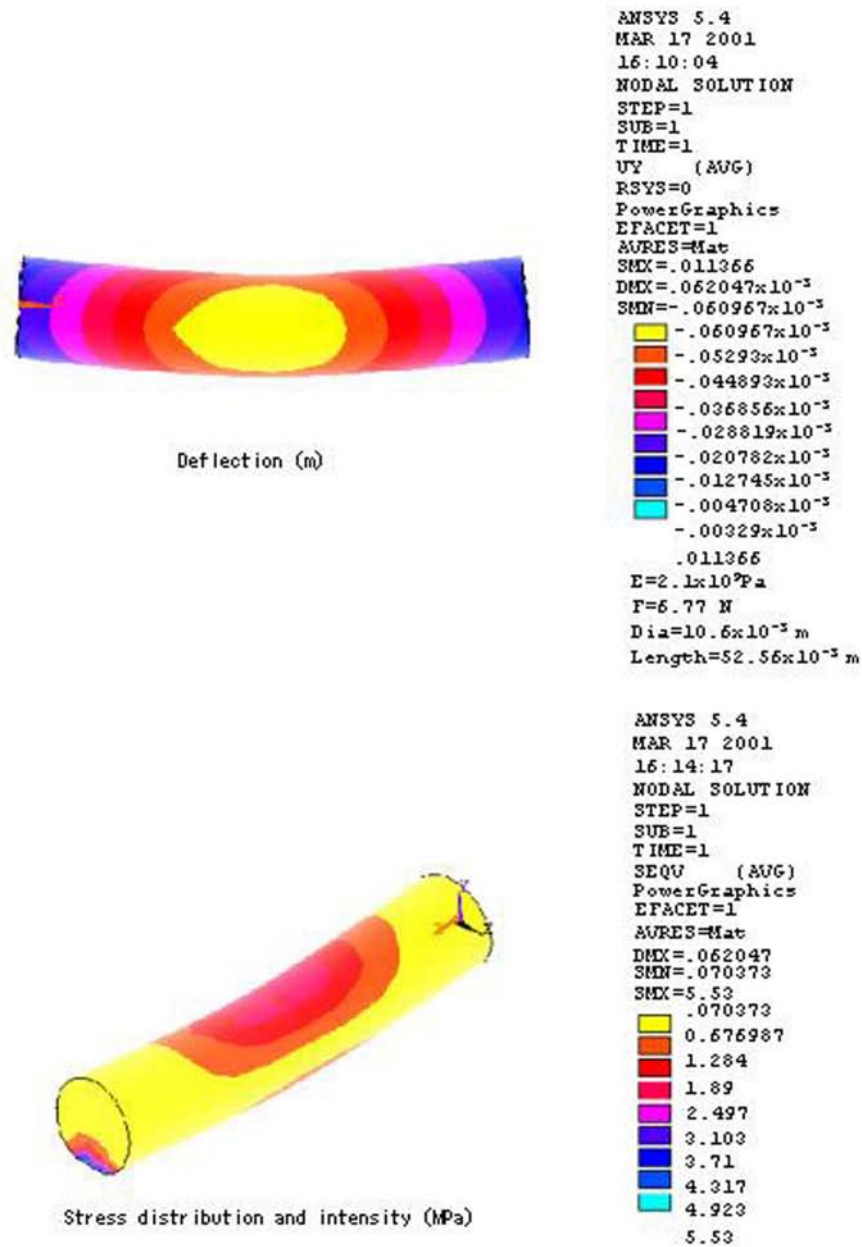


Fig.5.2(b): Deformation behaviour for tumeric under ambient conditions

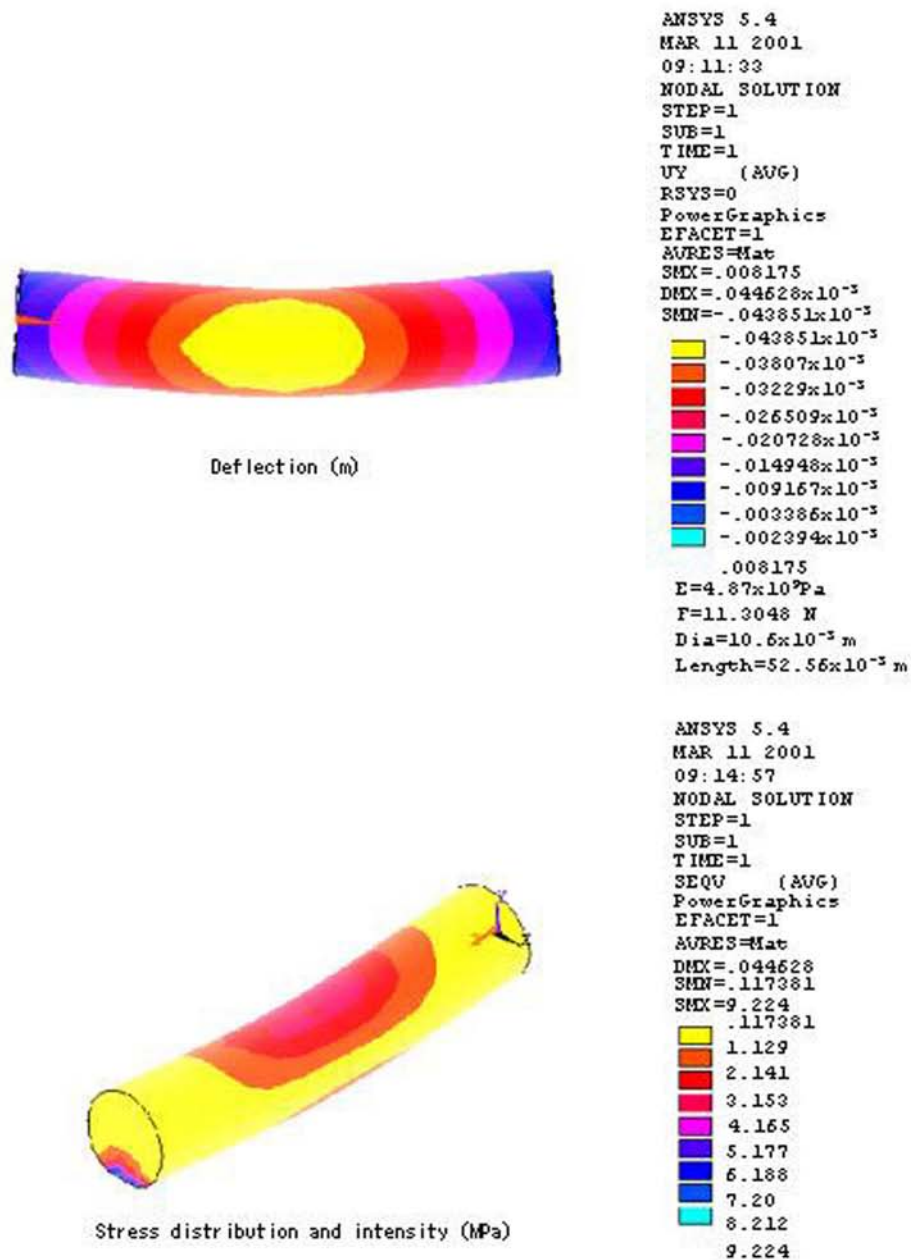


Fig.5.2(c): Deformation behaviour for turmeric under cryogenic conditions (- 8^oC)

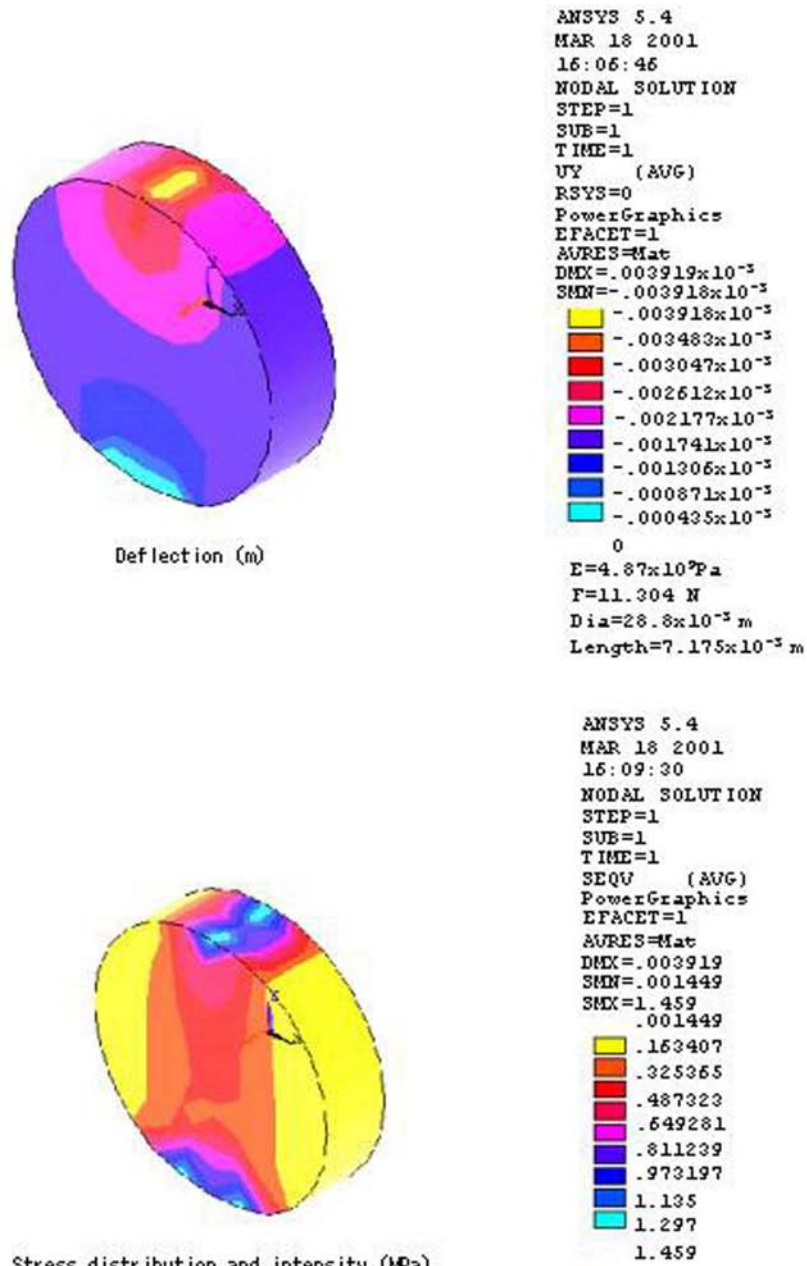


Fig.5.3(a): Deformation behaviour for turmeric at length to diameter ratio, 0.25

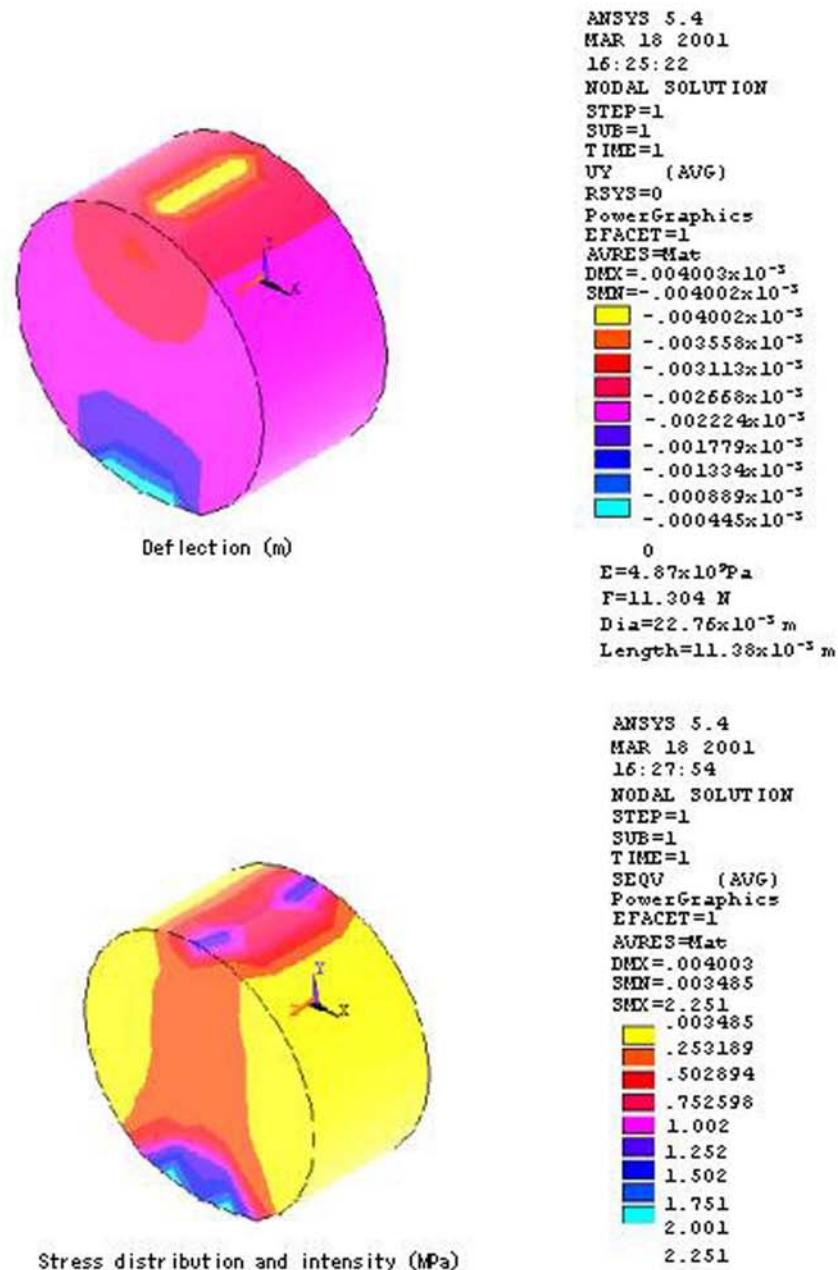


Fig.5.3(b): Deformation behaviour for turmeric at length to diameter ratio, 0.50

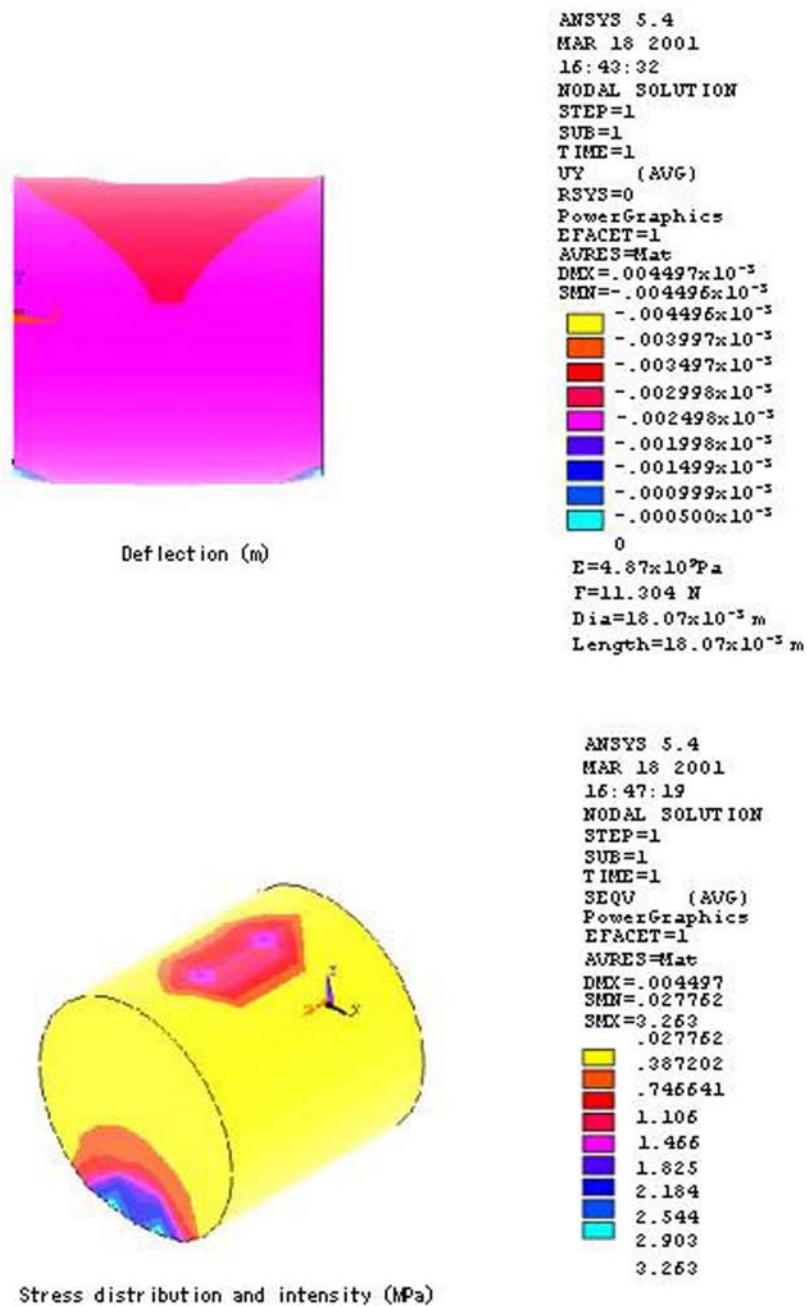


Fig.5.3(c): Deformation behaviour for turmeric at length to diameter ratio, 1.00

Crack growth resistance curve

It can be seen from Fig. 5.4 that there was a significant difference in the manner in which the turmeric samples failed after reaching the peak load. This failure mode was quantified by determining the crack resistance curve for both the ambient and cryogenically treated samples. A typical crack growth resistance curve for each of the turmeric samples is shown in Fig. 5.5. The cryogenically treated turmeric sample failed catastrophically upon reaching the peak load during testing while the turmeric sample under ambient condition exhibited failure beyond the peak load which resulted in a rising crack growth resistance curve. The slopes of these curves, calculated for the first 1 mm of crack extension, ranged between 1.8 and 5.1 (N/m)/ mm.

Fracture surface energy

The amount of energy required to create a new fracture surfaces was estimated with both the single edge notched beam tests (SENB) and Chevron notched beam (CNB) tests. Because the failure of the SENB samples was unstable for both types of turmeric samples, energy conservation was not insured. Thus, the surface energy values obtained from these tests were not taken as valid. For the Chevron notched beam sample configuration, stable crack propagation was obtained for both types of samples and true Γ_{WOF} values were expected. It was found that turmeric under ambient condition had the average specific fracture surface energy of $8.86 \pm 1.74 \text{ J/m}^2$ while the cryogenically treated sample had the average specific fracture surface energy of $5.66 \pm 1.68 \text{ J/m}^2$ which means that the Γ_{WOF} is strongly influenced by the material treatment.

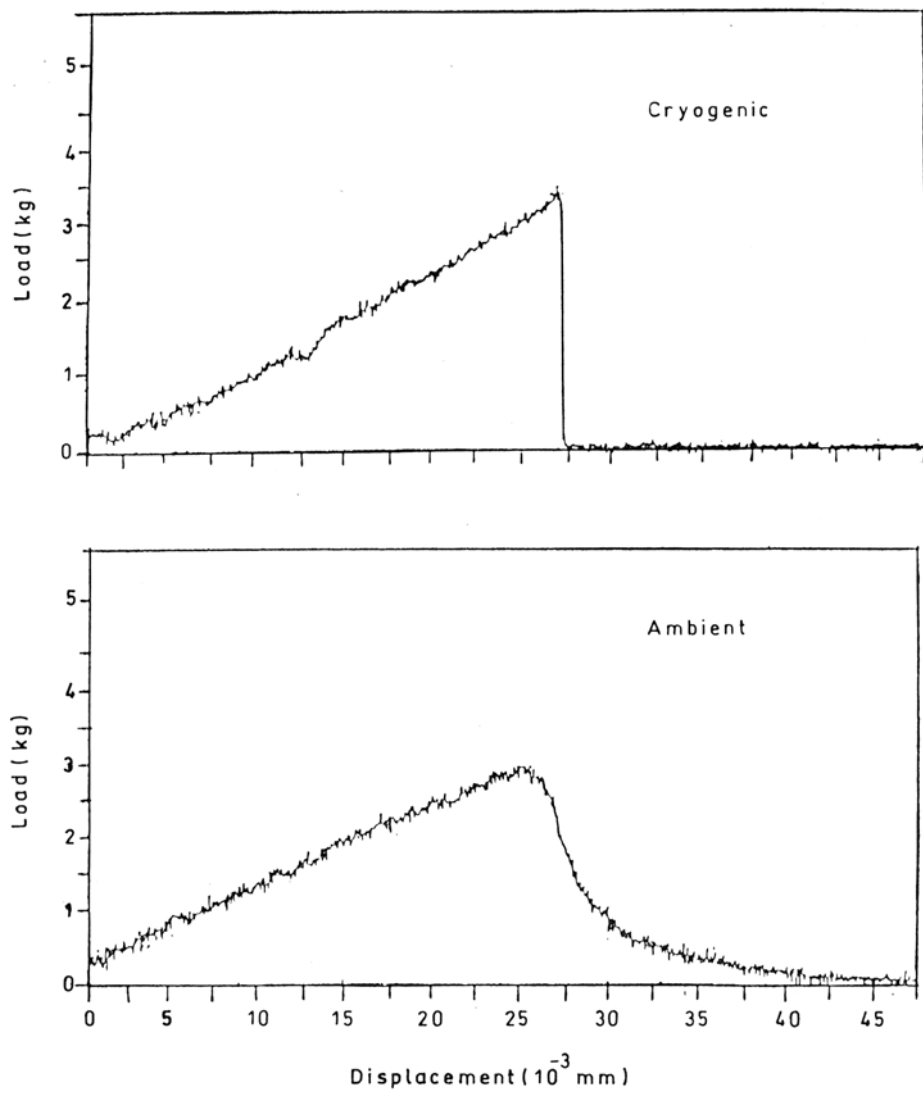


Fig. 5.4: Load-deflection plots of single edge notched beam test bar of turmeric under ambient and cryogenic conditions (-8°C)

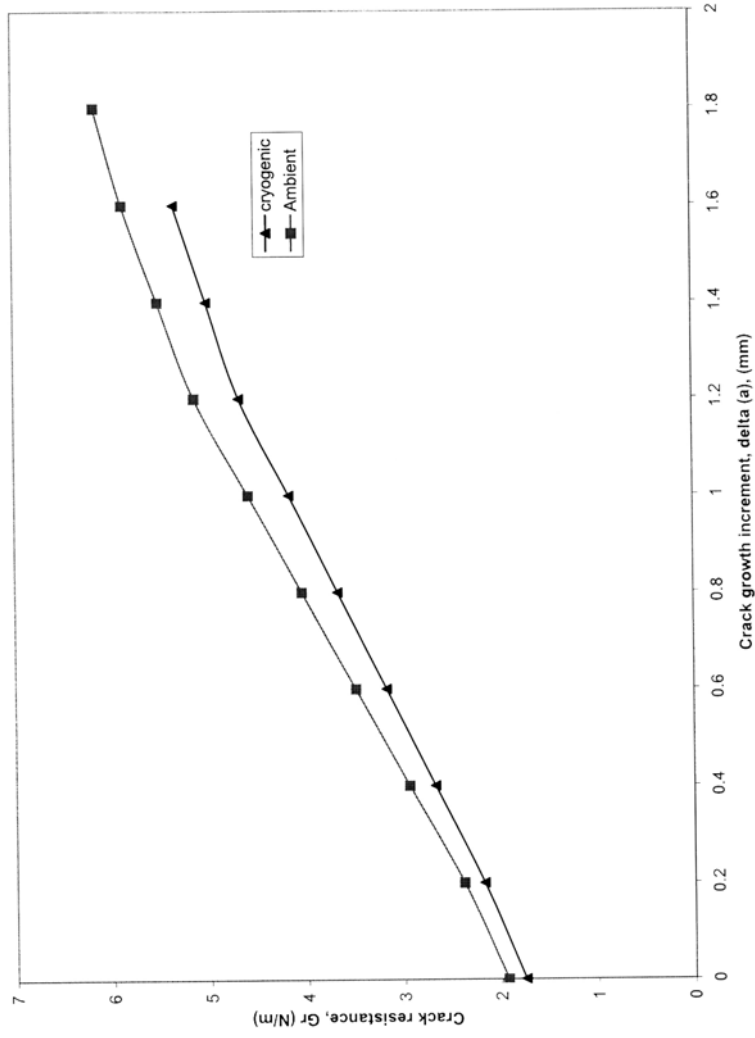


Fig. 5.5: Crack growth resistance curves for turmeric under ambient and cryogenic conditions (- 8°C)

5.2 Fracture mechanism predictions

The fracture paths predicted with these finite element models consist of a complex combination of events, the sequence of which depended upon the constituent properties and the fiber orientation. These events include self-similar crack propagation, fiber fracture, crack deflection, and interface debonding/microcracking. Physically, the strain energy release rate is the force per unit thickness required to extend the crack by an incremental amount δa . In order to compare the finite element results, the G' (Eq. 4.30) is normalized by dividing the strain energy release rate, G_I , in the absence of any fiber.

G_I was calculated from the theoretical relationship:

$$G_I = Y^2 \sigma^2 \pi a / E \quad (5.1)$$

where Y = the dimensionless geometry correction factor for the single edge-notched turmeric sample piece; σ =the applied stress; a = the crack length, measured in the Y -direction; and E = the elastic modulus of the matrix.

As shown in Fig. 5.6, the G' calculated with the finite element method is in excellent agreement with the linear elastic fracture mechanics theory.

Case (i): Thermal diffusivity of the fiber greater than the thermal diffusivity of the matrix

When the thermal diffusivity of the fiber was greater than the thermal diffusivity of the matrix, it contracted more upon cooling due to cryogenic temperature. This created residual compressive stresses parallel to the fiber axis in the matrix and a significant reduction in the stress intensity.

The combination of this residual stress state and a strong interface bond encourages crack deflection in the matrix and promotes fiber failure. The fracture path predicted for the 60° orientation of this residual stress state-interface strength combination is presented in Fig.5.7. Initially, crack extension was entirely self-similar, and the calculated strain energy release rate, G' remained nearly constant. The increased crack driving force due to increased crack length was offset by the compressive residual stresses in the matrix. When the crack

length was approximately 30 μm from the center of these fibers, the residual compression in the matrix caused it to deflect away from the fiber. The occurrence of the crack deflection resulted in a reduced strain energy release rate for that crack growth increment.

When the cracks grew to within 10 μm from the fibers, the residual tension in the fiber caused the fibers to fracture. Fiber fracture released a large amount of stored elastic energy. The primary crack then linked up with the fiber fracture and propagated beyond the fiber in a self-similar manner.

Case (ii): Thermal diffusivity of the fiber less than that of the matrix

When the fiber's thermal diffusivity was less than that of the matrix, the fiber was placed in residual compression. This had the effect of decreasing the actual stress in the fiber when it was intercepted by the growing crack, so that the fiber fracture was not predicted to occur. The weak interface promoted crack pinning and crack deflection by failing ahead of the crack. The creation of secondary crack surface via interface failure absorbed energy which would otherwise contribute to primary crack extension.

The fracture paths predicted for 90° orientation of this fiber - interface property combination are presented in Fig. 5.8 (a). When the crack grew to within 30 μm of the fiber oriented at 90° with respect to the crack plane, the interface debonded from the matrix. The primary crack linked up with the interface crack. As the crack spread along the first interface, the second interface debonded partially. The crack was locally pinned and the strain energy release rate was greatly reduced. Interface debonding also occurred when the crack approached the fibers inclined with respect to the crack plane. In these cases, the primary crack was then deflected toward and intercepted the debond crack. Crack deflection via interface failure continued to the end of the fiber.

Case (iii): Thermal diffusivity of the fiber and that of the matrix are equal

When the thermal diffusivity of the fiber and matrix are equal, no residual stresses are generated. Crack deflection in the matrix and fiber failure did not occur. Instead, the cracks propagated in self-similar manner until it intercepted the fiber. The fracture paths were similar to the fracture paths predicted with the fiber thermal diffusivity less than that of the matrix. The predicted fracture paths are shown in Figs. 5.8 (b) and (c). The similarity in behaviour is due to the fact that the magnitude of the difference between the C fiber's and matrix's thermal diffusivity is not as large as the difference between that of fiber A and the matrix.

Interface fracture strength

The primary effects of lowering the interface bond strength between the fiber and the matrix were to cause microcracking at and crack deflection along the fiber-to-matrix interface. Debonding of the fiber ends occurred for all orientations at the onset of primary crack extension. This reduced the magnitude of the residual stresses, so that crack deflection away from the fiber did not occur. Partial debonding along the fiber-matrix interface also decreased the residual tension in the fiber. The result is that fiber failure occurred only for the 90 and 60° orientations. In the other orientations the crack was deflected along the interface, as shown in Fig. 5.9. The fracture paths for 0 and 30° orientation were similar to the 45° orientation.

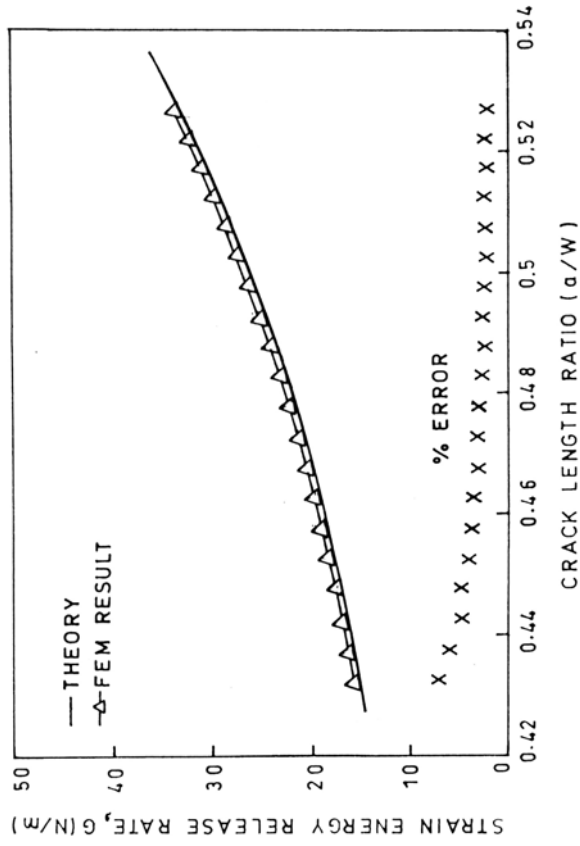


Fig. 5.6: Comparison of finite element and theoretical strain energy release rates

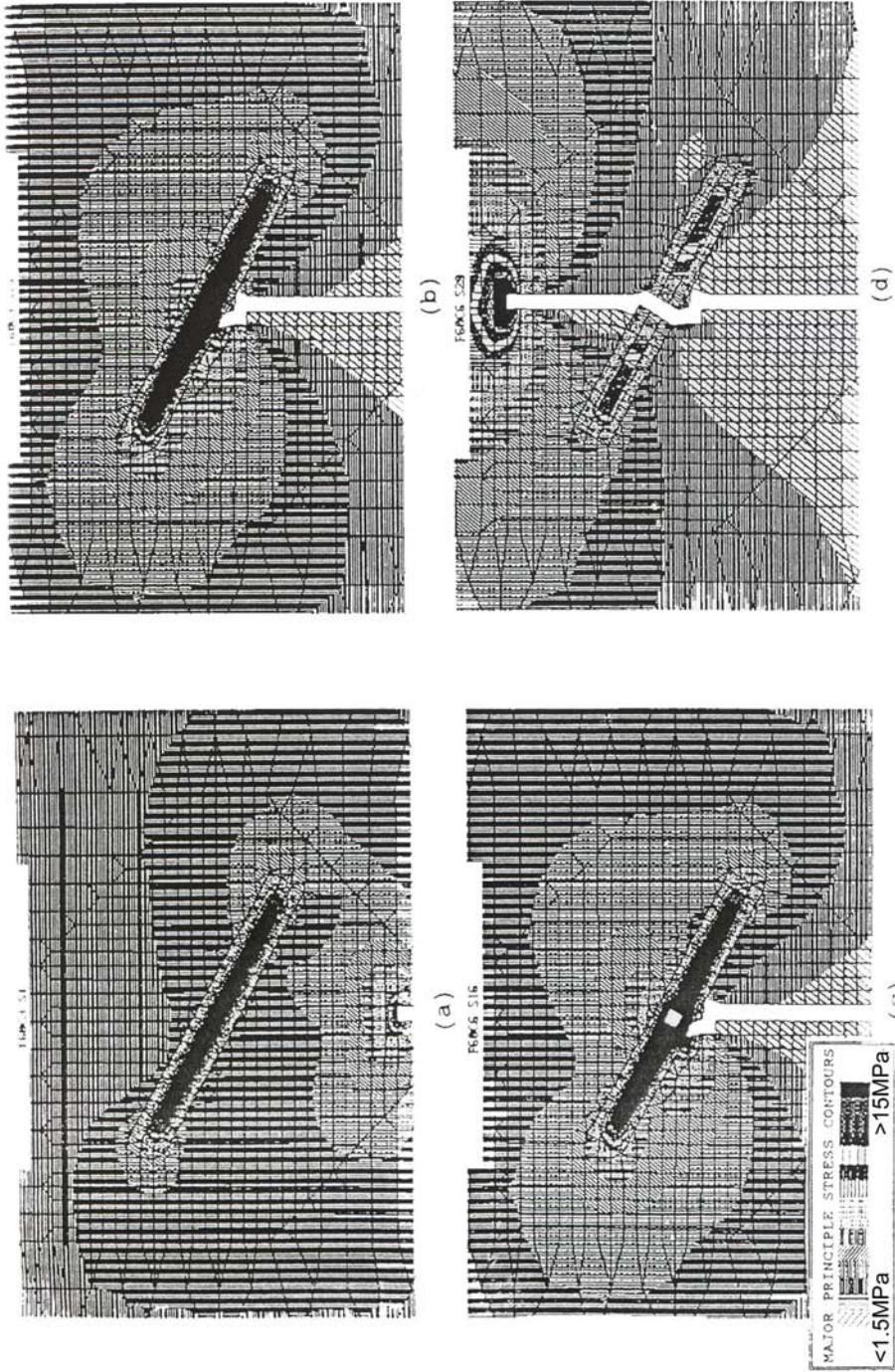


Fig .5.7 : Fracture path for $\alpha_f > \alpha_m$, strong interface, 60° orientation (a) initial configuration (b) crack deflection (c) fiber fracture (d) crack growth beyond fiber.

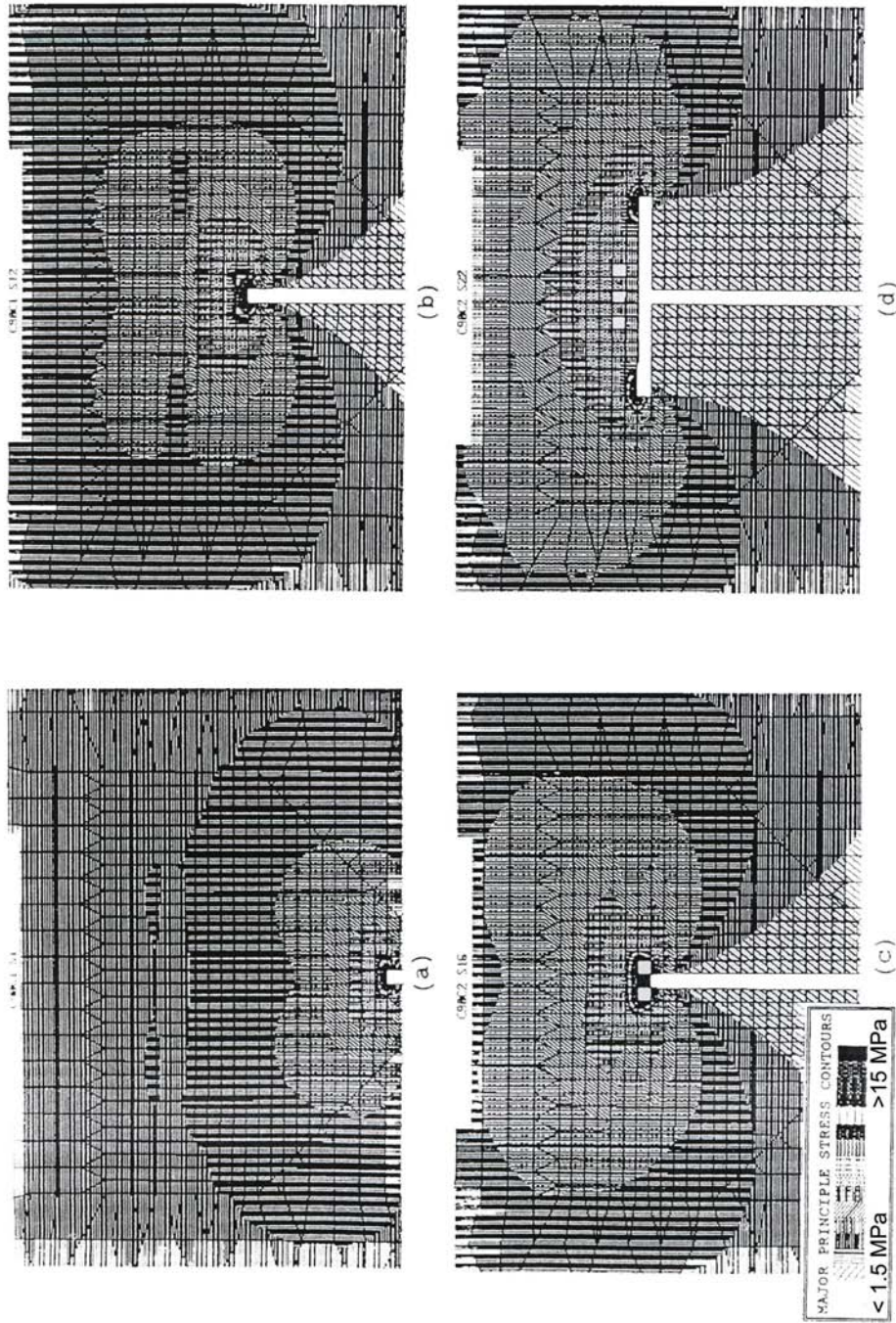


Fig. 5.8 (a): Fracture path for $\alpha_f < \alpha_m$, weak interface, 90° orientation (a) initial configuration (b) interface fracture in front of crack (c) fracture along interface (d) crack pinned by deflection along the interface

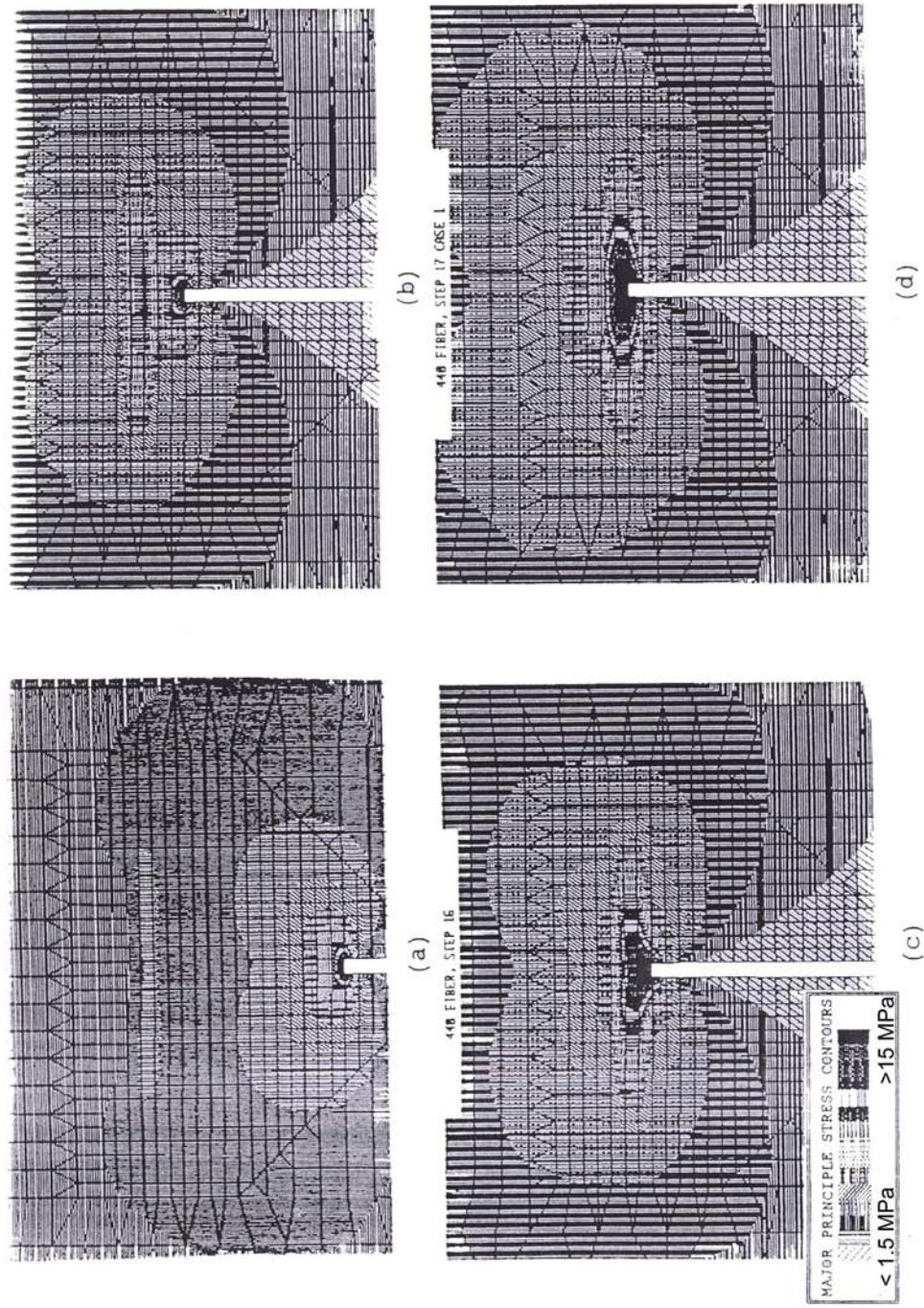


Fig. 5.8 (b): Fracture path for $\alpha_f = \alpha_m$, strong interface, 90° orientation (a) initial configuration (b), (c) self-similar propagation approaching fiber (d) crack pinning by the fiber

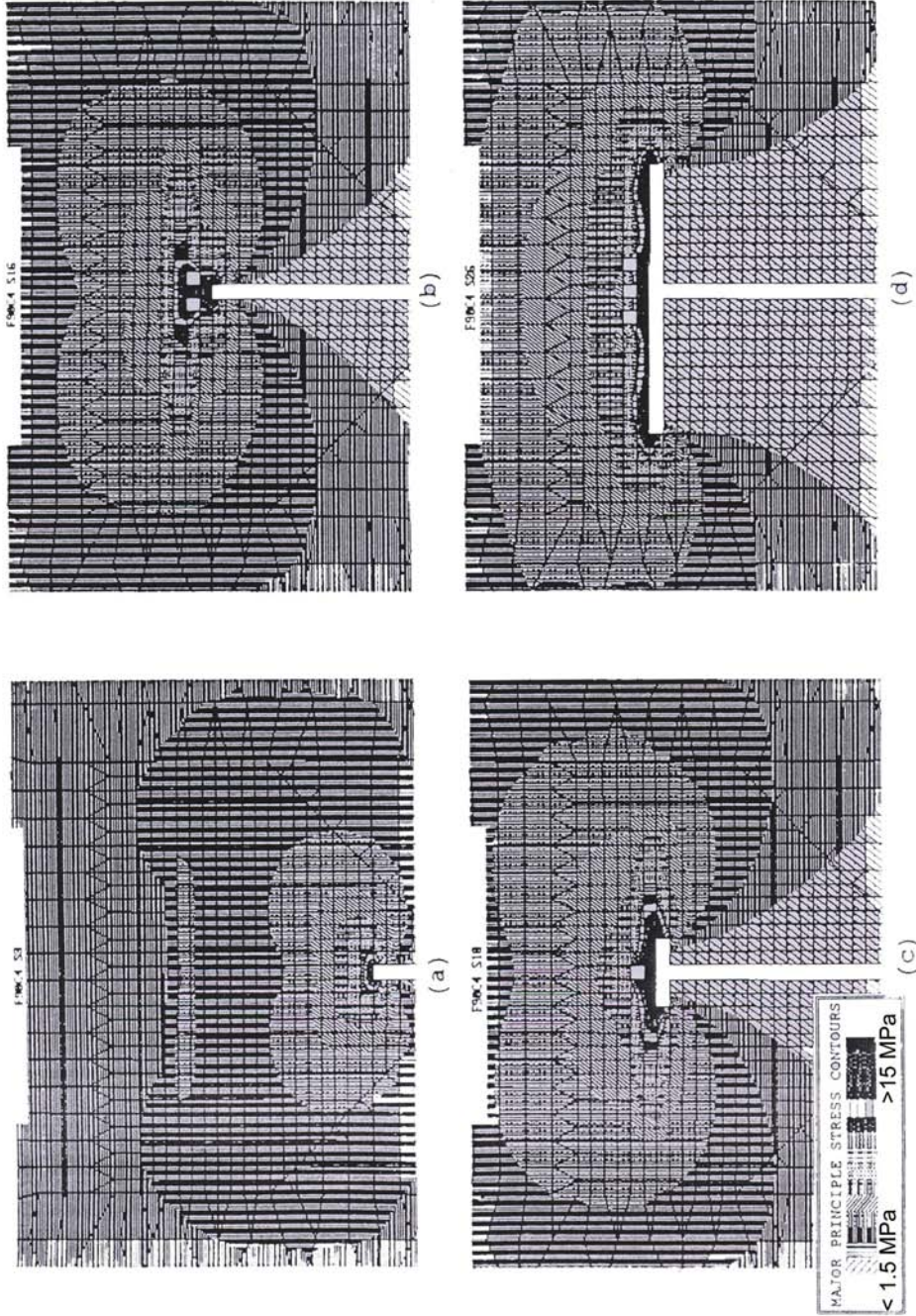


Fig. 5.8 (c): Fracture path for $\alpha_f = \alpha_m$, weak interface, 90° orientation (a) initial configuration (b) interface fracture in front of crack (c) crack pinned by deflection along the interface (d) fracture along interface

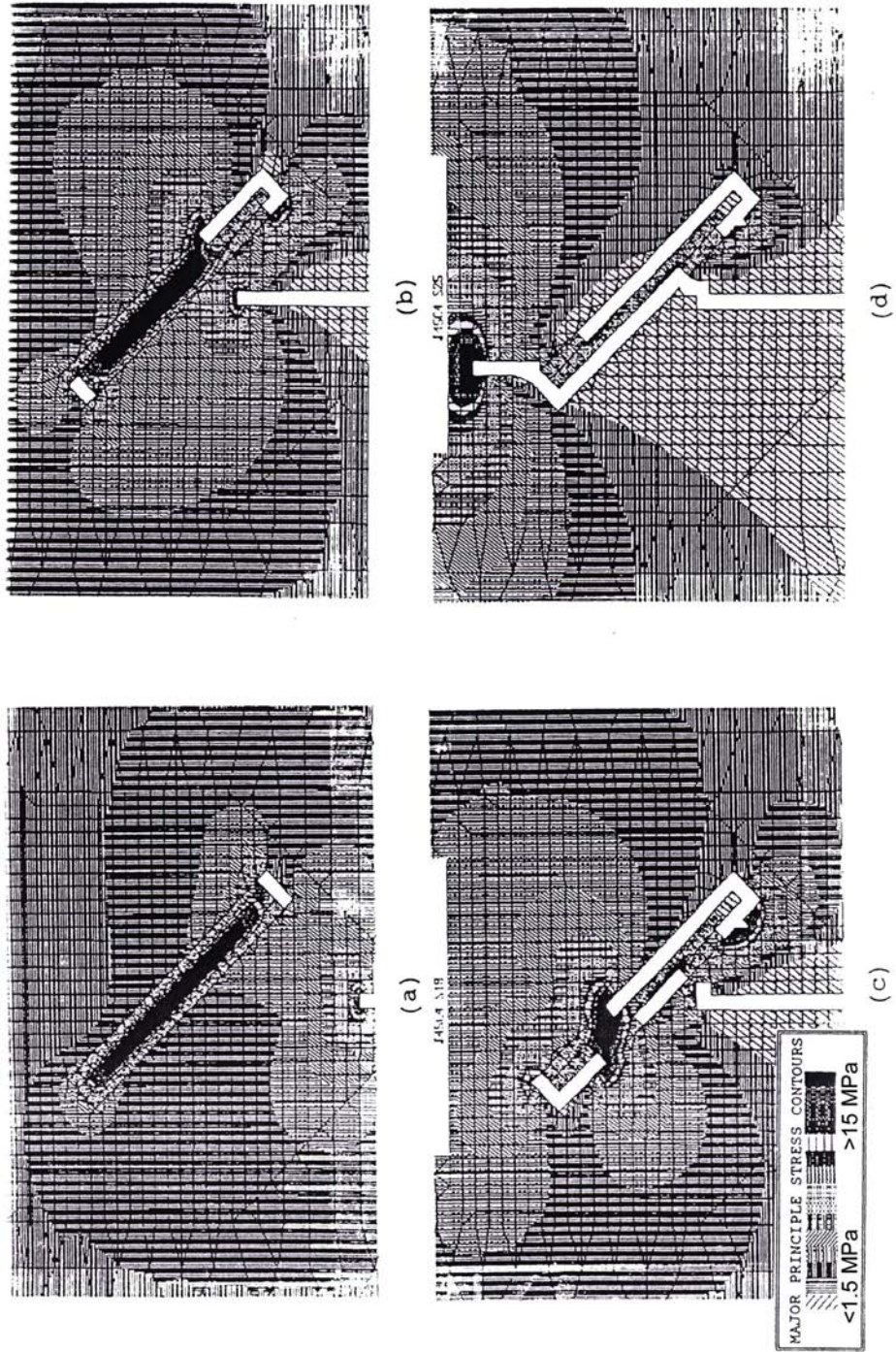


Fig.5.9.: Fracture path for $\alpha_f > \alpha_m$, weak interface, 45° orientation. (a) fiber end debond (b) end debond growth (c) interface fracture (d) link-up of primary and interface cracks

5.3 Fracture under different size reduction mills

5.3.1 Hammer mill (without screening)

Increased passes of material through the mill almost effected ϕ values according to the number of passes; values of ϕ decreased in the order of: pass five > pass three > pass one > pass two. Differences in shape factor were small, being 0.66 for pass five compared with 0.61 for pass two. However averaged over all the sizes, differences between ϕ values for pass five and some of the other passes were significantly different, even up to the 0.1% level.

Sieve size (μm)	Mean ϕ value
710	0.65 ^a
250	0.61 ^b
90	0.61 ^b

Table 5.4: Shapes of particles produced by unscreened hammer milling. Values are means of passes one to three and five and three replicates.

^{a,b} Means denoted by same letter are not significantly different at 5% level

Table 5.4 shows mean values of ϕ on the selected sieves. It can be seen that the value of ϕ was greatest for the 710 μm sieve and least for the 90 μm sieve and the difference in ϕ between 710 and 90 μm particles was 0.04. The decrease in the sphericity as the particle size decreased indicated the presence of more elongated particles at smaller sizes. Overall, ϕ values (particle shapes) were highly significantly ($p < 0.001$) dependent on particle size.

5.3.2 Hammer mill

The addition of screen to the hammer mill produced differences in particle shape as compared to unscreened hammer milling. Mean values of shape factor ϕ , increased as the number of passes through the mill increased. The magnitude of change in shape from pass five to pass one was 0.66-0.57 and significant differences in shape were only seen for particles from pass one compared to particles produced by other passes ($p < 0.001$). Table 5.5 shows shape differences between the three sizes where particles were present. Unlike the hammer milling without the screen, the value of ϕ fell as particle size decreased. Although all size fractions had significantly different particle shapes from each other at the 5% level, only the 90 μm particles were different in shape from other sizes at the 0.1% level. Considering unscreened hammer milling two differences can be observed – (i) consideration of effect of particle selection in the mill and (ii) possible occurrence of secondary breakage of fractured particles on the metal casing of the mill. These two differences are obviously great enough that shapes of the resulting particulate distribution are dissimilar to those generated from different mills.

Sieve size (μm)	Mean ϕ value
710	0.66 ^{a,a}
250	0.63 ^{b,a}
90	0.57 ^{c,b}

Table 5.5: Shapes of particles produced by screened hammer milling.

Values are means of passes one to three and five and three replicates.

^{a - c} Means denoted by same letters in first superscript are not significantly different at 5% level; in second superscript at 0.1% level.

5.3.3 Blender mill

The action of the blender mill is unlike the other two methods of impact size reduction selected in that the area of impacting surface on the particles is small, generating a less uniform distribution of stresses within the particle. It is therefore expected that the resulting particle shapes would be different from other two methods of size reduction (Rivas, 2001). As time of milling increased mean values of ϕ increased indicating more rounded particle shapes (Table 5.6). Differences between ϕ noted in Table 5.6 disappeared as the level of significance decreased, such that at the 0.1 % level, significant differences in particle shapes were only seen between 15 and 10 , 15 and 3 minutes millings.

Time of milling (minutes)	Mean ϕ value
15	0.64 ^a
10	0.59 ^b
5	0.59 ^b
3	0.57 ^c

Table 5.6: Changes in particle shape with time of blender milling.

Values are means three replicates.

^{a-c} Means denoted by same letters are not significantly different at the 5% level

The change in ϕ with particle size is shown in Table 5.7. The trend was similar to that seen for the hammer mill : particle shape was more elongated at smaller size. The magnitude of the change in ϕ with size was 0.14 for 710-90 μm (0.09 for the hammer mill). In case of the blender, when any given size was examined, mean ϕ values were higher for the hammer mill.

Sieve size (μm)	Mean ϕ value
710	0.63 ^a
250	0.56 ^b
90	0.49 ^c

Table 5.7: Shapes of particles produced by blender milling.

Values are means of three replicates and three milling times

^{a-c} Means denoted by same letters are not significantly different at 5% level or 0.1% levels

5.3.4 Cryogenic mill

Initially, the grinding effect in the impact zone/mill of the system was tested by (i) without using cryogen and (ii) using cryogen. In the former case, an incomplete size reduction was observed in terms of gumming or jamming of walls, non-uniform, irregular particle sizes and excessive heat generation. On the other hand grinding in the presence of cryogen the said problems were not observed. Also when it was attempted to circulate cryogen around the casing of the hammer mill, though effective size reduction was observed as compared to grinding without using cryogen, the mill was to be intermittently stopped due to excessive heat generation in the grinding zone.

Table 5.8 shows mean values of ϕ on the selected sieves. As it can be seen from the table, the values of ϕ were greatest as compared to hammer mill and blender milling, indicating uniform particle size reduction due to embrittled lattice effected by cryogen and non occurrence of secondary breakage of fractured particles in the metal casing of the mill.

Sieve size (μm)	Mean ϕ value
710	0.74 ^a
250	0.66 ^b
90	0.61 ^c

Table 5.8: Shapes of particles produced by cryogenic milling.

Values are means of passes two and three replicates.

^{a-c} Means denoted by same letters are not significantly different at 5% level

5.3.5 Size and shape characterization of cryo-ground and conventionally (without using cryogen) ground turmeric

Fig. 5.10 shows cumulative undersize weight fraction of the conventional and cryogenic ground turmeric powder. The curves are typical of the particle size distribution patterns reported in literature for different materials. As expected the cryo-ground materials are much finer. Volume mean diameter (or weight mean diameter) of cryo-ground turmeric is 50 μm smaller than conventionally ground turmeric. The volume mean diameter of the conventionally ground turmeric powder was found to be 199.2 μm (std.dev. :83.05) and for cryoground turmeric it was 149.2 μm (std.dev. :53.56).

Eighty percent of the particles by weight are less than 257 μm in the case of conventional-ground turmeric and 198 μm in the case of cryo-ground turmeric. Maximum particle size is 472 μm and 296 μm for conventional-ground and cryo-ground turmeric respectively.

Rossen-Rammler Bennet (RRB) plots of the equation for both grinding methods are shown in Fig. 5.11. The RRB equations describe the particle size distribution of turmeric powder obtained by both grinding methods well. Coefficient of determination (R^2) for the regression is 0.975 and 0.990 for conventional ground turmeric whereas the n' for cryo-ground turmeric is 3.01

indicating more uniformity of particle size distribution in the case of cryo-ground turmeric. Particle size distribution plots as per the Gaudin-Schumann and log-normal functions are in Figs 5.12 and 5.13 respectively. R^2 for the above functions for both cases of grinding of turmeric are also shown in the figures. From comparison of R^2 values of the fitted equations, one can conclude that RRB function fits the size distribution data better than other functions. The log-normal function for the conventional ground turmeric powder is $dF(x)=0.0057 \exp(-3.15 \log_e^2(x/161.3)) dx$. The log-normal function for the cryogenic ground turmeric powder is: $dF(x)=0.0081 \exp(-4.31 \log_e^2(x/133.2)) dx$. σ_g values (in the log-normal size distribution function) are 1.49 and 1.41 for the conventional and cryogenic grinding turmeric powder respectively.

Table 5.9 shows the results of the shape analysis for turmeric ground by both methods. The values of the various shape parameters for the conventional ground turmeric are much smaller than cryo-ground turmeric. The range for the values of each shape parameters is much less for the particles of cryo-ground process than the conventional grinding process. The mean shape factor of the conventional ground turmeric is 0.64 and the shape factors of cryo-ground turmeric particles are 0.74. Fig. 5.14 shows cumulative number distribution pattern of shape factor of particles of conventional and cryogenic grinding process respectively. The figure shows that there are about 10% particles highly rectangular in shape (shape factor less than 0.5) in conventional ground particles whereas only about 5% particles are having shape factor less than 0.5 in the case of cryo-ground particles.

	Conventional grinding				Cryo grinding			
	Mean	Standard deviation	Minimum	Maximum	Mean	Standard deviation	Minimum	Maximum
Average Feret's size, μm	88.20	216.00	4.80	1303.00	8.56	14.80	0.87	440.60
Average Martin's size, μm	37.81	117.12	2.21	820.9	1.58	3.17	0.41	268.7
Aspect ratio	625.00	1841.00	14.34	13877.00	46.70	139.00	3.14	4460.00
Perimeter, μm	0.64	0.21	0.04	0.97	0.74	0.12	0.05	0.95
Shape factor or sphericity	295.00	901.00	4.43	6832.00	21.50	68.40	0.87	2192.00
Specific length, μm	24.70	25.60	2.21	218.60	5.26	4.36	0.70	38.01
Specific width, μm								

Table 5.9 : Some key parameters of the shape analysis of turmeric powder

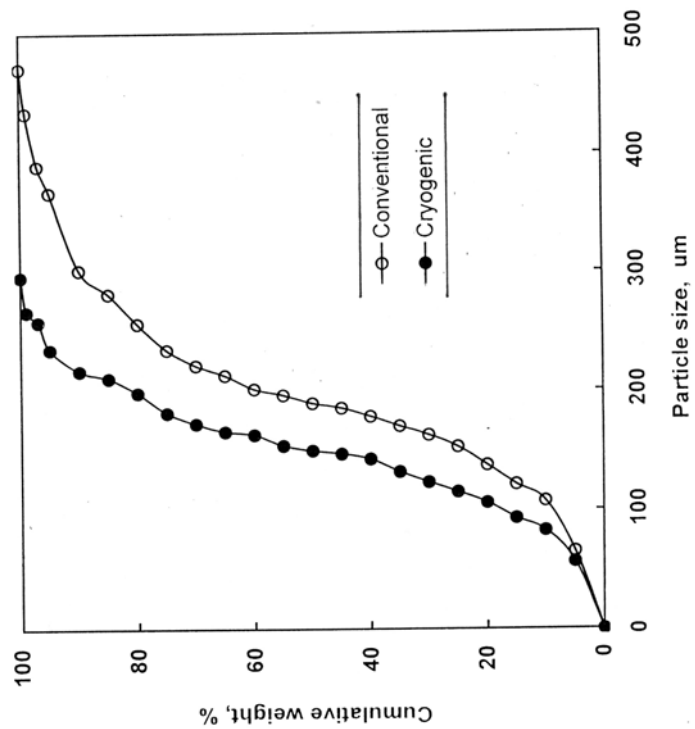


Fig. 5.10: Cumulative under size weight fraction curves for conventional and cryogrinding methods

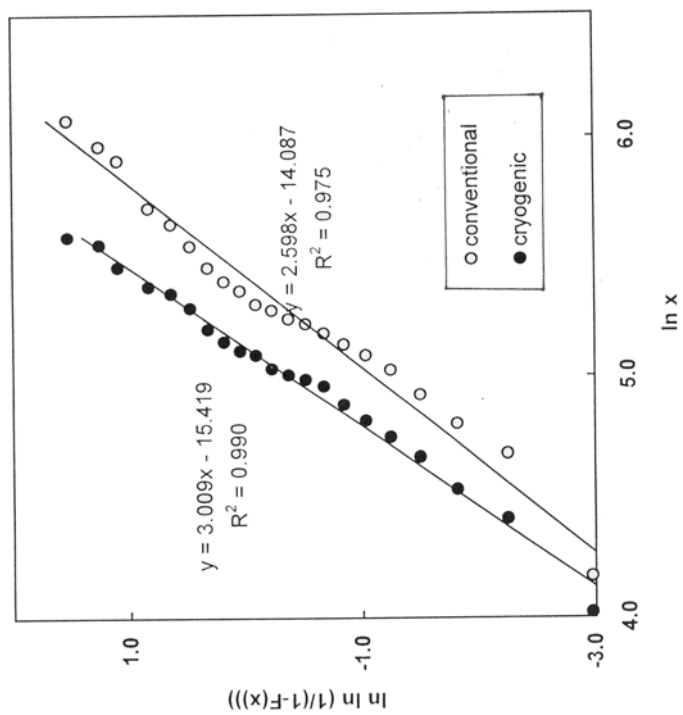


Fig.5.11: Rosin-Rammler-Bennet plots for conventional and cryo-grinding methods

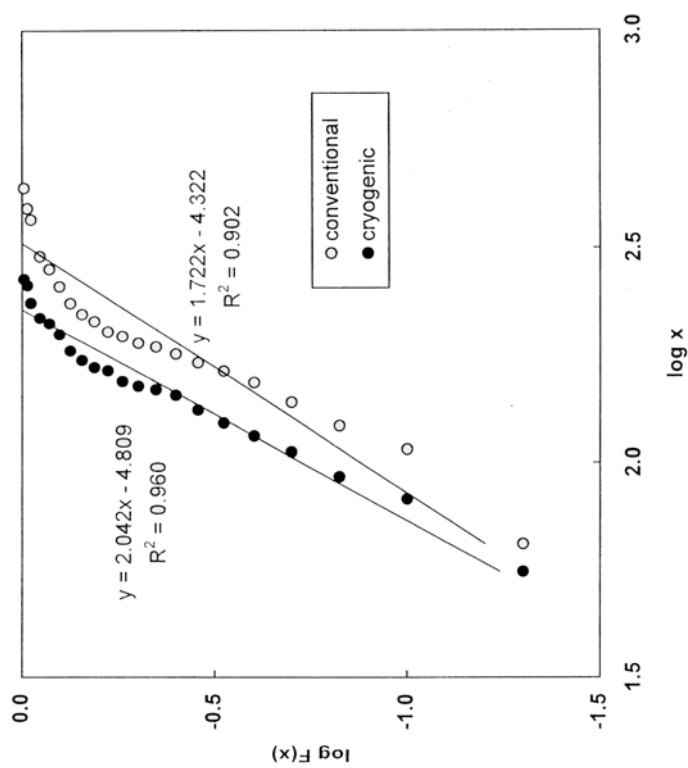


Fig.5.12: Gaudin-Schumann plots for conventional and cryogenic grinding methods

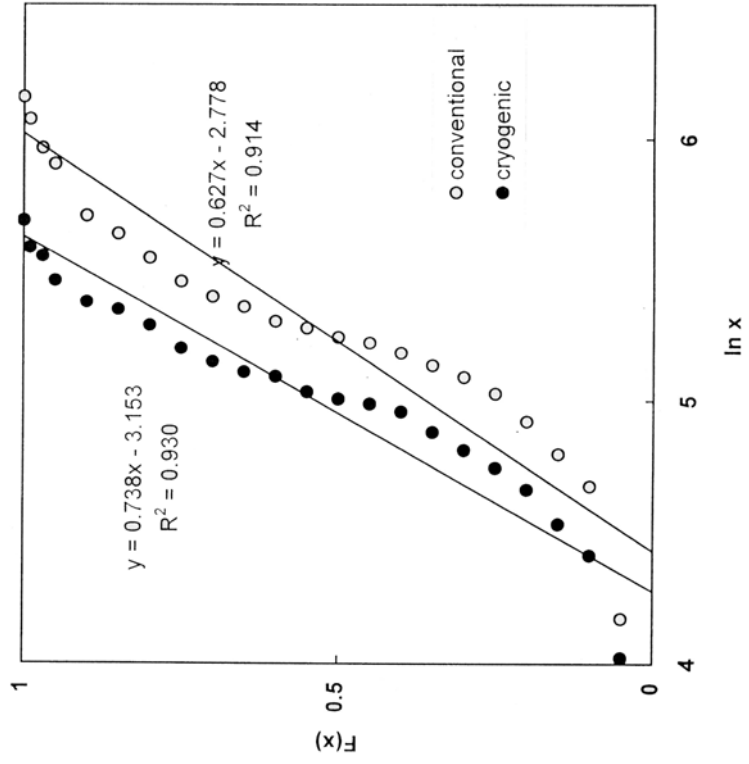


Fig. 5.13: Log-normal function plots for conventional and cryogenic methods

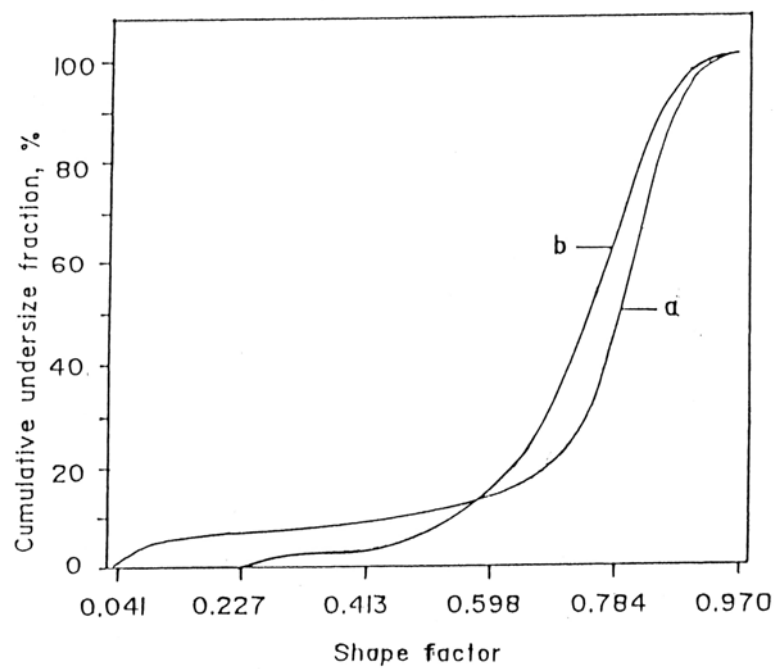


Fig.5.14: Cumulative number distribution for the shape factor for (a) conventionally ground turmeric (b) cryo-ground turmeric

5.4 Thermal effects prediction of fracture particulates

The calculated ΔT results are shown in the Tables 5.10 and 5.11. The graphical representation of particle size distribution of turmeric under ambient and cryogenic conditions impacted under $3.03 \times 10^6 \text{ J/m}^3$ is shown in Fig.5.15. The heat capacities, (C_p) of turmeric under ambient and cryogenic conditions (-8°C) respectively were, 1.641 and 1.890 kJ/kg $^\circ\text{C}$ (Kachuru and Alam, 1994). The mean values (after three replications) of two parameters D_g and σ_g , of log-normal probability distribution function as well as their (%) range were found to be: 480 μm (+31%, -21%); 1.93 (+35%, -29%) under ambient conditions and 400 μm (+25%, -27%); 2 (+25%, -31%) under cryogenic conditions (-8°C). It can be seen from the tables that the particle size ranges from 0-3600 μm with an average weight mean diameter of 567 μm for ambient and 484 μm for cryogenic conditions. The various parameters estimated under the said conditions such as surface-volume ratio, energy density and the combined strength parameters respectively were: $3.55 \times 10^3 - 1.07 \times 10^6 \text{ (m}^{-1}\text{)}$; $2.88 \times 10^5 - 8.63 \times 10^7 \text{ (J/m}^3\text{)}$ and $81.05 \text{ (J/m}^2\text{)}$ for ambient conditions and under cryogenic conditions, the values were: $3.80 \times 10^3 - 1.14 \times 10^6 \text{ (m}^{-1}\text{)}$; $2.65 \times 10^5 - 7.95 \times 10^7 \text{ (J/m}^3\text{)}$ and $69.76 \text{ (J/m}^2\text{)}$. The temperature rise shown in the tables is the maximum that could occur for a particle of the given diameter. As shown in the tables a temperature rise of up to 40.5°C , under ambient conditions and 26.9°C under cryogenic conditions, could occur for particles 12μ or lower. A plot of the maximum possible temperature as a function of a particle size is given in Fig. 5.16.

5.4.1 Temperature distribution simulation

The finite element grid of a quarter section of turmeric is shown in Fig. 5.17. The quarter section is shown since it is assumed the symmetry of turmeric. The temperature at different radial locations as predicted by FEM and the analytical solution were compared. The FEM calculated and analytical solution were within 1.5°C or 2.90 % relative difference.

The typical FEM plots of temperature distribution in turmeric samples for the different boundary conditions considered are given in Fig. 5.18 to 5.21. The FEM calculated temperature distributions for sizes 9.1×10^{-7} , 26.56×10^{-7} , and $46.33 \times 10^{-7} \text{ m}^3$ under the boundary conditions, (top face and bottom face of the product, 25°C and lateral surface, -8°C) are given in Fig. 5.22 to 5.24. Simulation results are illustrated as an example in Fig. 5.25 to 5.27, for the size $46.33 \times 10^{-7} \text{ m}^3$, length to diameter ratios, 0.25 to 1.00 under the boundary conditions, temperature at the top face, 25°C and at the bottom and lateral surface of the product, 0°C . Observations were similar for other boundary conditions and samples.

It can be seen from Fig. 5.18 and 5.20 that temperature distribution is symmetrical on either side of the sample, when the temperature at the top and bottom surface is at 25°C and at the lateral surface at -8°C , whereas it is non-symmetrical (Fig. 5.19 and Fig.5.21) when the temperature is at 25°C at the top face and 0°C at the bottom and lateral surface of the product respectively, even though the distribution pattern in both the cases is similar. Also in all the cases, it can be seen that the temperature gradient dies down or becomes negligible after some distance in the sample.

Of the three volumes considered, the pattern of temperature distribution within the product is similar and not symmetrical. The temperature gradient becomes negligible after some distance in the sample. The spread in temperature proportionately increased with increase in volume, with no change in pattern of distribution. It can be seen that with length to diameter ratios varying from 0.25 to 1.00, the temperature gradient or change appears to be predominant till length to diameter ratio, equal to 0.5. Beyond this, the temperature variation is negligible or remain constant, including no change in pattern of temperature distribution. Similar behaviour was observed for change in boundary conditions and other samples.

Particle diameter, μm	Cumulative volume fraction $V(D)/V_n$	Surface volume ratio, ^a m^{-1}	Energy density, ^b J/m^3	Temperature rise, ^c $^{\circ}\text{C}$
12	0.04	1.065E+06	8.629E+07	40.46
24	3.43	5.323E+05	4.315E+07	20.23
36	4.33	3.549E+05	2.876E+07	13.49
48	5.59	2.661E+05	2.157E+07	10.11
60	7.18	2.129E+05	1.726E+07	8.09
72	9.78	1.774E+05	1.438E+07	6.74
84	10.93	1.521E+05	1.233E+07	5.78
96	11.84	1.331E+05	1.079E+07	5.06
108	12.35	1.183E+05	9.588E+06	4.50
120	12.56	1.065E+05	8.629E+06	4.05
360	35.83	3.549E+04	2.876E+06	1.35
720	77.81	1.774E+04	1.438E+06	0.67
960	86	1.331E+04	1.079E+06	0.51
1200	93.36	1.065E+04	8.629E+05	0.40
1680	94.96	7.604E+03	6.164E+05	0.29
2160	96.47	5.914E+03	4.794E+05	0.22
2400	97.85	5.323E+03	4.315E+05	0.20
2880	99.02	4.436E+03	3.595E+05	0.17
3120	99.62	4.094E+03	3.319E+05	0.16
3600	100	3.549E+03	2.876E+05	0.13

$D_g = 480 \mu\text{m}$; $\sigma_g = 1.93 (D_{84}/D_{50})$; Density = $1300 \text{ kg}/\text{m}^3$; $W_o = 102.9 \text{ J}$;
 $C_v = 2132884 \text{ J}/\text{m}^3\text{C}$ ($C_p \times \rho$); $(\gamma_f / \varepsilon) = W_o/S_n = 81.06 \text{ J}/\text{m}^2$; $W_o/V_n = 2.68 \text{ E} +06 \text{ J}/\text{m}^3$
^a calculated from Eq. (2.41); ^b calculated from Eq. (2.39); ^c calculated from Eq. (2.40)

Table 5.10: Calculated properties of fracture particulate for turmeric impacted at $3.03 \times 10^6 \text{ J}/\text{m}^3$ under ambient conditions

Particle diameter, μm	Cumulative volume fraction $V(D)/V_n$	Surface volume ratio, ^a m^{-1}	Energy density, ^b J/m^3	Temperature rise, ^c $^{\circ}\text{C}$
12	0.09	1.140E+06	7.954E+07	26.93
24	5.36	5.702E+05	3.977E+07	13.47
36	6.53	3.801E+05	2.651E+07	8.98
48	7.94	2.851E+05	1.989E+07	6.73
60	10.25	2.281E+05	1.591E+07	5.39
72	13.06	1.901E+05	1.326E+07	4.49
84	14.78	1.629E+05	1.136E+07	3.85
96	17.3	1.425E+05	9.943E+06	3.37
108	17.31	1.267E+05	8.838E+06	2.99
120	18.41	1.140E+05	7.954E+06	2.69
360	46.32	3.801E+04	2.651E+06	0.90
720	81.9	1.901E+04	1.326E+06	0.45
960	91.06	1.425E+04	9.943E+05	0.34
1200	95.7	1.140E+04	7.954E+05	0.27
1680	96.53	8.145E+03	5.682E+05	0.19
2160	97.82	6.335E+03	4.419E+05	0.15
2400	98.43	5.702E+03	3.977E+05	0.13
2880	99.53	4.751E+03	3.314E+05	0.11
3120	99.94	4.386E+03	3.059E+05	0.10
3600	100	3.801E+03	2.651E+05	0.09

$D_g = 400 \mu\text{m}$; $\sigma_g = 2 (D_{84}/D_{50})$; Density = $1800 \text{ kg}/\text{m}^3$; $W_o = 102.9 \text{ J}$;
 $C_v = 2953224 \text{ J}/\text{m}^3\text{C}$ ($C_p \times \rho$); $(\gamma_f / \varepsilon) = W_o/S_n = 69.76 \text{ J}/\text{m}^2$; $W_o/V_n = 3.03 \text{ E} +06 \text{ J}/\text{m}^3$
^a calculated from Eq. (2.41); ^b calculated from Eq. (2.39); ^c calculated from Eq. (2.40)

Table 5.11: Calculated properties of fracture particulate for turmeric impacted at $3.03 \times 10^6 \text{ J}/\text{m}^3$ under cryogenic conditions (-8°C)

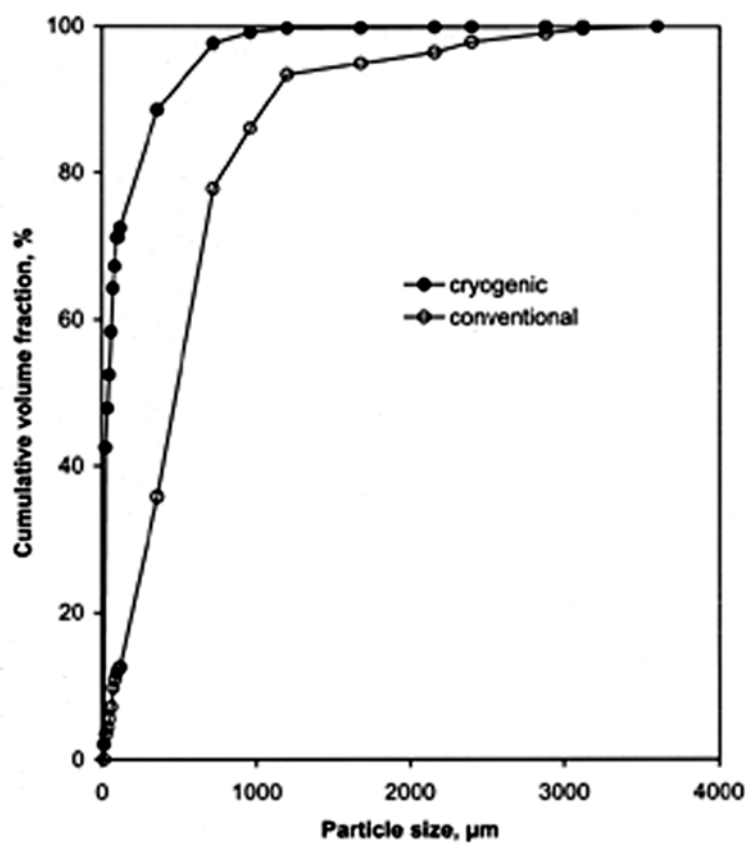


Fig. 5.15: Particle size distribution of turmeric under ambient and for cryo-treated samples impacted at $3.03 \times 10^6 \text{ J/m}^3$

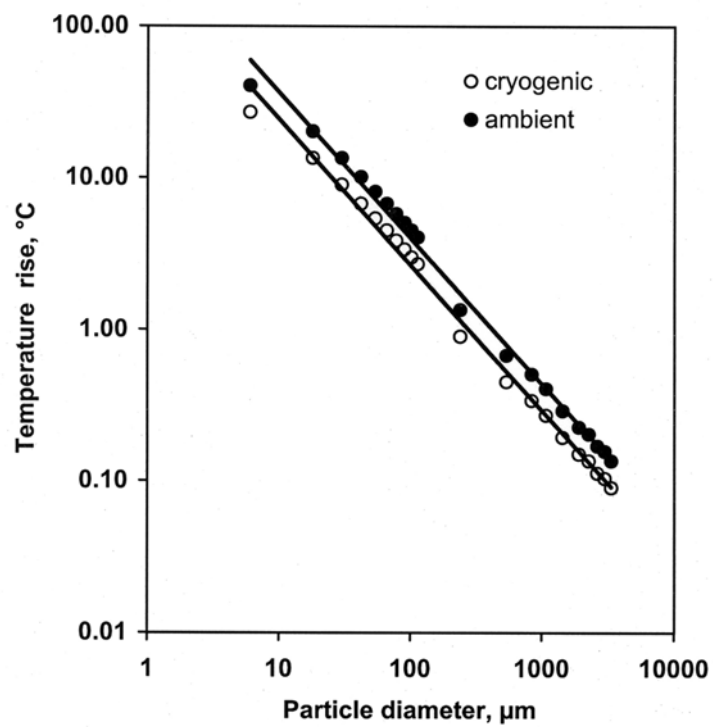


Fig. 5.16: Calculated temperature rise as a function of the size of turmeric particles under fracture for ambient and for cryo-treated samples (based on Tables 5.10 and 5.11)

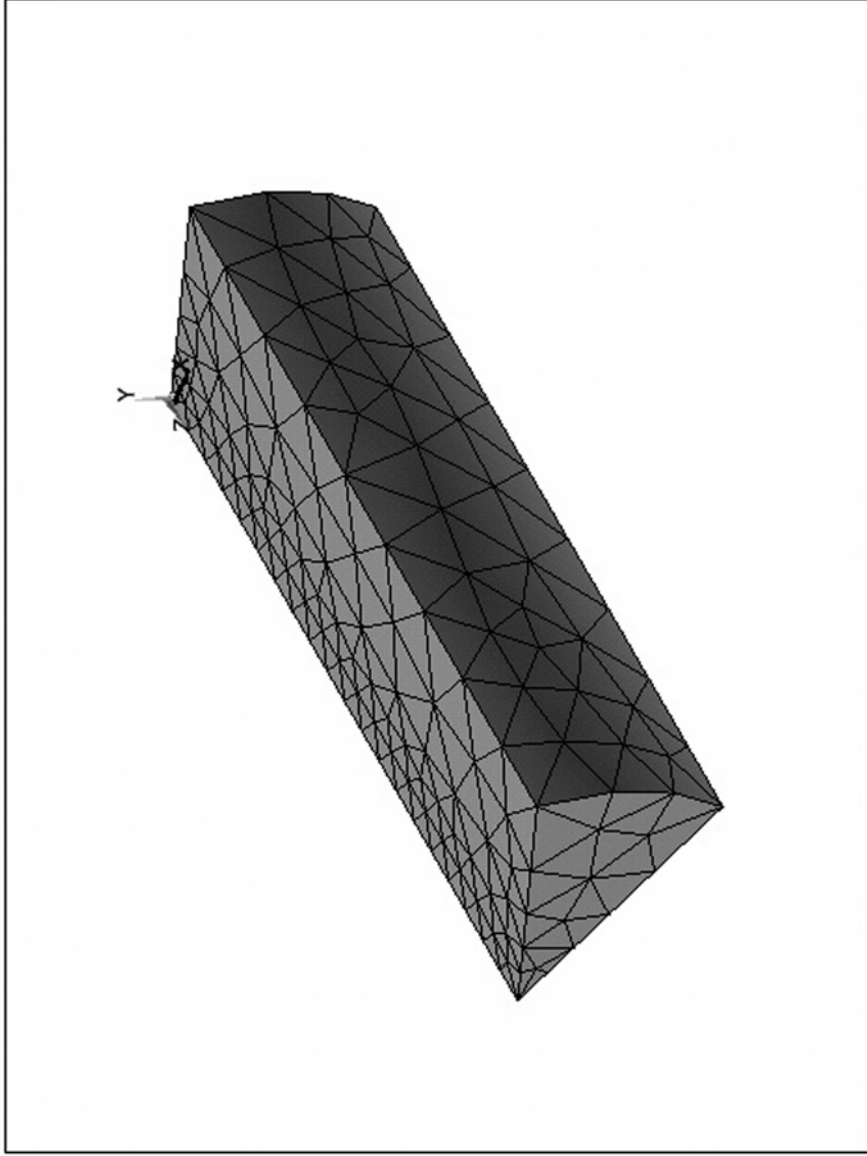


Fig. 5.17: Finite element mesh for turmeric (1/4 cross section, 1367 nodes and 665 elements)

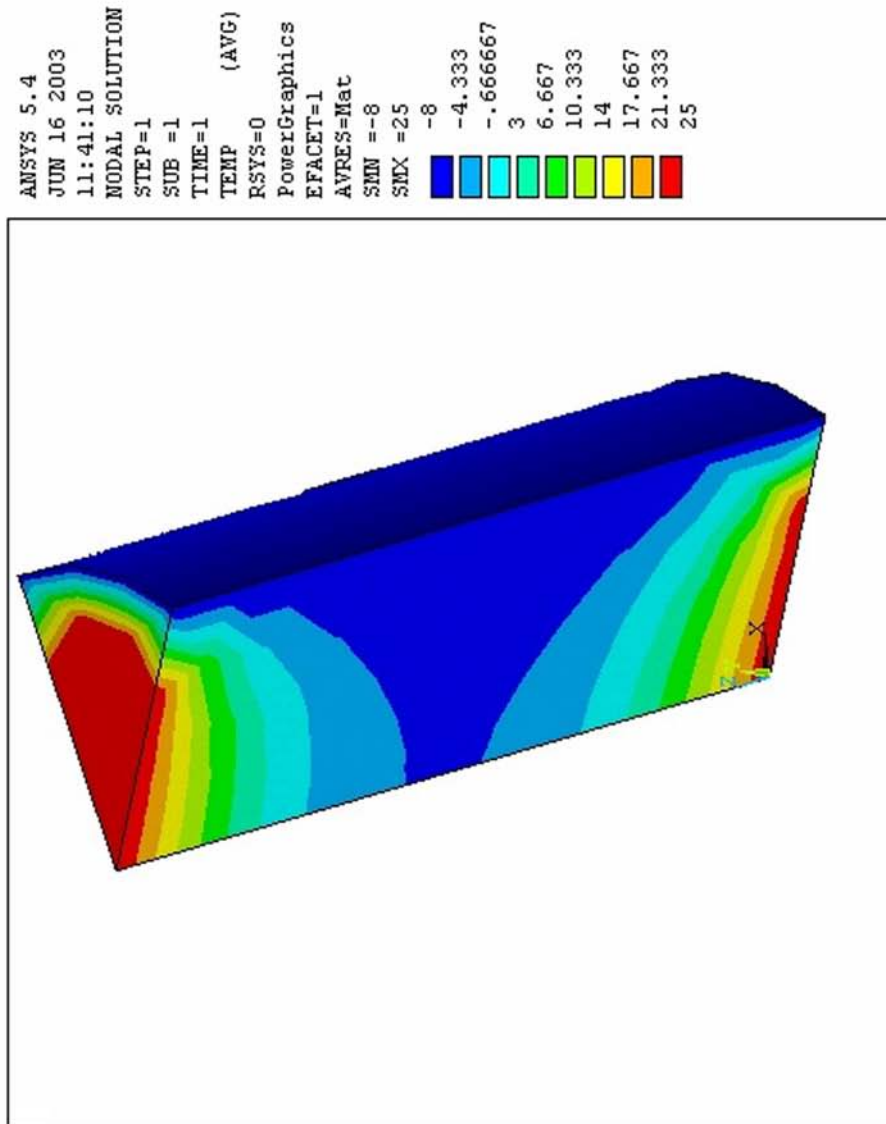


Fig. 5.18: Temperature distribution for turmeric (1/4 cross section) at the boundary conditions of top, 25°C, bottom, 25°C and lateral surface - 8°C (thermal conductivity - 0.458 W/m K; density - 1300 kg/m³; specific heat - 1.641 kJ/kg K)

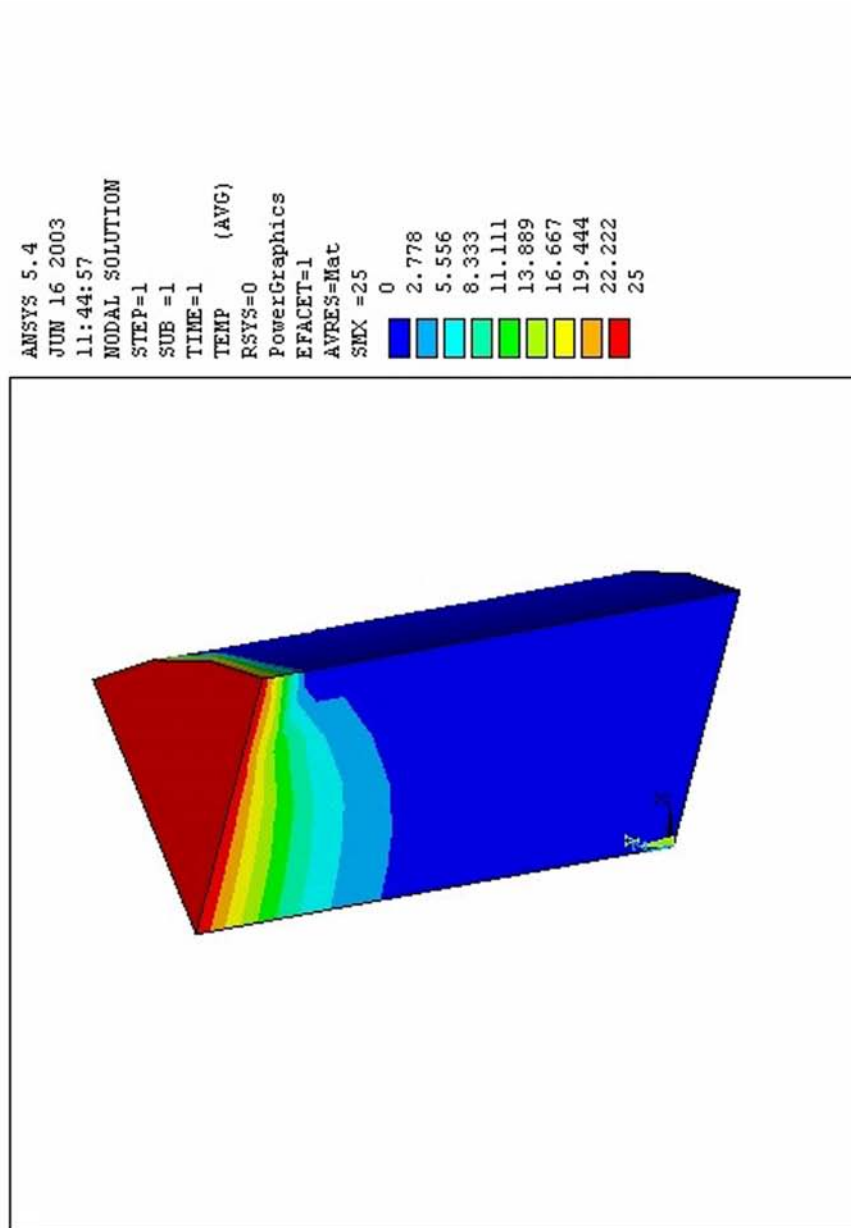


Fig. 5.19: Temperature distributions for turmeric (1/4 cross section) at the boundary conditions of top, 25°C, bottom, 0°C and lateral surface, 0°C (thermal conductivity - 0.458 W/m K; density - 1300 kg/m³; specific heat - 1.641 kJ/kg K)

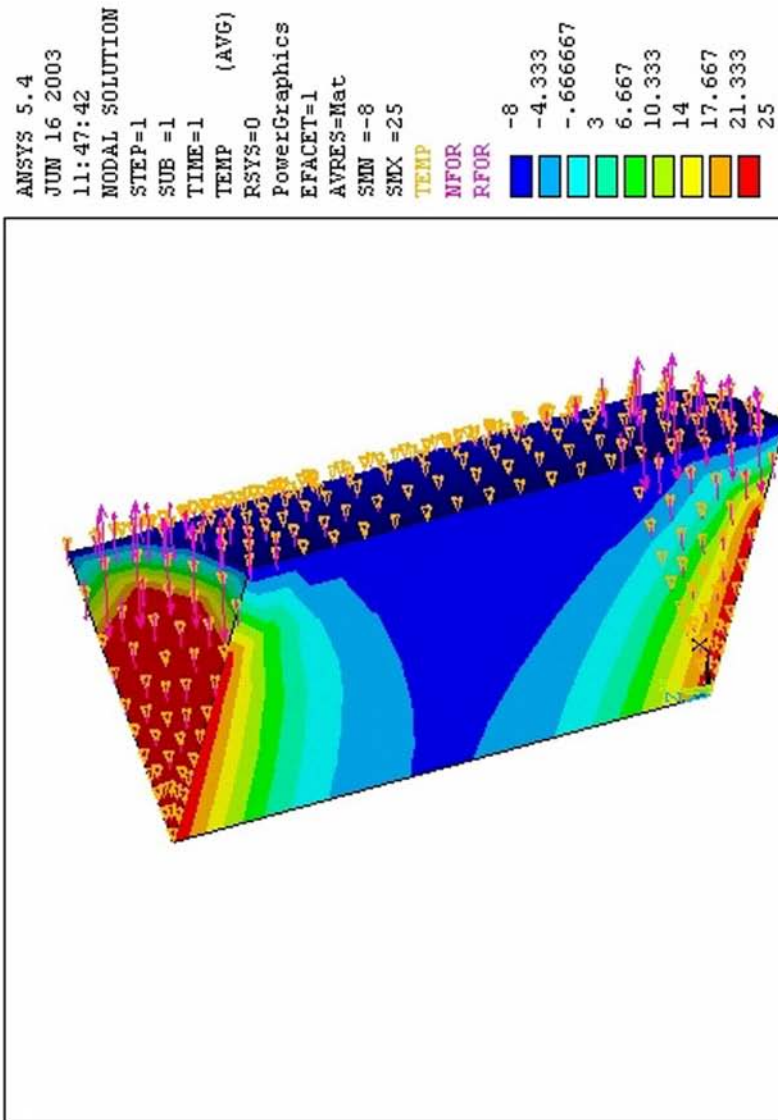


Fig. 5.20: Temperature distributions for cryo-treated (- 8°C) turmeric (1/4 cross section) at the boundary conditions of top, 25°C, bottom, 25°C and lateral surface - 8°C (thermal conductivity - 0.326 W/m K; density - 1800 kg/m³; specific heat - 1.890 kJ/kg K)

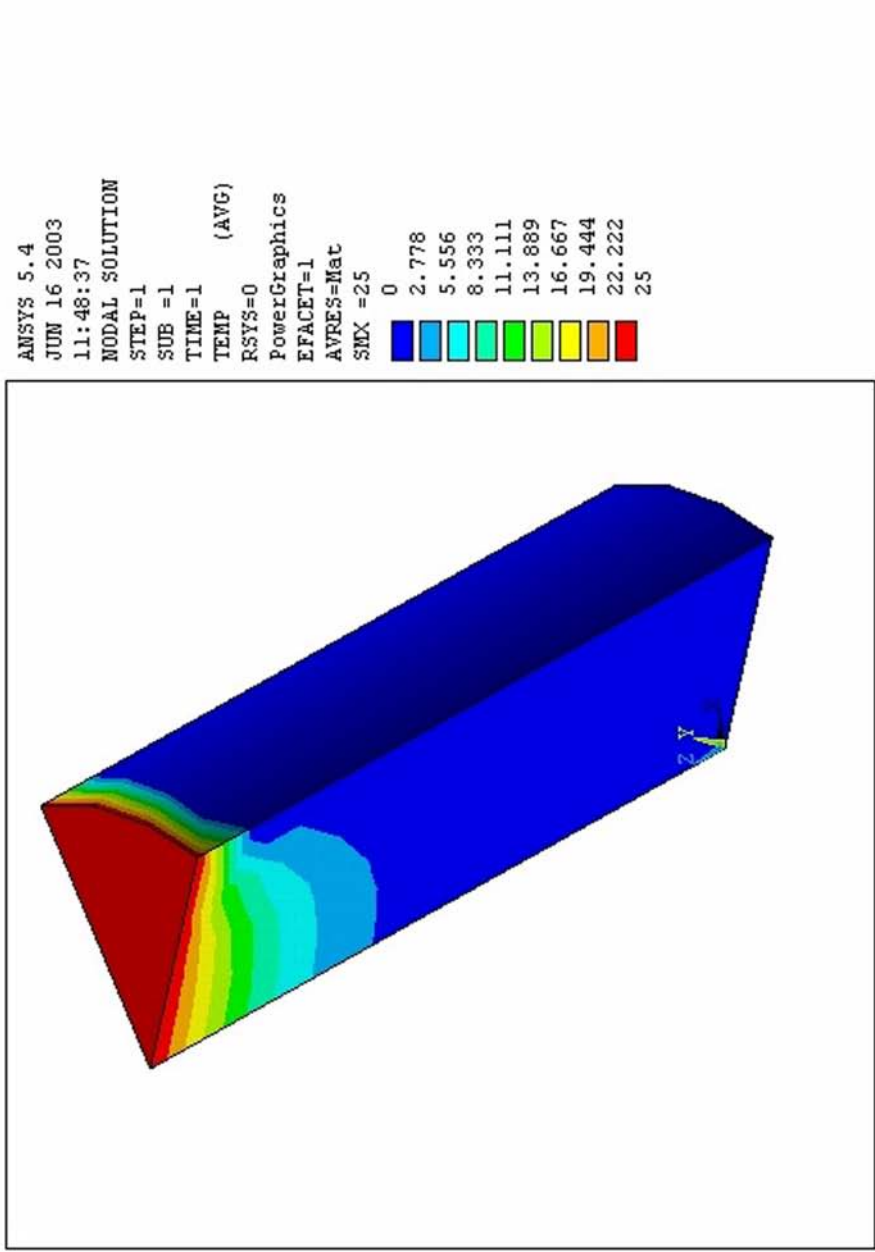


Fig. 5.21: Temperature distributions for cryo-treated (-8°C) turmeric (1/4 cross section) at the boundary conditions of top, 25°C, bottom, 0°C and lateral surface 0°C (thermal conductivity - 0.326 W/m K; density - 1800 kg/m³; specific heat - 1.890 kJ/kg K)

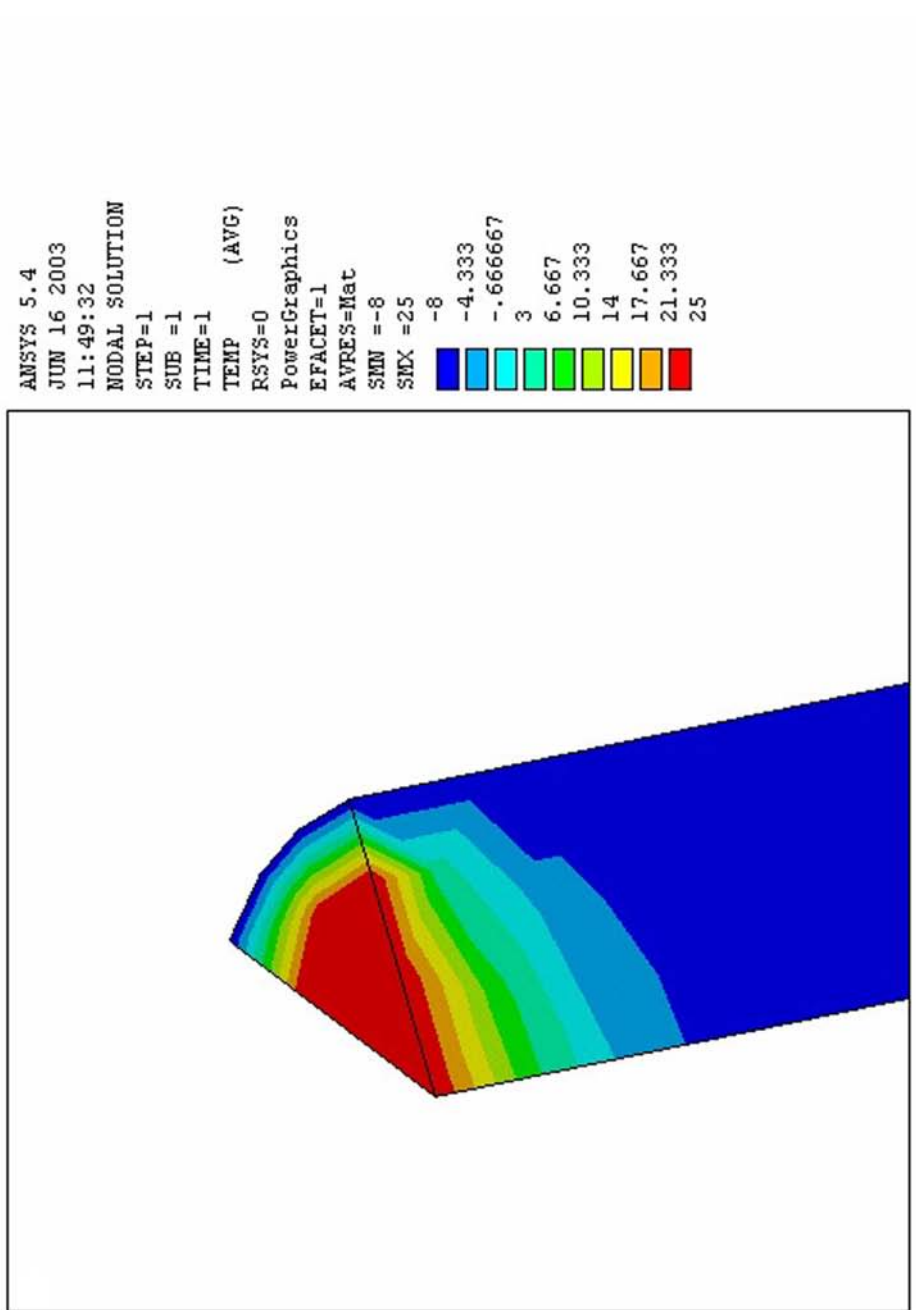


Fig. 5.22: Typical temperature profile in turmeric (volume, $9.1 \times 10^{-7} \text{ m}^3$; length, $28.23 \times 10^{-3} \text{ m}$; diameter $6.41 \times 10^{-3} \text{ m}$)

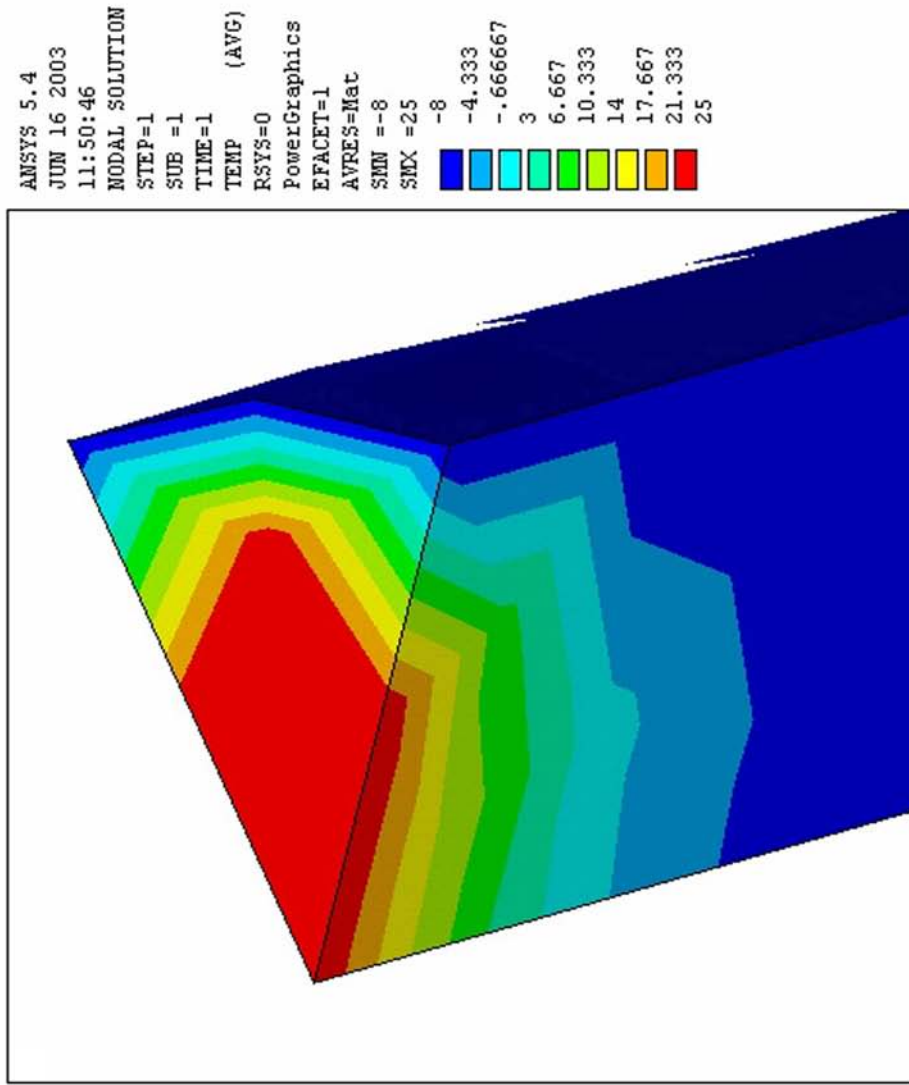


Fig. 5.23: Typical temperature profile in turmeric (volume, $26.56 \times 10^{-7} \text{ m}^3$; length, $42.67 \times 10^{-3} \text{ m}$; diameter $8.92 \times 10^{-3} \text{ m}$)

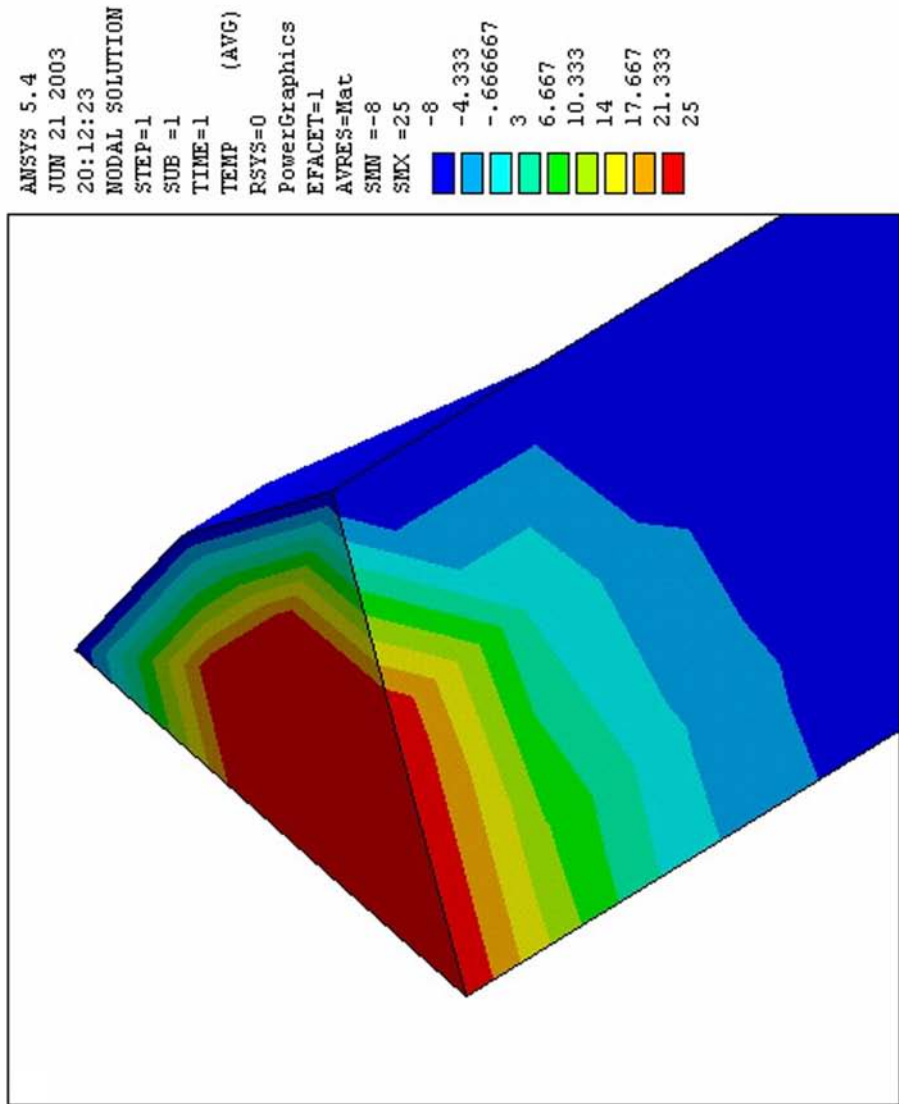


Fig. 5.24: Typical temperature profile in turmeric (volume, $46.33 \times 10^{-7} \text{ m}^3$; length, $52.5 \times 10 \text{ m}$; diameter $10.6 \times 10^{-3} \text{ m}$)

```

ANSYS 5.4
JUN 21 2003
21:53:58
NODAL SOLUTION
STEP=1
SUB =1
TIME=1
TEMP      (AVG)
RSYS=0
PowerGraphics
EFACET=1
AVRES=Mat
SMX =25
0
2.778
5.556
8.333
11.111
13.889
16.667
19.444
22.222
25

```

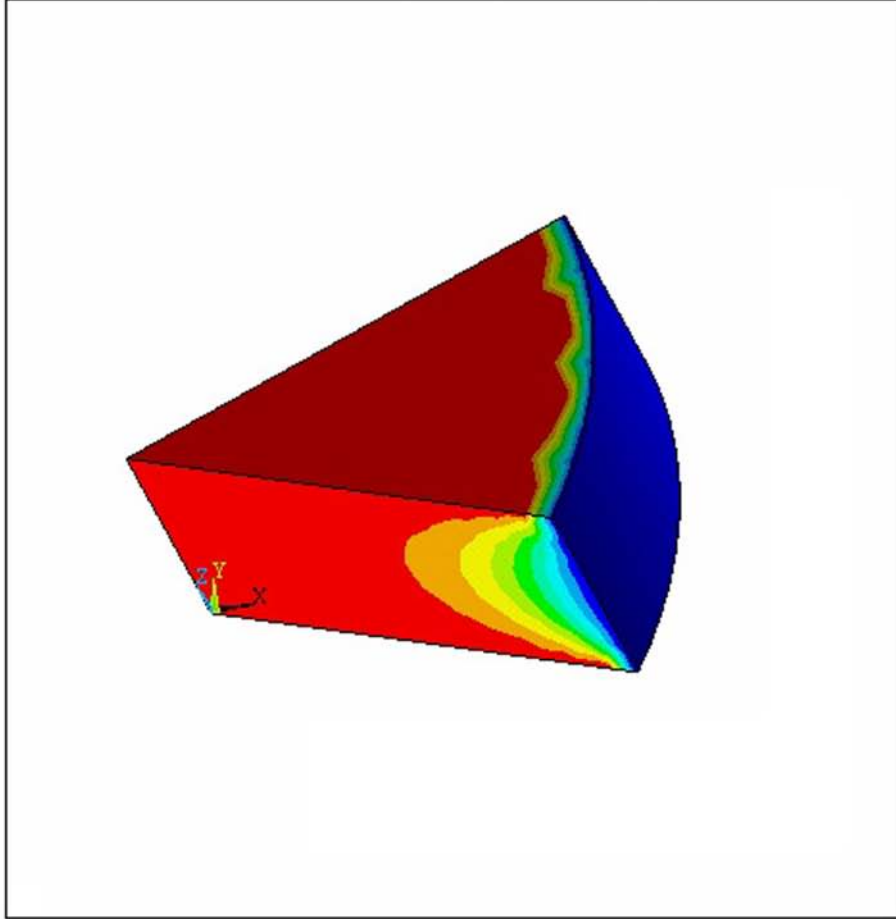


Fig. 5.25: Simulated temperature distribution in turmeric at $L/D = 0.25$ (volume, $46.33 \times 10^{-7} \text{ m}^3$)

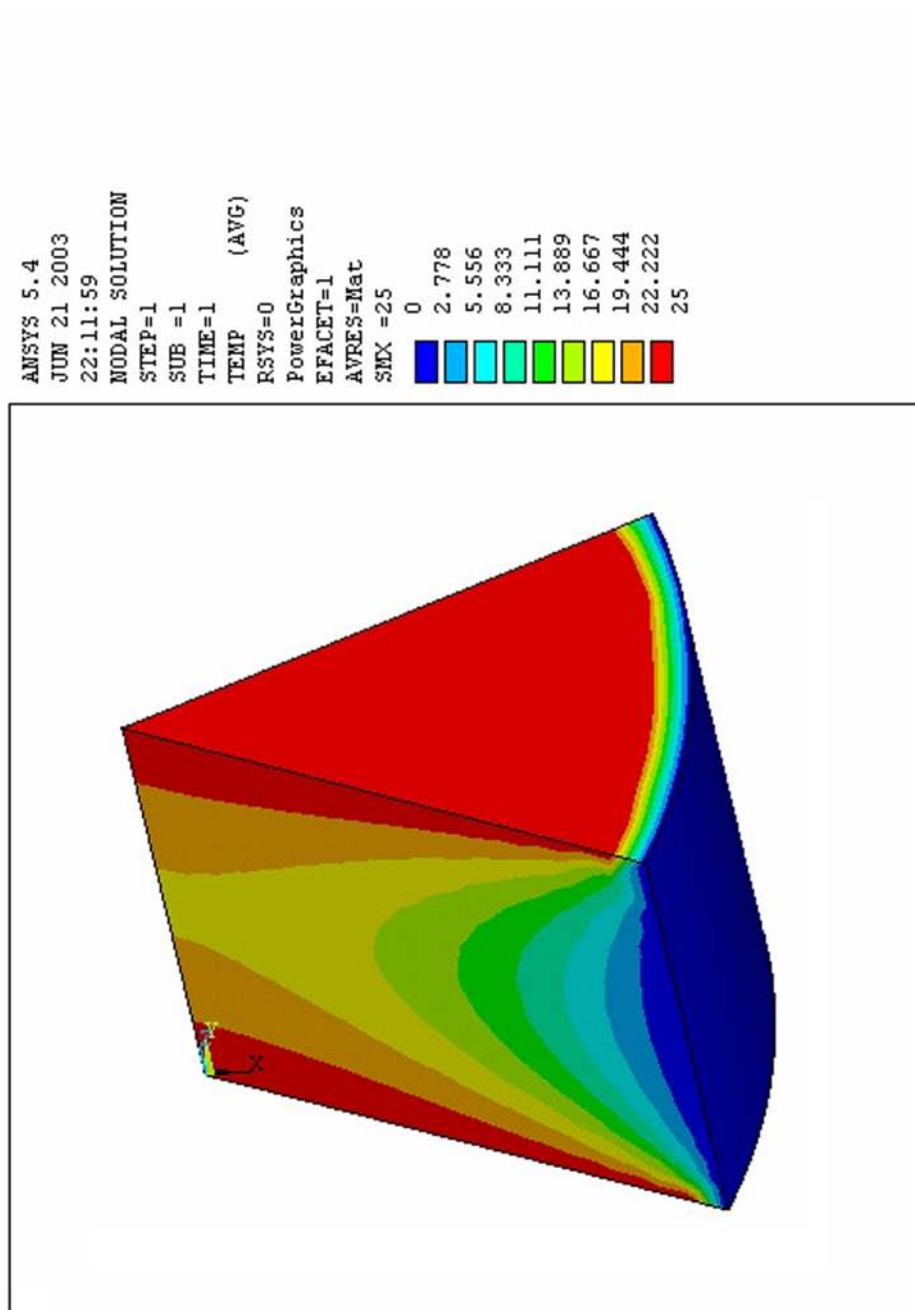


Fig. 5.26: Simulated temperature distribution in turmeric at $L/D = 0.50$ (volume, $46.33 \times 10^{-7} \text{ m}^3$)

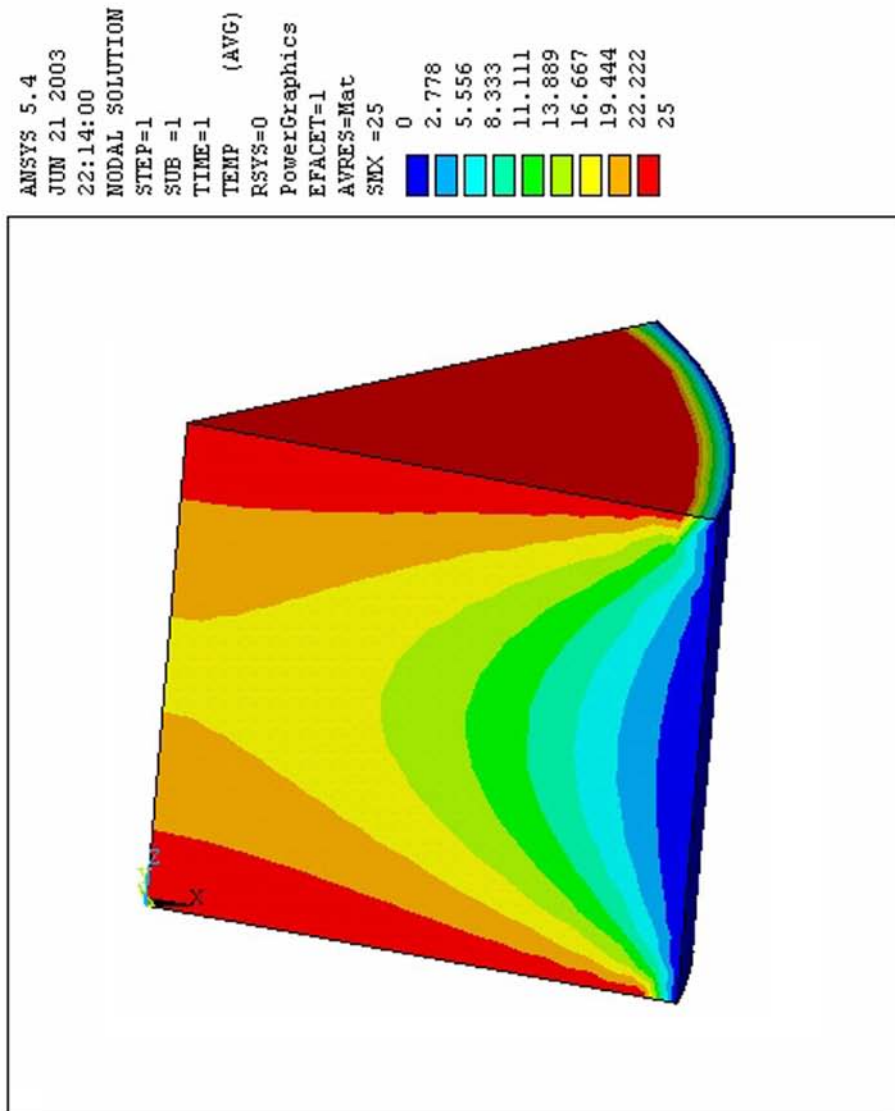


Fig. 5.27: Simulated temperature distribution in turmeric at $L/D = 1.00$ (volume, $46.33 \times 10^{-7} \text{ m}^3$)

5.5 Specific energy consumption

The specific energy consumption increased from 55 to 94 kJ/kg with increasing grinding temperature from -60 to -8°C and it was between 174-181 kJ/kg for the grinding temperatures ranging between 55 to 60°C (Table 5.12), following a second order polynomial relationship. The increase in specific energy consumption with grinding temperature was found to be significant at 1% level. It is obvious that at low grinding temperatures, degree of brittleness of turmeric increased due to which it required less energy in grinding.

The relationship between specific energy consumption and grinding temperature can be represented by the following equation:

$$E = 109.32 + 1.052T + 0.0025T^2 \quad (5.2)$$

$$(R^2 = 1)$$

where E is the specific energy consumption in kJ/kg

5.6 Liquid nitrogen consumption and throughput

The liquid nitrogen consumption for cryo-grinding of turmeric was found to be 0.76 kg/kg of turmeric ground, when the cooling capacities of vented nitrogen vapour and ground product not utilized. When the cooling capacity of vented nitrogen vapour was utilized, the consumption was 0.57 kg/kg and when both the cooling capacities were utilized it was 0.40 kg/kg of turmeric ground. The inlet temperature condition was 25°C and the nitrogen temperature at the exit of the conveyor was - 65°C. The temperature rise in the mill during grinding was 50°C. The operating pressure of liquid nitrogen spraying system during grinding was 3.5 bar (gauge). The refrigerant loss was 4.5% at this set pressure. Increase of pressure in the vessel above this, though can increase the feed rate, it was limited to the above pressure since it caused over flooding of food surfaces with liquid nitrogen. This is similar to the conditions obtained in immersion freezing and hence heat transfer coefficients would fall as a result of local film boiling condition on the food surface.

The product throughput in cryogenic grinding is many times that obtained with conventional grinding. It can be seen from Table 5.13 that with an increase

in particle size, the feed rate also increased correspondingly under cryogenic conditions, following a linear relationship represented by eq. (5.3):

$$Y = 1.12 X - 139.44 \quad (5.3)$$

$(R^2 = 1)$

where Y is the feed rate in kg/h and X is the particle size in micrometers.

The Table 5.13 shows that for a fineness of 171.27 μm , the feed rate (throughput) in conventional grinding was 35 kg/h, whereas in the cryogenic grinding, the same will be 52 kg/h, indicating an increased throughput of 1.5 times as compared to conventional grinding.

5.7 Quality evaluation

Figs 5.28 (a) and 5.28 (b) show the micrographs of particles ground under conventional and cryo-ground conditions.

The essential oil yield and gas chromatographic analysis results are presented in Tables 5.13 and 5.14. The volatile oil and oleoresin content of conventionally ground turmeric samples were found to be in the range of 3.4-3.8ml /100gm, 4.9 – 6.0g /100g respectively and for cryo-ground samples it was in the range of 4.5 – 5.2ml / 100g and 5.8 – 7.2g / 100g respectively. The entire analyses confirm that the cryo-ground process produces a better particle size range and shape parameters than the conventional grinding process with an increased essential oil yield and better retention of monoterpenes.

Samples	Feed rate (kg/hr)	Grinding Temperature (°C)	Specific energy consumption (kJ/kg)
Cryo – 1	20	-8	94
Cryo – 2	15	-28	81
Cryo – 3	35	-54	59
Cryo – 4	40	-60	55
Conventional – 1	35	60	174
Conventional – 2	20	55	181
		F value	164 ^a

Table 5.12: Effect of grinding temperature on specific energy consumption

^a Significant at 1% level

Samples	Feed rate (kg/hr)	Temperature (°C)	Volatile oil (ml/100gm)	Moisture (ml/100g)	Oleoresin content (g/100g)	Particle size (µm)
Cryo – 1	20	-8	4.5	6.7	7.2	149.29
Cryo – 2	15	-28	4.7	6.5	5.8	136.78
Cryo – 3	35	-54	5.1	7.6	6.7	156.56
Cryo – 4	40	-60	5.2	7.15	6.45	151.45
Cryo – 5	45	-35	4.9	7.2	6.8	143.56
Conventional – 1	35	60	3.4	8.1	4.9	171.27
Conventional – 2	20	55	3.8	7.6	6.0	190.48

Table 5.13: Volatile oil and essential oil content analysis of turmeric powder

Sample		Cryo	Conventional
Compounds	RT (min)		
α - Phellandrene	11.37	0.7131	0.2258
ρ - Cymene	11.943	0.3438	0.0690
1,8 – Cineole	12.263	0.6018	0.1403
Ar – Curcumene	27.948	2.7935	2.1602
Zingiberene	28.442	5.1761	4.7963
β - Farnesene	29.358	4.9287	4.4661
Ar – Turmerone	33.192	54.9147	53.0565
Turmerone	34.232	17.8749	16.5035
Curione	36.203	4.6918	4.3319

Table- 5.14: GC of essential oil samples of turmeric powder (%concentration)

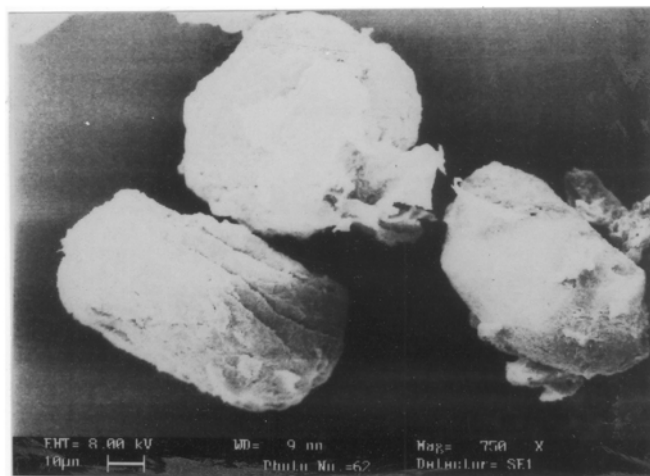


Fig. 5.28 (a): Scanning electron microscope (SEM) photograph of conventionally ground turmeric particles



Fig. 5.28 (b): Scanning electron microscope (SEM) photograph of cryo-ground turmeric particles

5.8 Development of scale-up procedure

An attempt has been made to present a generalized expression for the distribution function encompassing various controlling mechanisms of fracture, to obtain a rational method for reliable scale-up. Sizing and milling simulation by mass-size balance method is the most rational and informative method (Viswanathan and Mani, 1992; Zoga et al., 1996; Frank and Polke, 1999). The available models suffer from the following drawbacks (Viswanathan and Mani, 1992):

1. The fraction of material in a particular size interval falling into the same size interval after breakage is assumed to be zero however in actual practise, it is always greater than zero can be considerable.
2. The selection and distribution functions are assumed to be independent of each other whereas there exists a strong interrelationship between the two.
3. The validity of the generally used size-discrete time-continuous models may be questionable especially for industrial scale.
4. None of the available models assumes forms of the distribution function that have any theoretical basis.

To overcome the above said drawbacks, a mathematical model called the “Distributed Fracture Model” was developed by Viswanathan and Mani (1992).

The distributed fracture model

The feed is assumed to be of a function of distribution of sizes. The numbering of sieves starts from the top (coarsest) interval. The first (coarsest) interval contains particles in the size range (d_2, d_1) where d_1 and d_2 are the largest and the smallest particle sizes in the top interval, respectively. Similarly j -th interval contains particles in the size range (d_{j+1}, d_j) .

The average particle size d_{aj} in the j -th interval equals $(d_j d_{j+1})^{1/2}$. It is evident that a larger particle in the i -th interval can fall into i -th interval itself after breakage. That is, if $b_{i,j}$ represents the fraction of material in j -th interval falling

into i -th interval after breakage, then $b_{i,j}$ is a non-zero quantity. The available models in the literature assume $b_{i,j}$ to be zero which can be highly erroneous (Viswanathan and Mani, 1992). The mass balance in words (Zoga et al., 1996):“

The material in the i -th interval after grinding equals the unbroken material in that interval, plus the material falling after breakage in i -th interval from all sizes from the i -th interval to the top size interval”

Mathematically this can be expressed as:

$$\sum_{j=1}^i b_{i,j} (1 - P_{j,j}) f_j + f_i P_{i,i} = p_i \quad (5.4)$$

f_i and p_i represent the fraction of material in i -th interval in the feed and product respectively. In eq. (5.4), f_j represents the fraction of material in j -th interval remaining unbroken. In matrix form, eq. (5.4) becomes

$$D \underline{f} = \underline{p} \quad (5.5)$$

$$D = b (I - P) + P \quad (5.6)$$

$$b_{i,j} = B_{i,j} - b_{i+1,j} \quad (5.7)$$

In eq. (5.6) I is the identity matrix, P is the diagonal matrix with elements $P_{j,j}$, and b is the lower triangular matrix with elements b_{ij} .

Now the product distribution (\underline{p}) can be predicted for any feed distribution and grinding time, if the matrices b and P can be predicted.

The various fracture controlling mechanisms abbreviated as (FCM), that can be considered are as follows:

FCM1 – activation of edge flaws in fibrous (one dimensional) materials

FCM2 – activation of edge flaws in flaky (one dimensional) materials

FCM3 - activation of surface flaws in flaky (two dimensional) materials

FCM4 - activation of edge flaws in volumetric materials

FCM5 - activation of surface flaws in volumetric materials

FCM6 - activation of volume flaws in volumetric (three dimensional) materials.

Following the procedure for deriving theoretical expressions for $b_{i,j}$, $P_{j,j}$ ((Viswanathan and Mani,1992) the generalized equation valid for all the controlling mechanisms can be obtained as follows:

$$P_{j,j} = \exp [- C_j (d_{aj} / d_j)^n] \quad (5.8)$$

$$B_{i,j} = \frac{1 - \exp (- C_j x_{ij}^n) [1 + C_j x_{ij}^n - C_j x_{ij}^{2n}]}{1 - \exp (- C_j)} \quad (5.9)$$

where

$$\begin{aligned} x_{ij} &= d_i / d_j & \text{if } d_i \leq d_j \\ &= 1 & d_i > d_j \end{aligned} \quad (5.10)$$

$$d_{aj} = (d_j d_{j+1})^{1/2} \quad (5.11)$$

$$n = (n_f + n_s) / 2 \quad (5.12)$$

$$n_f = \begin{cases} 1 & \text{for FCM1,FCM2,FCM4} \\ 2 & \text{for FCM3, FCM5} \\ 3 & \text{for FCM6} \end{cases} \quad (5.13)$$

$$n_s = \begin{cases} 1 & \text{for FCM1} \\ 2 & \text{for FCM2, FCM3} \\ 3 & \text{for FCM4, FCM5, FCM6} \end{cases} \quad (5.14)$$

It can be seen from eqs (5.11), (5.13) and (5.14) that theoretically 'n' can be between 1 and 3. It can also be useful to assume eq. (5.9) to be a valid empirical expression for n lying between 0 and 1. Since controlling mechanism is usually not known, n should be kept as a parameter whose value can be anywhere between 0 and 3.

It can be also noted that the distribution function in eq. (5.9) is independent of d_{aj} , and depends only on the maximum size in j-th interval ($x_i = d_i / d_j$). Since according to physical logic $b_{j,j}$ should be non-zero, from eqs (5.7) and (5.8) we have,

$$b_{j,j} = \frac{\exp(-C_j) - \exp(-C_j x_i^{n+1}) [1 + C_j x_i^n - C_j x_i^{2n+1}]}{1 - \exp(-C_j)} \quad (5.15)$$

Now this model can be used to predict the product distribution if the parameters n and C_j (as a function of d_{aj}) are known. These can be obtained from experiments and scaled-up appropriately for use in industrial scale.

Calculational procedure to obtain C_j :

Feed material of a single size interval (d_{j+1}, d_j) should be ground for a certain time and product size distribution is obtained. Let the fraction of the original material remaining in j -th interval after breakage be P_{expt} . Since P_{expt} contains $(1 - P_{j,j}) b_{j,j}$ fractions of material breaking into the same (original feed) intervals, the actual fraction remaining unbroken is:

$$P_{j,j} = (P_{\text{expt}} - b_{j,j}) / (1 - b_{j,j}) \quad (5.16)$$

where $b_{j,j}$ is given by Eqn. (5.14). The parameter C_j can be obtained from Eqn. (5.8) as

$$C_j = - (d_j / d_{aj})^n \ln (P_{j,j}) \quad (5.17)$$

From prior knowledge of the fresh feed rate G , the feed size distribution g , and the classification matrix C , and by obtaining the values of C_j and n from batch experiments, appropriate scale up of grinding process for use in industrial level is possible by coupling with the material balance equations which can be illustrated as follows.

A schematic view of a typical grinding mill is shown in Fig.5.29. It consists of a grinding mill whose product goes to a classifier, where the undersize from it is taken as product and the oversize is recycled. The recycled oversize is mixed with fresh feed and fed to the grinding mill. Kapoor and Meloy (1991) has concluded that assumption of first order classifier behaviour is a good approximation to characterize a classifier function. Accordingly, the classifier selects a set fraction by weight c_i of the entering material of size interval i and sends it to tailings or oversize. The numbering of the intervals is from the top so that $i = 1$ corresponding to coarsest size interval.

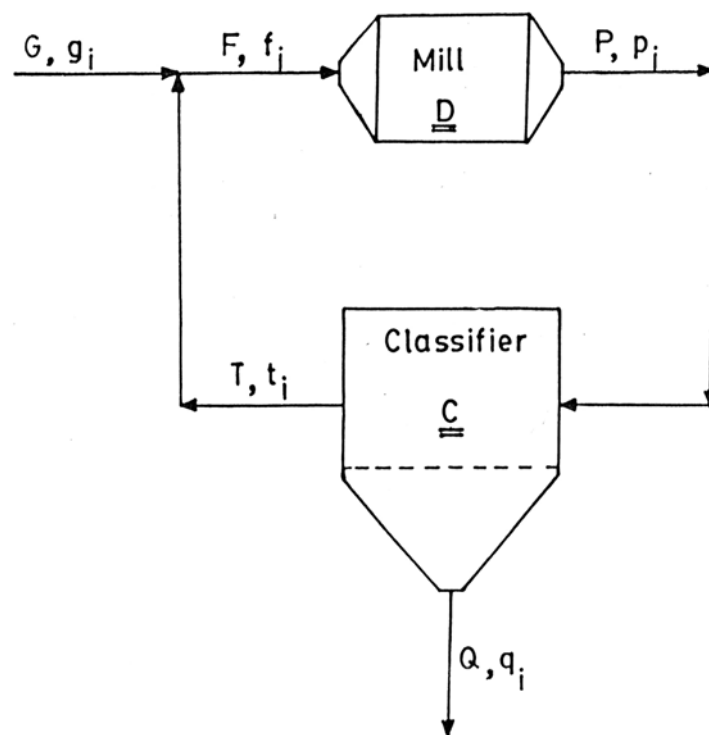


Fig. 5.29: Schematic view of a typical grinding mill

Referring to Fig. 5.29, c_i can be stated as:

$$Tt_i = Pp_i c_i \quad (5.18)$$

$$Qq_i = Pp_i(1 - c_i) \quad (5.19)$$

where T , is the identity matrix, t_i , the size distribution of oversize in the i th interval, P , the diagonal matrix with diagonal elements P_{jj} , p_i , size distribution of the product from the mill in the i th interval, c_i , the fraction of material in the i th interval sent to oversize tailing by classifier, Q , the diagonal matrix with diagonal elements q_i and q_i , size distribution of product from classifier in the i th interval.

The overall material balance for the mill is simply given by,

$$G = Q \quad (5.20)$$

$$F = P = G + T \quad (5.21)$$

$$P = Q + T \quad (5.22)$$

where G , is the fresh feed rate and F , the matrix with elements f_i .

Now the circulation ratio R , can be given as the ratio of recycle rate to fresh feed rate or

$$R = T/Q = T/(P - T) \quad (5.23)$$

The fresh feed fraction f_i in the i th interval is

$$f_i = (Gg_i + Tt_i)/(G+T) \quad (5.24)$$

where g_i , is the size distribution of fresh feed in the i th interval, t_i , the size distribution of oversize from classifier in the i th interval.

From eqs (5.18), (5.21) and (5.22),

$$f_i = (g_i + Rt_i)/(1+R) \quad (5.25)$$

From eqs (5.16) and (5.21), the recycle fraction t_i is given as

$$t_i = (1+R)/R p_i c_i \quad (5.26)$$

In matrix notation, eqs (5.23) and (5.24) can be written respectively as

$$f = 1/(1+R)/(g+Rt) \quad (5.27)$$

$$t = (1+R)/R Cp \quad (5.28)$$

where C is the diagonal matrix with diagonal elements c_i

From eqs (5.25) and (5.26),

$$f = 1/(1+R)g + Cp \quad (5.29)$$

Multiplying both sides of the eq. (5.27) by the mill transformation matrix, D and substituting eq. (5.5) leads to

$$p = 1/(1+R)Dg + DCp \quad (5.30)$$

Eq. (5.28) can also be written as

$$(I - DC) p = 1/(1+R)Dg \quad (5.31)$$

Eq. (5.29) can now be solved for p as

$$p = 1/(1+R) (I - DC)^{-1} Dg \quad (5.32)$$

where I is the identity matrix

Since the elements of vector p has to be unity, from eq. (5.30) circulation ratio R can be obtained as

$$R = \sum_{i=1}^N (m_i) - 1 \quad (5.33)$$

where m_i are the elements of $m = (I - DC)^{-1} Dg$ (5.34)

Product size distribution can be obtained from eq. (5.17) as

$$q = (1+R) (I - C) p \quad (5.35)$$

The validity of the model is illustrated through a problem example in Appendix C.

6. Discussion

6.1 Engineering properties of turmeric

The deformation behaviour of turmeric under ambient and low temperature conditions as determined by stress-strain test indicates rapid increase of particle strength as the particle size and temperature is lowered. This means that strain rate and complexity of the stress system have the effect of decreasing ductility at lower temperatures. A material breaks or cracks along defects in the structure. For a large piece, which has many defects, a small stress may cause breakage but, as the size is reduced, fewer defects remain and breakage strength increases. The observed increasing set of modulus of elasticity and maximum stress intensity values as the temperature is lowered from ambient to cryogenic, may be due to (i) the differences in spatial arrangement depending on the brittleness as well as embrittled effect due to cryogen and (ii) the increase of interatomic and intermolecular forces because of the decrease in the disturbing influence of atomic and molecular vibrations. Since elastic reaction is due to the action of these intermolecular and interatomic forces, one would expect the elastic moduli to increase as the temperature is lowered.

Also it has been seen that the hardness and ultimate stress increase as the temperature is lowered. The line of reasoning could be the less vigorous vibration of the atoms of the material and the requirement of larger applied stress, due to the decreased thermal agitation of the atoms. The increased brittleness of turmeric during cryogenic conditions may be attributed to the absence of slip systems due to low temperature embrittlement. Slip systems are directions within the material in which the plane can slip away easily over one another. The dislocations can move most easily through the material in the direction of slip planes. When a stress is applied to turmeric sample the atomic bonds rupture at some points on the surface. The crack then propagates causing the fracture. This means that at low temperatures, however, the attractive intermolecular forces are more effective than the thermal energy “lubricant” and the material deforms less readily. The role of dislocation is useful in explaining

the yield strength and brittleness of solids like food materials (Wigley, 1992). The observed variation of stress intensity factors indicate that strain energy is not uniformly distributed throughout the particle and is concentrated around holes or other discontinuities where the radius of curvature is small. The reason may be due to the presence of greater localized stresses than the mean stress values in the material.

It can be seen from the Finite Element analyses of stress distribution of turmeric under ambient and low temperature conditions, that stress intensity non-uniformities are higher at low volumes. The stress intensity non-uniformity can be attributed to higher concentration of stresses at the outer surface when the radius of the product decreases. For products of lower volume the radius of the product is smaller. The application of a high stress intensity on the product for instance with a smaller radii , results in a more severe focussing effect causing higher non uniformity in stress intensity.

6.2. Finite element prediction of fracture mechanism

Although the preliminary two-dimensional finite element micro-mechanical studies did not result in quantitatively exact predictions of the fracture properties of turmeric they do produce accurate information regarding the behaviour of a crack as it approaches, intercepts, and passes a fiber.

6.2.1 Effect of interface bond strength

The primary influences of low-fiber-to-matrix bond strength were to reduce the potential for fiber failure and to encourage crack deflection along the fiber-to-matrix interface. In addition, the weakened interface typically failed away from the primary crack tip. This process is akin to micro cracking and absorbed energy that would otherwise contribute to primary crack extension. As shown in Fig.6.1, the strain energy release rate was greatly reduced by the formation of secondary crack surface. If the interface was too weak, however, and failed completely before primary crack extension occurs, the actual stress intensity at the crack tip was greater than that calculated from the fracture mechanics theory.

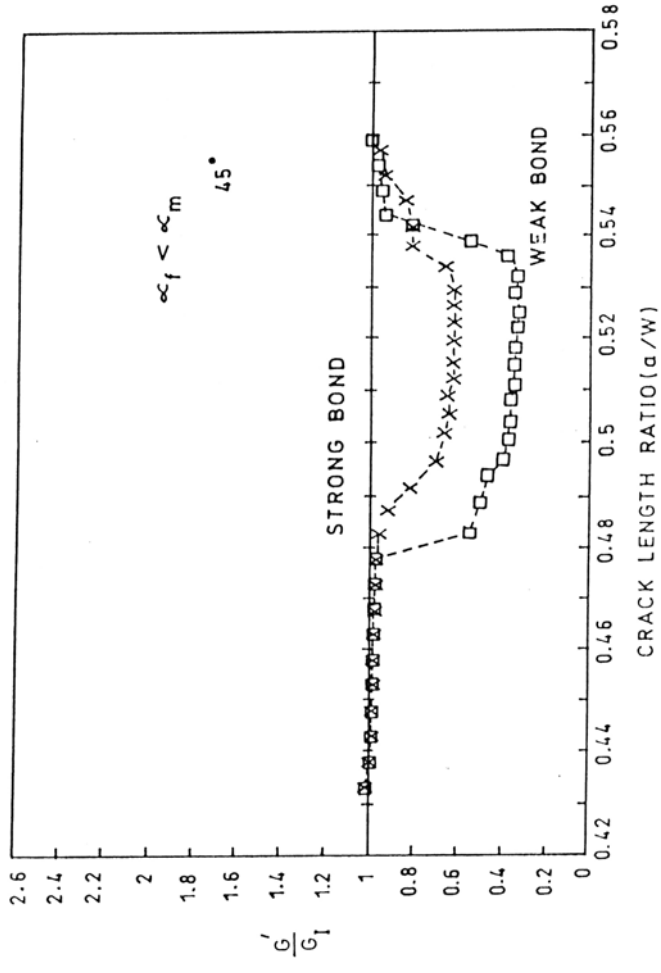


Fig. 6.1: Effect of interface bond strength on the normalized strain energy release rate

6.2.2.1 Effect of residual stress state

Different states of residual stress resulted in different failure processes. In general, residual tension in the fiber caused crack deflection in the matrix and also caused fiber failure. Fiber failure resulted in a large increase in the strain energy release rate for that crack growth increment. This stress state also encouraged fiber-matrix interface failure, so that the crack deflection along the fiber-matrix interface were diminished.

The stress states of residual compression in the fiber, and absence of residual stresses, encouraged crack pinning. Because these residual stress states did not increase the driving force for the interface cracks, the crack deflection will be along the fiber. This is apparent from the $G'/G_1 v_s$ crack length curves presented in Fig. 6.2.

6.2.3 Effect of fiber orientation

For fiber orientations of 90° with respect to the crack plane, crack pinning occurred, provided that the fiber did not fail. The primary effect of decreasing the orientation of the fiber from 90° was to promote crack deflection as it intercepted the fiber. Crack deflection along the interface resulted in a reduced strain energy release rate. As shown in Fig. 6.3, crack deflection through an angle of 60° resulted in a more significant reduction in the G' than through an angle of 30° .

When the fiber - matrix interface bond was strong and the fiber was in residual tension, fiber fracture occurred for all fiber orientations except the 0° orientation. This suggests that the critical angle for crack deflection when this fiber is strongly bonded to the matrix is less than 30° . When the interface was weak, fiber fracture occurred only for the 90° and 60° fiber orientations. Here, the critical fiber orientation for crack deflection was between 60° and 45° . Crack deflection along the fiber-to-matrix interface occurred for all the inclined fiber orientations discontinuities which were under no residual stress (fiber B) or were under residual compression (fiber C).

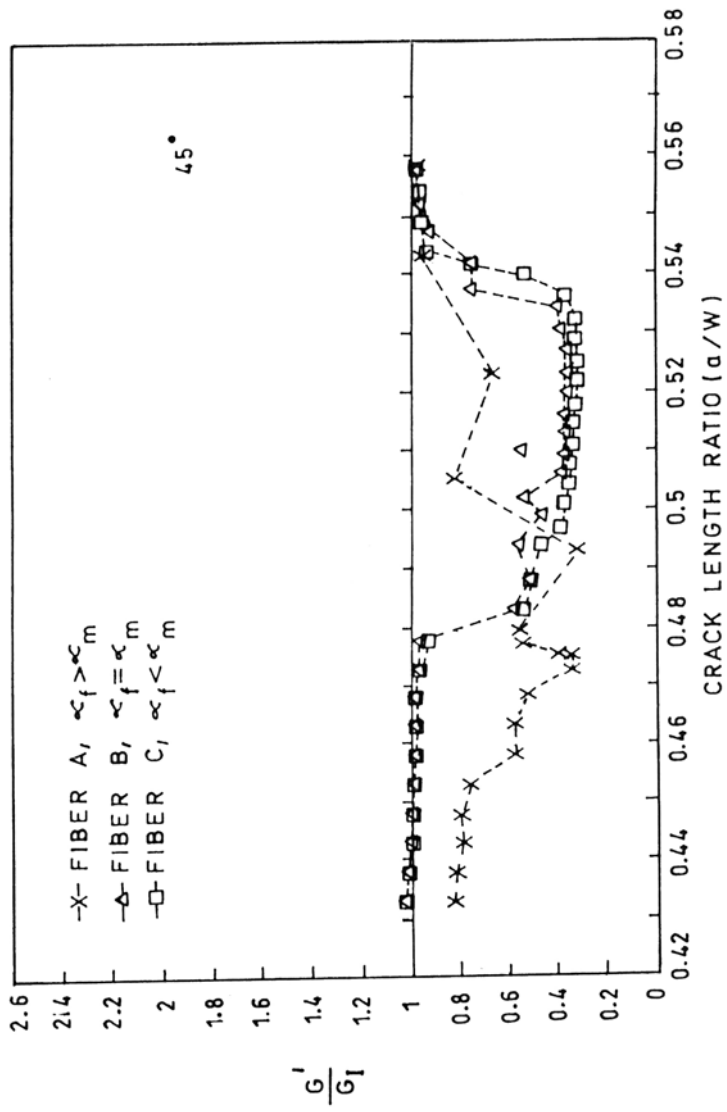


Fig. 6.2: Effect of residual stress state on the strain energy release rate for the weakly bonded fiber

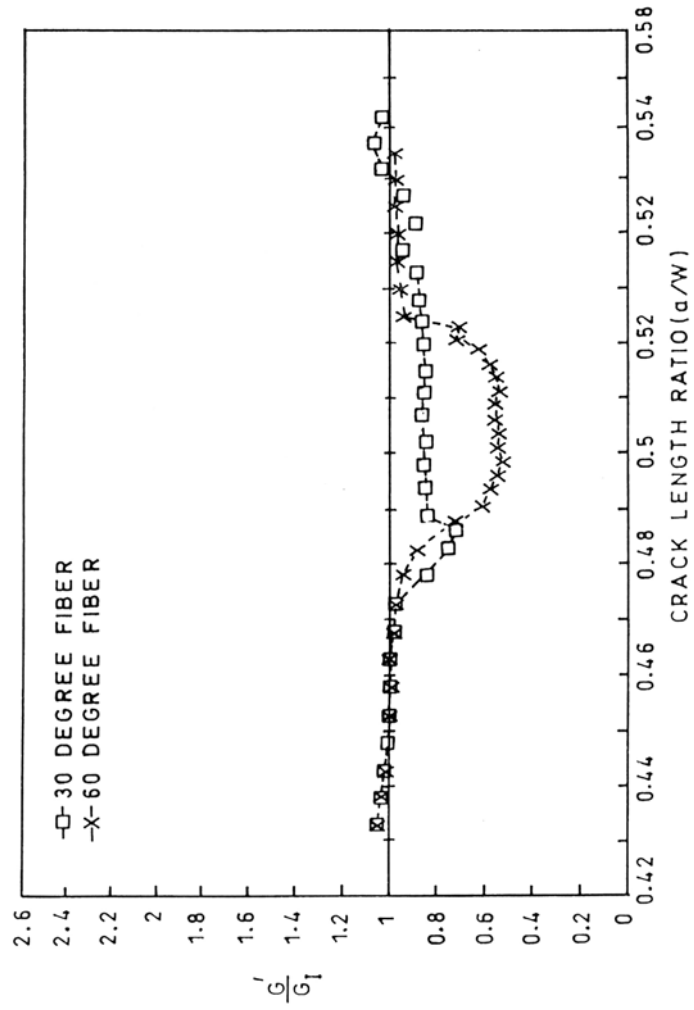


Fig. 6.3: Effect of fiber orientation on the strain energy release rate when $\alpha_f = \alpha_m$

6.3 Fracture mechanism under different size reduction methods

The fracture mechanism under different size reduction methods is based on the hypothesis that the particle shapes are related to the way in which crack run through the original stressed material. At the crack tip a strong stress concentration provides the elastic energy necessary to maintain fracture (Theocaris, 1995). Since interaction of the crack tip stress field with inhomogeneities causes complex wave phenomena which affect crack propagation and direction (Theocaris, 1995), it can be thought that material inhomogeneity (the presence of pores) could change stress patterns as the crack propagated. This phenomenon might then be responsible for the production of elongated particles of low ϕ values at smaller sizes, which theoretically should not arise from crack trajectories resulting from impact loading of a homogenous material (Rivas, 2001).

The results of particle shape versus size for the various size reduction mills show that all forms of size reduction showed decreases in ϕ as size decreased, implying the presence more elongated particles at smaller sizes. The majority of the results substantiate Allen's observation (Rivas, 2001) that materials of the same composition do not have the same shape throughout their size range. The production of greater numbers of elongated particles by size reduction at smaller sizes has been noted by a number of researchers (Buchen et al., 1993; Kumar, 1996; Pradid et al., 1998; Rolland et al., 1999; Rivas, 2001). It was also observed in this study that the standard deviation associated with the mean value of ϕ for a given sieve increased as size decreased for all modes of size reduction. The increase (although not statistically significant) was particularly noticeable for the 90 μm sieve. This observation implies a greater heterogeneity in particle shapes at smaller sizes.

When considering how particle shape changes with increased milling the results for size reduction in the unscreened hammer milling concur with the results of blender, screened hammer and cryo-milling: with few exceptions, as the degree of milling increased, particles shapes at any given particle size became more rounded. Fig. 6.4 illustrates this effect for blender milling. Changes

in particle shape with increased amount of grinding have been demonstrated (Pradid et al., 1998) including a decrease in the number of elongated particles (Meloy and Williams, 1994; Bridgewater, 1995). According to theoretical considerations (Rivas, 2001) the lower velocity and thinner blade of the blender should initiate fracture for fewer flaws and thus produce greater numbers of elongated particles. The results of blender milling support such observations.

The interaction between the pores and an advancing crack causes the fracture to continue on two planes, resulting in a cleavage step at their intersection, a phenomenon reported to occur during fracture of metals (Kirchner et al., 1994), various organic polymers (Kirchner et al., 1994; Salman et al., 1995) and extruded wheat starch plasticized with glucose and water (Ollett et al., 1991). The propagation of the fracture front into different cleavage planes as a result of fracture front stress waves, interacting with pores and other material inhomogeneities (Morrissey and Rice, 1998; Bridgewater, 1995) has been previously reported. The prolonged cleavage step formation and undercutting leads to the formation of a sliver of the elongated material during the fracture process. Independence of slivers formed from the main fracture face has previously been reported (Salman and Gorham, 1997) and substantiated for turmeric in Fig. 6.5 where the fracture planes have intersected approximately at right angles. The cleavage step formation and undercutting during crack propagation is shown schematically in Fig. 6.6. In the figure, bottom diagrams are sections of the fracture plane drawn perpendicular to advancing fracture front at the point of vertical arrows in top diagrams.

The number of elongated particles formed may be attributed solely to the number of fracture faces, with the number of slivers formed on each fracture face being proportional to the number of pores which the propagating fracture encounters. The presence of elongated particles admixed with particles reduced in size by "more normal" fracture processes (Lawn, 1993), would also account for the observed increase in the standard deviation for ϕ at smaller sizes.

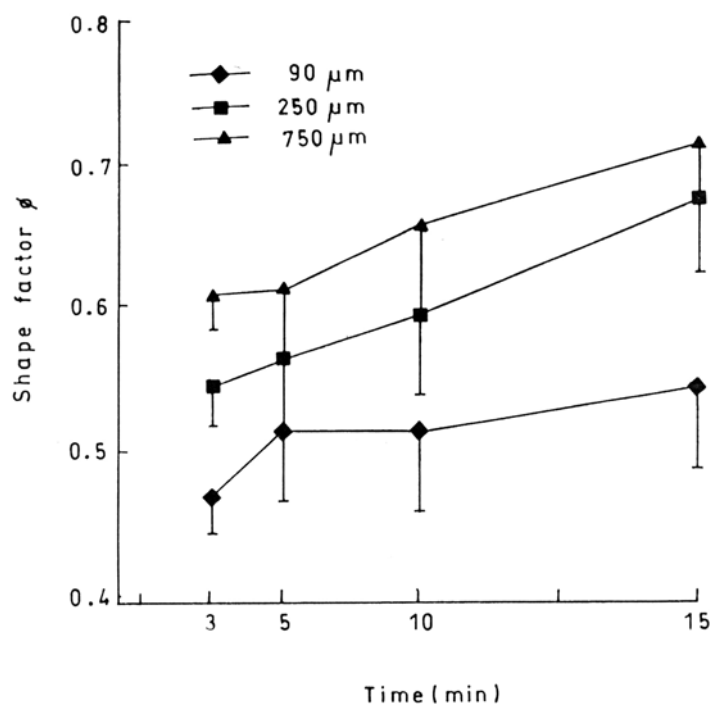


Fig. 6.4: Changes in particle shape ϕ with time of blender milling for particles in sizes of 710, 250 and 90 μm . Error bars are $\pm 95\%$ confidence limit

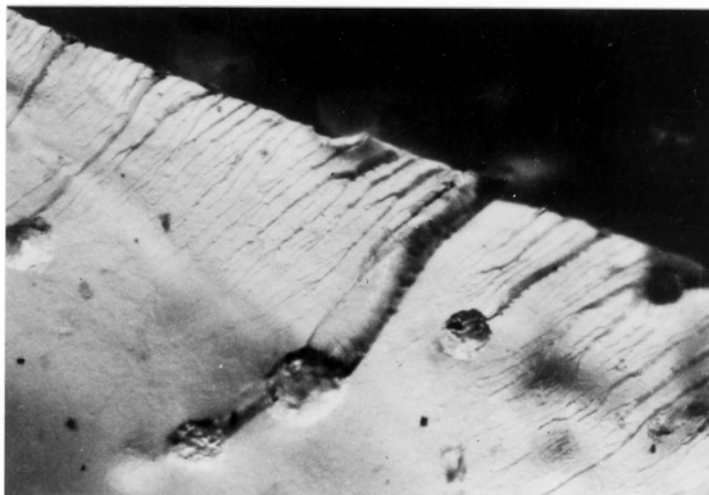


Fig. 6.5: Interaction of two fracture planes, approximately at right angles, showing elongated particle being fractured at a different point to the fracture plane on which it was residing

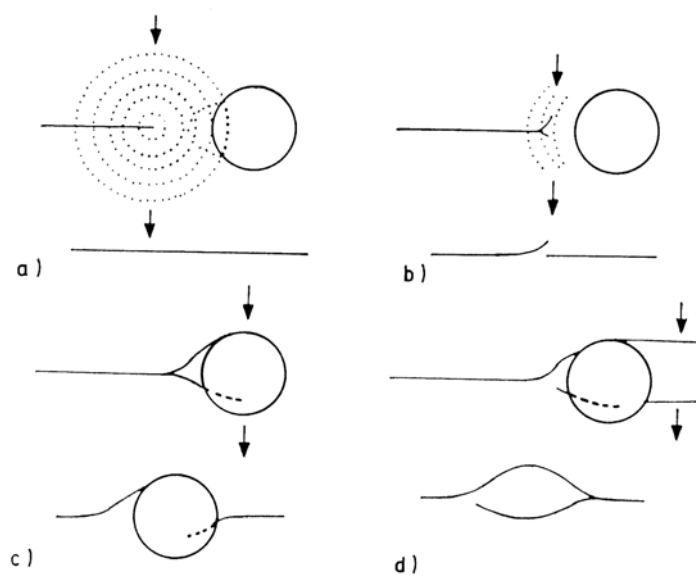


Fig. 6.6: Cleavage plane formation and overlap during four stages of crack propagation

- (a) Advancing fracture moving left to right with stress waves emanating from tip of crack
- (b) Reflected stress waves disturbing fracture front causing crack bifurcation
- (c) Crack branch continuing to deviate from original fracture plane due to further stress waves reflection from the pore
- (d) Main fracture planes spreading outwards and undercutting fracture plane of crack branch, creating a sliver that will create an elongated particle

6.3.1 Hammer mill

The fracture mechanisms occurring in particles that are hammer milled are effected by effect of particle selection in the mill (Gorham and Salman, 1998) and secondary breakage (Bourgois et al., 1994). These factors obviously influence fracture events to the extent that shape distributions versus size are markedly different from those arising from single impact breakage.

6.3.1.1 Unscreened hammer mill

The effects of any impact from the hammer should produce from the fracture surfaces the same elongated particles as were formed in the other types of mills. But, in the hammer mill the close proximity of the surrounding metal casing ensures that kinetic energy derived from fracture is used in secondary breakage (Bourgois et al., 1994). As elongated particles would be unlikely to break along their longest axis the particles formed from secondary breakage of any slivers would be more blocky than elongated (Kumar, 1996).

6.3.1.2 Screened hammer mill

The above effects of secondary breakage on particle shape would be expected to be more pronounced due to the presence of screen. However, ϕ decreased with decreasing particle size. The addition of the screen causes an extra selection effect that is size dependent, so that particle that would normally pass into the container or bag unaltered in unscreened hammer milling, are retained on the screen. The strong outward air currents in the mill would blow out particles smaller than the screen aperture, generally the smaller elongated particles. Larger particles are retained to be rebroken. The relative number of these preferential selection events occurring on the screen (and expulsion of elongated particles) determines how much the mean value of ϕ is lowered at smaller sizes compared to hammer milling without the screen. Additional lowering of ϕ due to the screen would be expected from particles that have been broken and the kinetic energy associated with the progeny particles causes secondary breakage on the screen rather than on the upper casing. In this case

any slivers formed during this secondary breakage would likely be ejected from the mill, and not subject to further breakage which would increase their ϕ values.

6.3.2 Blender mill

A single impact of a particle by the blender blade does not effect the same degree of size reduction as does impact in the hammer mill or cryo-grinding. Therefore fewer fracture surfaces and their concomitant slivers will be produced. The slivers will dominate the particulate population at small sizes leading to low ϕ values, while at larger sizes, values of ϕ will be high due to the blocky shaped particles that are produced. This will be particularly so when time of grinding is small. The presence of elongated slivers could account for creation of small particles (fines) in the early steps of grinding whose mass is independent of the mass of material being ground (Perry and Green, 1997). This is because the number of elongated fines created will be proportional to the new fracture surface area. New fracture surface area will be dependent solely on material that has been selected for breakage, and unless the mill is grossly under loaded this will be independent of mass of material in the mill (Durnrn and Hogg, 1990). As the time of milling in the blender is increased, ϕ increased for all sizes. The slivers which are produced and which continue to be available for breakage in such a closed system would likely fracture across their short axes forming more blocky shapes (Kumar, 1996). Increasing ϕ values as the number of passes in the hammer mill increased would likely be due to a similar mechanism: smaller elongated particles returned for milling preferentially fracturing across their short axes, so increasing ϕ values.

6.3.3 Cryogenic mill

The affects of any impact should produce from the fracture surfaces the same elongated particles as found in other methods described. But in the cryogenic mill, the uniform embrittled lattice developed by the cryogen, as well as the close proximity of the intermeshing pins of the grinding zone allowing equal opportunity for the particles to size reduction, ensures that kinetic energy derived

from fracture is used in secondary breakage. The observation of increased ϕ formed during cryo-milling compared with impact breakage gun, hammer milling and blender mills, implies that considerable secondary breakage and efficient grinding has occurred. Referring to the Fig. 5.14, the shape factor of the conventionally –ground (without cryogen) turmeric is as low as 0.04. But the shape factors of cryo-ground turmeric particles are mostly above 0.23. The microscopic pictures of ground particles [Figs 5.17 (a) and 5.17 (b)] under conventional (without cryogen) and cryogenic grinding methods as well as the shape analysis done with the computerized inspection system confirm these results.

6.4 Thermal effects of fracture particulates

It can be seen from Tables 5.10 and 5.11 and Figs 5.15 and 5.16 that the description of fracture particulates in terms of log-normal parameters allow quantitative characterization of fracture under comminution. Since fracture is a rate process with random fluctuation of stresses, thermal effects during fracture cannot be calculated from continuum mechanics. Impact energy and heat capacity of the material provide a basis for prediction of thermal effects along with log-normal parameters. In any fracture process, it may be supposed that cracks propagate in all directions resulting in multiple stages of binary cleavage of the body, producing particles (Wanibe and Itoh, 1999). If a body of original diameter D_0 is subjected uniformly to n stages of binary cleavage (in three directions), the result would be cubicle particles of diameter D

$$D/D_0 = (1/2)^n \quad (6.1)$$

If n is a random variate, distributed normally, then it can be shown from the description of section 2.3.2 that particle diameter, as a random variate D , is distributed log-normally. While the normal probability law is basic in physics as the error function, it is not appropriate for characterizing random physical variables such as D , that can never take negative values. Nor is the normal probability suitable for binary -cleavage processes that determine magnitudes exponentially [as D in eq.(6.1)], because the error function characterizes

magnitudes that vary additively. From these arguments, it follows that particles produced by crushing or grinding (binary cleavage) would have sizes distributed log-normally, while those produced by other means, for example, by attrition probably would not. While these characterizations are only approximate, they can provide practically useful quantitative information, wherein it is possible to predict the maximum temperature rise that could occur for a particle of a given diameter fractured under grinding and similar unit operations and as a principled basis for rational experimental design and for modeling effects in a field where deterministic thermodynamics and continuum mechanics is not possible to apply. However confirmations of predictions for sub-micron or nano-particles would require measurements with electron microscopy and related sophisticated instruments which is beyond the scope of the present study.

6.4.1 Temperature distribution

The results of mapping and analysis of temperature distribution shown (Fig. 5.18 to 5.27) have indicated that the temperature gradient changes predominantly up to the length to diameter ratio of 0.5, beyond that the temperature distribution remains constant or uniform including distribution pattern, irrespective of change in volume or change in boundary conditions. The reasons for this behaviour can be attributed to the choice of boundary conditions as well as the steady state heat conduction assumed. The effect of temperature gradient can be much more predominant in transient analysis where time-temperature history is involved, which is beyond the scope of the present work.

The comparison of analytical and FEM simulated results (2.90% relative difference) suggests that finite element formulation is capable of predicting temperature distribution within the fractured particulate of turmeric.

6.5 Specific energy consumption

It can be seen from the grinding temperature effects on specific energy consumption (Table 5.12) that chilling of the product induces brittleness and low temperature of the mill prevents excessive temperature of the grinding zone,

which also keeps oil and moisture conditions in the product in the crystallized condition during milling and avoids clogging. Also there can be large aggravation of the weak points in crystal structure after chilling. These aspects make the material to shatter more easily and thus less energy and less heat formation are involved during cryogenic grinding as compared to conventional grinding which can be attributed to a large aggravation of the weak points in a crystal structure after chilling.

6.6 Liquid nitrogen consumption and throughput

Generally, as the spray pressure increases the flow rate of the liquid increases. The operating pressure of liquid nitrogen spraying system during grinding was limited to 3.5 bar (gauge). Increase of pressure in the vessel above this, though can increase the feed rate, was limited to the above pressure since it caused over flooding of food surfaces with liquid nitrogen. This is similar to the conditions obtained in immersion freezing and hence heat transfer coefficients would fall as a result of local film boiling condition on the food surface.

For many food products, pre-chilling to as low a temperature as -196°C (Boiling point of liquid nitrogen under a pressure of one atmosphere absolute) is not necessary to get the desired degree of improvement in milling efficiency. Temperatures of -60°C to -100°C are often quite enough. Such temperatures are realizable with the help of nitrogen and naturally the total usage of nitrogen can be economized.

It can be seen from Table 5.13 that at a constant degree of fineness the product throughput can be increased as much as 1.5 times when liquid nitrogen is used. This can be a measure of the way in which chilling can increase the ease of shattering of the material, heat generation at the point of fracture being greatly reduced.

The optimum milling efficiency can be achieved when the available cooling energy in the evaporated nitrogen is optimized. The energy wasted in the form of unused cooling power in the exhaust gases from the mill becomes apparently nothing if the nitrogen actually blows out of the milling plant at room temperature. Such ideality is virtually may not be possible in practice, though however it is

common to collect the waste gas, compress it and use it for other purposes, such as pneumatic conveying of sensitive materials and blast cleaning of air filters.

Apart from actual waste of cooling power through cooling the material and the exhaust gases, more than is really necessary, the cooling load has to be balanced to the energy input of the mill. Obviously, the greater the output and the greater the required degree of fineness, the greater the heat input at the mill which will have to be offset by the degree of pre-cooling applied.

6.7 Quality evaluation

As indicated by the size and shape analysis as well quality evaluation [Tables 5.9, 5.13 and 5.14, Figs 5.2 (a) and (b), 5.3 (a) to (c), Figs 5.15 (a) and (b)] of turmeric powder, particles with better particle size range and shape parameters, choice of size reduction systems such as low temperature grinding, produce increased yield in terms of quality and quantity as compared to poorer shape and size parameters. The reason for achievement of better quality and quantity may be attributed to the development of an uniform embrittled lattice and crystallized conditions due to the effect of cryogen preventing any loss of volatile oils occurring during cryogenic conditions, provision of equal opportunity for the feed material to undergo complete size reduction without exposing any pores, thus preventing the elongation of particles.

The increased values of shape factors during cryogrinding as compared to conventional grinding indicate prevention of elongation of particles, and greater homogeneity of material. The greater volatile oil yield and oleoresin content may be due to the influence of geometry and dimension of the product leading to concentration of essential oil related to certain size and shape much like an optical lens concentrating light waves (Datta, 1990) as evidenced from the present study.

7. Summary

The objective of the present study is to investigate fracture mechanism, crack propagation and thermal effects of fracture particulates during size reduction under ambient and cryogenic conditions and also to understand the finer mechanical interactions between the growing crack and constituent material properties through finite element method, with reference to spices, in particular turmeric (*Curcuma Longa*) as a model food material.

Engineering properties

The test data generated for the analysis of fracture mechanism were in terms of engineering properties such as Modulus of elasticity, Poisson's ratio deformation loads, fracture stress and strain energy values at different interface temperatures. Maximum stress intensity values were estimated by Finite element method under different loads, at ambient and low temperature conditions. The low temperature studies were conducted with temperature range -8°C to -62°C . The most commonly used cylindrical shape, of turmeric was considered in the estimation of above properties. Stress intensities were investigated by varying the height to base ratio by keeping the volume constant. The deformation /fracture behaviour of turmeric under the said conditions to determine the hardness, toughness and brittleness values of turmeric is also included. The values of Poisson's ratio under ambient and low temperature conditions were found to be 0.33. The range of densities were between $1190 - 1350\text{ kg/m}^3$ (under ambient conditions) whereas under cryogenic conditions it was in the range $1780 - 1812\text{ kg/m}^3$. Strength and hardness are important parameters governing size reduction. The threshold parameters estimated such as critical load and corresponding critical length indicate that threshold load is much less than applied load (applied load F , threshold load F^* and crack length 'a' under ambient and cryogenic conditions (Temp. -8°C), respectively were: $F - 11.30$ and 6.89 N , $F^* - 0.7$ and 0.5 N , $a - 5$ and $3\text{ }\mu\text{m}$) and thus the process of breakage or damage of turmeric is essentially a fracture and is not deformation-controlled. The ductile-brittle behaviour of turmeric as determined by the familiar stress-strain test indicated that food materials such as turmeric exhibit much

greater change in the modulus of elasticity and yield strength at low temperatures. As the temperature is decreased, interatomic and intermolecular forces tend to increase because of the decrease in the disturbing influence of atomic and molecular vibrations. Since elastic reaction is due to the action of these intermolecular and interatomic forces, elastic moduli is expected to increase as the temperature is decreased. When the brittleness and hardness increases, toughness decreases which means, that resistance to deformation increases and resistance to fracture decreases. The material does not retain its ductility from ambient to low temperatures, making it to fracture more readily than at ambient temperature. The ultimate stress, modulus of elasticity and stress intensity values increase from ambient to low temperature conditions indicating increase in hardness. For example, under low temperature conditions with the temperature range -8°C to -62°C , values of ultimate stress, modulus of elasticity and maximum stress intensity values respectively were found to be in the range of 3.6 to 5.7×10^6 Pa, 4.9 to 6.3×10^9 Pa, and 9.2 to 10.9×10^6 Pa. And under ambient conditions the above values respectively were 3.4×10^6 Pa, 2.1×10^9 Pa, and 5.5×10^6 Pa for the sample categorized as large (size: diameter, 10.6×10^{-3} m and length, 52.5×10^{-3} m). The reason may be due to the differences in spatial arrangement depending on brittleness as well as embrittled effect due to cryogen. Also, the thermal vibrations of atoms in the structural lattice is strongly temperature dependent and is less effective in assisting dislocation at low temperature.

It was seen that the modulus of elasticity increases with the decrease in size. For example when compared with the sizes of the samples categorized as large and small (Dimensions - diameter, 10.6×10^{-3} m , length, 52.5×10^{-3} m and diameter, 6.41×10^{-3} m, length, 28.23×10^{-3} m), modulus of elasticity and maximum stress intensity values under ambient conditions were found to be in the range $2.1 - 6.9 \times 10^9$ Pa, and $5.5 - 10.2 \times 10^6$ Pa respectively and under cryogenic conditions ($- 8^{\circ}\text{C}$), the values were in the range of $4.9 - 20.9 \times 10^9$ Pa and $3.6 - 34.6 \times 10^6$ Pa respectively. This indicates increase in material strength, more stiffness which means less material deforming on the application of a fixed force. A material breaks or cracks along defects in the structure. For a large

piece, which has many defects, a small stress may cause breakage but, as the size is reduced, fewer defects remain and the breakage strength increases. That is particle strength increases with decreasing particle size.

Product volume and height-to-base ratio, have pronounced effect on stress intensity, strain energy and deformation loads. Stress intensity appeared to be more concentrated at the outer layer or circumference of the product than the rest. The stress intensity increased as the height to base ratio increased from 0.25 to 1.0. Also for an increase in volume there is a decrease in strain energy indicating wider stress distribution throughout the material ($10.6 - 33.4 \times 10^{-3}$ N-m under ambient conditions and $12.1 - 40 \times 10^{-3}$ N-m under cryogenic conditions ($- 8^{\circ}\text{C}$). With the volume kept constant and for different L/D ratios (0.25, 0.5 and 1.00) strain energy increases with an increase in L/D ratios under ambient and cryogenic conditions, indicating more stress concentration. For example, the sample with the dimensions, (L : 52.5×10^{-3} m and D: 10.6×10^{-3} strain energy increased from 0.54 to 3.9×10^{-3} N-m under ambient conditions and under cryogenic conditions ($- 8^{\circ}\text{C}$) it increased from 1.1 to 5.1×10^{-3} N-m. The estimated stress intensity factors indicated that strain energy is not uniformly distributed throughout the particle and is concentrated around holes or other discontinuities where the radius of curvature is small. The stress intensity factor increases with an increase in deflection and a decrease in radius of curvature.

Finite element model studies

Finite element model studies was attempted to simulate and analyze the fracture mechanism and crack growth of turmeric with reference to its morphology as composite structure of fibers. A two- dimensional finite element model for crack growth is developed, in which residual stress state, fiber orientation and interface bond strength are varied. Fracture paths are predicted for individual fibers at discrete locations with respect to primary crack plane. The effect of fracture path and the microstructure on the stress intensity at the crack tip is monitored by calculating the rate of release of strain energy after each increment of crack growth. The finite element crack growth algorithm which is developed can determine the effects of constituent properties and morphology on

the fracture behaviour of a brittle food material. The method accurately predicted stress intensity and provided good graphical interpretation of fracture paths.

It was found from finite element modeling that (a) residual tension in the fiber promoted crack deflection in the matrix but increased the potential for fiber fracture and for interface debonding, (b) absence of residual stress, and particularly residual compression in the fiber encouraged crack pinning and crack deflection along weakened fiber matrix interfaces (c) weak fiber-to-matrix interfaces promote primary crack deflection and microcracking away from the crack tip (d) fibers oriented normal to the crack plane locally pin the crack, and required increased driving forces for further crack propagation and the inclined fibers cause the crack to deflect, reducing the stress intensity at the crack tip (e) crack deflection along the fiber-to-matrix interface was more predominant in the fiber in residual compression, only weakly bonded to the matrix. These weakened interfaces lead to deflection of the crack parallel to the fiber axis. The presence of the compressive residual stresses decreased the stress intensity when the crack intercepted or deflected along the fiber and (f) development of a 2-dimensional Finite element model for crack growth permits the isolation of the effects of individual features on the fracture behaviour and the strain energy release rate after each increment of crack growth. Strain energy release rate calculated with the Finite element method was in close agreement with the theoretical relationship obtained from the linear elastic fracture mechanics theory.

Due to their two-dimensional character, the finite element studies did not result in quantitatively exact predictions of the turmeric's fracture properties. They did produce useful information regarding behaviour of a crack as it approaches, intercepts and passes a fiber and it is possible to compare FEM predicted mechanisms of fracture to those observed in the experiments.

Thermal effects of fracture particulates

Cylindrical specimens of turmeric, impacted diametrically were found to have size distributions, that plotted as straight lines on log-normal graphical coordinates. Generalized log-normal properties were estimated for these particle-size distributions and found to correlate with impact kinetic energy per unit

volume of the specimen. The various properties estimated under ambient and cryo-treated conditions, such as surface-volume ratio, energy density, combined strength parameter were found to be: 3.5×10^3 to 1.14×10^6 (m^{-1}), 2.8×10^5 to 7.9×10^7 J / m^3 and 70 to 81.1 J / m^2 respectively. These log-normal parameters along with material properties were utilized to calculate the temperature rise of fracture particulates. The calculated ΔT were plotted as a function of size of particles. Local temperature rise of up to 40.5 and 26.9°C were found for particle size of 12 microns or lower for ambient and cryogenic conditions respectively. While these characterizations are considered approximate, they provide quantitative information and a principled basis for modeling effects, in a field where deterministic thermodynamics and continuum mechanics is not applicable, such as fracture which is a rate process with random fluctuation of stresses.

The finite element modeling of temperature distribution inside turmeric has been attempted and validated. The pattern of distribution was similar for the variation in size, length to diameter ratio varying between 0.25 to 1.00 keeping the volume constant and different boundary conditions considered. Under all these conditions, the temperature gradient corresponding to length to diameter ratio 0.5 was predominantly effective and beyond this the effect was almost negligible or constant. Considering two samples having different physical parameters, the distribution was symmetrical on either side, when the top and bottom surface temperature of the product was maintained at 25°C and lateral surface at -8°C , and non-symmetrical when the temperature at the top and bottom the product was at 25°C and lateral surface at 0°C .

Fracture mechanism under different size reduction methods

The investigation on fracture mechanisms under different size reduction methods reveal that both material properties and size reduction methods were shown to affect particle shape, enabling fracture progress in a given material to be studied if particles of specific shapes are to be produced by comminution. Particles of elongated shape were small in size in two different impact mills, which are attributed to material inhomogeneity. As fractures propagated, stress field interactions with the pores caused cleavage step formation. Undercutting of these cleavage steps caused small particles of elongated shape to be liberated,

increasing the number of elongated particles at lower sizes. Formation of a uniform embrittled lattice, attaining material homogeneity, eliminating elongation of particles at lower sizes and secondary breakage were responsible for better shaped particles in the low temperature grinding. Differences in the shape versus size distribution between conventional and cryo-ground materials was surmised to be due to the manner in which particles are selected for breakage within the mill.

Specific energy, liquid nitrogen consumption and throughput

The material shatter more easily, requiring less energy and heat formation during cryogenic grinding as compared to conventional grinding which can be attributed to aggravation of the weak points in a crystal structure after chilling. The specific energy consumption increased from 55 to 94 kJ/kg as the temperature was increased from -60 to -8°C and it was between 174-181 kJ/kg for the grinding temperatures ranging between 55 to 60°C following a second order relationship given by $E=109.32 + 1.052T + 0.0025T^2$ where E is the specific energy consumption in kJ/kg, and T is the grinding temperature.

The optimum milling efficiency could be achieved when the available cooling energy in the evaporated nitrogen was optimized. When the cooling capacity of vented nitrogen vapor and ground product was not utilized, the liquid nitrogen consumption for cryo-grinding of turmeric was found to be 0.76 kg/kg of turmeric ground, whereas when the cooling capacity of vented nitrogen vapor was utilized, the consumption was 0.57kg/kg of turmeric ground.

The product throughput was increased as much as 1.5 times, at a constant degree of fineness when liquid nitrogen was used. For an increase in particle size, the feed rate also increased correspondingly under cryogenic conditions, following a linear relationship represented by, $Y = 1.12 X - 139.44$ where Y is the feed rate in kg/h and X is the particle size in microns. For a fineness of 171.27 μm , the throughput in conventional grinding was 35 kg/h whereas it was 52 kg/h for cryo-grinding indicating 1.5 times increase in throughput as compared to conventional grinding.

Quality evaluation

Experimental studies to analyze, characterize and compare sizes and shapes of the turmeric particles ground by conventional and cryogenic method were conducted. Some of the estimated key shape parameters for turmeric particles like average Feret's size, average Martin's size, aspect ratio, perimeter, shape factor, specific length and specific width were found to be 88.20 μm , 37.81 μm , 0.69, 625 μm , 0.74, 295 μm and 24.70 μm respectively for conventional grinding and for cryo-ground turmeric particles it is 8.56 μm , 0.69, 46.70 μm , 0.74, 21.50 μm and 5.26 μm respectively. The cryo-ground turmeric materials are much finer than the conventional ones. Volume mean diameter or weight mean diameter of cryo-ground turmeric is 50 μm smaller than conventionally ground turmeric. Eighty percent of the particles by weight are less than 257 μm in the case of conventionally ground turmeric and 198 μm in the case of cryo-ground turmeric samples. Maximum particle size is 472 μm and 296 μm for conventional and cryo-ground turmeric respectively. The quality evaluation studies included, essential oil yield and gas chromatographic analysis. The volatile oil and oleoresin content for conventionally ground turmeric samples was found to be in the range of 3.4 – 3.8 ml/100g, 4.9 - 6.0 g /100g respectively and for cryo-ground samples it was in the range of 4.5 –5.2 ml/100g and 5.8 - 7.2 g/100g respectively. The percentage concentrations of compounds like α - phellandrene, p - cymene, 1,8 - cineole, Ar - curcumene, zingiberene, β - farnesene, Ar - turmerone, turmerone and curlone obtained after the the gas chromatographic analysis of essential oil samples of turmeric powders were: 0.71, 0.34, 0.60, 2.79, 5.18, 4.93, 53.06, 17.87 and 4.69 respectively for cryo-ground samples and for conventional ones it was 0.23, 0.07, 0.14, 2.16, 4.80, 4.47, 54.91, 16.50 and 4.33 respectively. The entire analyses confirm that the cryo-grinding process produce a better particle size range and shape parameters than the conventional grinding process with an increased essential oil yield and better retention of monoterpenes.

Development of scale -up procedure

The generalized expressions have been presented for the distribution function encompassing the various possible fracture controlling mechanisms, using the “Distributed Fracture Model”. A simple mathematical procedure is described by which to obtain the scale-up relation. The procedure is illustrated with the aid of an example by coupling with the material balance equations. The equations can be used for design, scale-up and simulation of grinding and for calculating the fraction of material in any size interval falling into the same size interval after breakage.

Scope for further work

1. The finite element crack growth simulation for turmeric should be extended to three dimensional modeling to include fiber interaction effects and thermal stresses.
2. Parametric studies considering effects of surface treatments such as cryogenic immersion, spraying and additives on the fracture behavior of food materials can be investigated. The thermal effect characterization of fracture particulates correlating log-normal parameters and energy density be extended to sub-micron or nano particles for an overall confirmation of prediction to any scale or type of impact.
3. As the grinding properties of some food systems such as cocoa-sugar mix, spice mix are not the same, studies relating the fracture mechanism, crack formation, particles shape and size characteristics, including simulation and modeling under different size reduction methods, can also be performed.
4. The finite element temperature distribution studies in the present work were valid for the linear region of the test data generated confining steady state conditions and did not contain time-temperature history. Since the effect of non - linear properties have a prominent role in the real comminuting situation, fracture mechanisms under ambient and cryogenic conditions involving transient thermal analysis can be investigated.

8. Appendix A

The displacement -based finite element method

The MSC Pal 2 finite element package used in this study is based on the displacement method. This appendix presents the equations used for the construction of the finite element model's global stiffness matrix and global load vector, and the solution of the unknown nodal displacements. The information in this appendix was taken from Zienkiewicz (2000), Bathe (1996) and MSC Pal 2 reference manual (1989).

A.1. Nodal displacement and forces

A typical finite element e is defined by nodes i, j, m, \dots and straight line boundaries. In the element coordinate system defined in Fig. A.1, the displacement of a node point, u_i can be completely described in terms of six components

$$u_i = [u_x, u_y, u_z, \theta_x, \theta_y, \theta_z]^T \quad \text{----- (A.1)}$$

A set of generalized forces is associated with each of the nodal displacements as shown in Fig. A.1. This set is a column vector written as

$$p_i = [p_x, p_y, p_z, m_x, m_y, m_z]^T \quad \text{----- (A.2)}$$

For plane problems, the translation in the z -direction and rotation about the x -, y -, and z - axes can be eliminated so that each node has only two displacement degrees of freedom:

$$\hat{u}_i = \begin{bmatrix} u_x \\ u_y \end{bmatrix} \quad \text{----- (A.3)}$$

The components of the element displacements are represented as the vector sum of the nodal displacements

$$u^e = \begin{bmatrix} \hat{u}_i \\ \vdots \\ \hat{u}_m \end{bmatrix} \quad \text{----- (A.4)}$$

where m is the node points connected by element e . Likewise, the vector of element forces is,

$$p^e = \begin{bmatrix} p_i \\ \vdots \\ p_m \end{bmatrix} \quad \text{----- (A.5)}$$

A.2. Element displacement functions

The displacement within an element are related to the nodal point displacements by the displacement transformation matrix, or shape function, Φ

$$v^e = \begin{bmatrix} u(x,y) \\ v(x,y) \end{bmatrix} = \Phi^e \cdot u^e \quad \text{----- (A.6)}$$

where v^e is the displacement vector for element e .

In the present study, it is assumed that displacements vary linearly across the element. The shape function for the four node quadrilateral element and the three node triangular element are:

Four node quadrilateral element

$$\Phi^e = 1/4 [(1+r) (1+s), (1-r) (1+s), (1-r) (1-s), ((1+r) (1-s)] \quad \text{----- (A.7)}$$

Three node triangular element

$$\Phi^e = 1/4 [2 (1+s), (1-r) (1-s), (1+r) (1-s)] \quad \text{----- (A.8)}$$

These formulations guarantee interelement compatibility. The variables r and s are the local element coordinates, defined in Fig. A.2, which satisfy $(-1 \leq r \leq +1, -1 \leq s \leq +1)$. The shape functions provide a one to one mapping between the local (r,s) and the global (x,y) coordinates. The relationship for coordinate transformation is

$$\begin{bmatrix} \frac{\partial \Phi}{\partial r} \\ \frac{\partial \Phi}{\partial s} \end{bmatrix} = \begin{bmatrix} \frac{\partial x}{\partial r} & \frac{\partial y}{\partial r} \\ \frac{\partial x}{\partial s} & \frac{\partial y}{\partial s} \end{bmatrix} \begin{bmatrix} \frac{\partial \Phi}{\partial x} \\ \frac{\partial \Phi}{\partial y} \end{bmatrix} = J \begin{bmatrix} \frac{\partial \Phi}{\partial x} \\ \frac{\partial \Phi}{\partial y} \end{bmatrix}$$

----- (A.9)

where J is the Jacobian matrix. Inverting the Jacobian matrix, the global derivatives of the shape function are obtained:

$$B = \begin{bmatrix} \frac{\partial \Phi}{\partial x} \\ \frac{\partial \Phi}{\partial y} \end{bmatrix} = J^{-1} \begin{bmatrix} \frac{\partial \Phi}{\partial r} \\ \frac{\partial \Phi}{\partial s} \end{bmatrix} \quad \text{----- (A.10)}$$

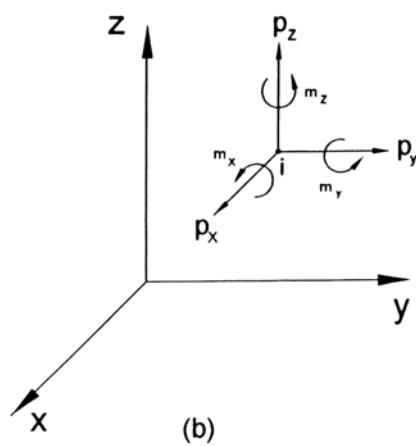
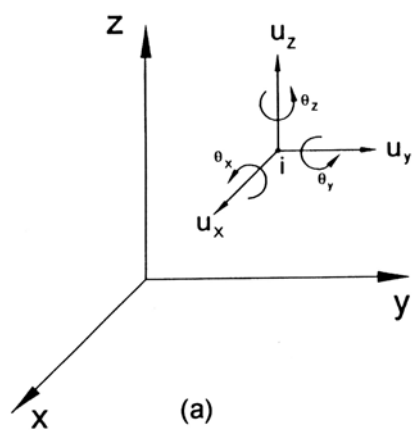


Fig. A.1: (a) Grid point degrees of freedom
(b) Grid point forces

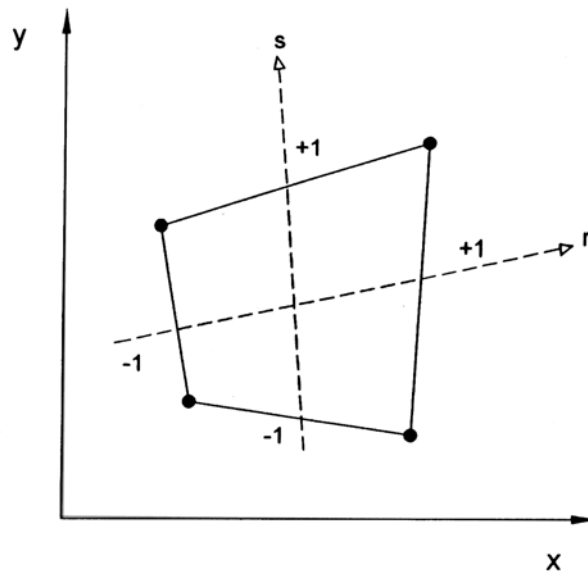


Fig. A.2: Definition of coordinate frames

A.3. Element strains

The strains within an element are determined from the element displacement vector and strain-displacement matrix, D.

$$\varepsilon^e = D \cdot v^e \quad \dots\dots\dots (A.11)$$

The matrix D is a matrix of differential operators which satisfies continuity requirements and is given by

$$D = \begin{bmatrix} \frac{\partial}{\partial x} & 0 \\ 0 & \frac{\partial}{\partial y} \\ \frac{\partial}{\partial y} & \frac{\partial}{\partial x} \end{bmatrix} \quad \dots\dots\dots (A.12)$$

Strains which arise upon the application of a temperature load are represented as “initial strains”. For a plane stress, isotropic element subjected to a temperature change θ° with thermal diffusivity α , the initial strains are

$$\varepsilon^0 = \begin{bmatrix} \alpha\theta^\circ \\ \alpha\theta^\circ \\ 0 \end{bmatrix} \quad \dots\dots\dots (A.13)$$

A.4. Element stresses

Assuming linear elastic material behaviour, the element stresses are related linearly to element strains through

$$\sigma = \begin{bmatrix} \sigma_{xx} \\ \sigma_{yy} \\ \sigma_{xy} \end{bmatrix} = C (\varepsilon - \varepsilon^0) \quad \dots\dots\dots (A.14)$$

where C is the elasticity matrix defined by

$$C = \frac{E}{(1-\nu^2)} \begin{bmatrix} 1 & \nu & 0 \\ \nu & 1 & 0 \\ 0 & 0 & \frac{1-\nu}{2} \end{bmatrix} \quad \dots\dots\dots (A.15)$$

A.5. Element stiffness matrix

The stiffness matrix of an element e, with constant thickness t and area A, is defined by

$$K^e = [B]^T \cdot C \cdot [B] \cdot t \cdot A \quad \dots\dots\dots (A.16)$$

K^e relates the node point displacements to the vector of node point forces, p^e ,

$$K^e \cdot v^e = p^e \quad \dots\dots\dots (A.17)$$

A.6. The system equations

In order to assemble the q element equations into a set of equations which describe the behaviour of the total finite element model, the quantities defined in local element coordinates must be transformed into the global coordinates.

With the element local node point degrees of freedom listed in v^e , the global displacements are the components of a column vector, d , given by

$$d = \sum_{e=1}^q \begin{bmatrix} v^e \end{bmatrix} \quad \text{..... (A.18)}$$

The global force vector, P and the global displacement matrix, K , are assembled similarly.

$$P = \sum_{e=1}^q \begin{bmatrix} p^e \end{bmatrix} \quad \text{..... (A.19)}$$

$$K = \sum_{e=1}^q \begin{bmatrix} k^e \end{bmatrix} \quad \text{..... (A.20)}$$

The unknown displacement vector is determined from the force vector and the stiffness matrix, such that static equilibrium of the system is satisfied. That is,

$$K \cdot d = P \quad \text{..... (A.21)}$$

Several numerical methods are available for determining d . The finite element program used in this research used the method of matrix decomposition.

Since K is a symmetric matrix, it may be factorized into a lower triangular matrix, L , and an upper triangular matrix, U , so that eq. (21) becomes

$$L \cdot U \cdot d = P \quad \text{..... (A.22)}$$

Forward substitution is then performed to solve for Y in the matrix equation:

$$L \cdot Y = P \quad \text{..... (A.23)}$$

The solution for the vector d is obtained by backwards substitution in the matrix equation:

$$U \cdot d = Y \quad \text{..... (A.24)}$$

Upon solution, the components of the global displacement vector are related to the element stresses and strains through the relationships given in sections A. 3 and A.4.

9. **Appendix B**

Model strain energy calculation program

The following FORTRAN program was written to calculate the total strain energy contained in the finite element models. The program requires two input data files: the coefficients of the global stiffness matrix (file EQN.) and the values of the nodal displacements (file DSP.).

The file EQN. is created with the MSC ADCAP2 program, using the “Print Matrix, Full” option. The file DSP. is created with the MSC STAT2 program using the “Print Displacements, Full” option.

These files are formatted primarily for ease of visual inspection of the data. This required creative use of read statements and end-of-file checks to filter out text strings and blank lines.

```

c ***** PROGRAM ENERGY.FOR *****
c This program calculates the strain energy of a Pal2 FEM model
c from the stiffness "EQN." and the displacement "DSP." files.
C Strain energy is written to file"ESE."
c
$STORGAE:2
  real dvect(2500)
  character*16 junk,BLANK
  common dvect,nrow,junk
c
c nrow=2298
c
c open(unit=1,file='eqn')
c open(unit=2,file='dsp')
c open(unit=3,file='ESE')
c
c call DISPL(dvect,nrow)
c write(*,*) 'DISPL RAN'
c call CALC(dvect,nrow,U)
c write(*,*) 'CALC RAN'
c
c write(*,20) 'The total energy (uN um) is', U
C write(*,20) U
C write(3,20) 'Model Strain energy (uN um) is',U
20 format(a40,5x,f20.2)
c
c close(unit=1)
c close(unit=2)
c close(unit=3)
c stop
c end
C
C *****
C
C SUBROUTINE DISPL(DVECT,NROW)
c This turns the Pal displacement file into the displacement
c vector.
c CHARACTER*16 JUNK
c real dvect(2500)
c
c DO 5 J=1,10
c READ(2,'(A15)') JUNK
5 CONTINUE
c
c DVECT(71)=0.0
c DVECT(72)=0.0
C
c rjend=real(nrow)/2.
c jend=int(rjend)
c
c do 10 j=1,48
c read(2,*) node,xt,yt,zt,xr,yr,zr
c rnode1=2.0*(real(node))-1.
c rnode2=RNODE1+1.
c node1=int(rnode1)
c node2=int(rnode2)
c
c dvect(node1)=xt
c dvect(node2)=yt
10 continue
C
C DO 30 K=1,50
C DO 15 J=1,3
C IF (EOF(2)) GOTO 40
C READ(2,'(A15)') JUNK

```

```

15      CONTINUE
c
      do 20 j=1,55
      if (eof(2)) goto 40
      read(2,*) node,xt,yt,zt,xr,yr,zr
      rnode1=2.0*(real(node))-1.
      rnode2=RNODE1+1.
      node1=int(rnode1)
      node2=int(rnode2)

c
      dvect(node1)=xt
      dvect(node2)=yt
20      continue
30      continue
C
40      return
      end

C
C *****
C
      SUBROUTINE CALC(dvect,nrow,U)
C      This calculates the total strain energy in the Pal model.
c
      real DVECT(2500),temp(2500),KVAL(2500)
      character*16 junk,BLANK

c
c----- INITIALIZE TEMP ARRAY AND DISCARD JUNK IN EQN FILE -----
      read (1,(A1)) BLANK
      read (1,(A15)) junk
      read (1,(A1)) BLANK

c
      do 10 i=1,nrow
      temp(i)=0.0
10      continue
      U=0.0
c----- READ STIFFNESS EQUATION COEFFICIENTS -----
      do 50 i=1,nrow
      read (1,(A15)) BLANK
      read (1,20) junk,icol,junk,irow
20      format(a8,i5,a5,i5)

c
      rownum=real(icol)-real(irow)+1.
      numrow=int(rownum)
      WRITE(*,*)ICOL,IROW,NUMROW

c
      read(1,*) (kval(k),k=1,numrow)
      kval(numrow)=(kval(numrow))/2.

c----- PERFORM FIRST CALCULATION -----
      do 30 j=1,numrow
      rjj=real(irow)+real(j)-1.
      jj=int(rjj)

c
      temp(jj)=kval(j)*dvect(icol)+temp(jj)
      temp(icol)=kval(j)*dvect(jj)+temp(icol)

c
30      continue
50      continue
c
c----- PERFORM SECOND CALCULATION -----
      do 60 i=1,nrow
      U=U+(temp(i)*dvect(i))/2.
60      continue
      return
      end

```

10. Appendix C

Validation of the distributed fracture model

The following problem example illustrates the validity of the distributed fracture model developed. Consider for the grinding mill as shown in Fig.5.14. It is needed to calculate the product size distribution for (i) classifier set at 1 mm and (ii) classifier set at 1.5 mm. The grinding time is to be 10 min. The fresh feed belongs to a single size interval, from 1.5 to 2 mm. For describing size distribution, the values of 2, 1.5, 1 and 0 mm were used for d_i . This means that 3 intervals are considered that is $d_a = 1.73, 1.23$ and 0.5 mm. (For ex., d_{a1} from Eqn.(5.11) is $(2 \times 1.5)^{1/2} = 1.73$). The values of n and C_j obtained from batch experiments (Viswanathan and Mani, 1992) were used. From the experimental data it is seen that $n = 1$ and for a grinding time of 10 min, C_j was empirically given as

$$C_j = 0.75 d_j \quad \text{----- (C.1)}$$

Using the above data the matrices P, B, b and D are obtained from eqs (5.5) to (5.11) as follows:

$$P = \begin{bmatrix} 0.273 & 0 & 0 \\ 0 & 0.399 & 0 \\ 0 & 0 & 0.687 \end{bmatrix} \quad \text{----- (C.2)}$$

$$\begin{aligned} \{ P_{11} &= \exp [- C_j (d_{aj} / d_j)^n] \\ &= \exp [- 0.75 \times 2 (1.73/2)] \\ &= \exp [- 1.50 (0.865)] \\ &= 0.273 \} \end{aligned}$$

$$B = \begin{bmatrix} 1 & 0 & 0 \\ 0.752 & 1 & 0 \\ 0.451 & 0.606 & 1 \\ 0 & 0 & 0 \end{bmatrix} \quad \text{----- (C.3)}$$

$$b = \begin{bmatrix} 0.248 & 0 & 0 \\ 0.301 & 0.394 & 0 \\ 0.451 & 0.606 & 1 \end{bmatrix} \quad \text{----- (C.4)}$$

$$D = \begin{bmatrix} 0.453 & 0 & 0 \\ 0.219 & 0.636 & 0 \\ 0.328 & 0.364 & 1 \end{bmatrix} \quad \text{----- (C.5)}$$

Since the fresh feed is given to be only in the first interval (from 2.0 to 1.5 mm)

$$g = (1,0,0)^T \quad \text{----- (C.6)}$$

Considering the two cases of classification,

Case 1: Classifier set at 1 mm:

For this case

$$C = \begin{bmatrix} 1 & 0 & 0 \\ 0 & 1 & 0 \\ 0 & 0 & 0 \end{bmatrix} \quad \text{----- (C.7)}$$

From eq. (5.34) m is calculated to be

$$m = (0.82, 1.1, 1)^T \quad \text{----- (C.8)}$$

From eq. (5.33)

$$\text{circulation ratio, } R = 0.82 + 1.1+1-1 = 1.92 \quad \text{----- (C.9)}$$

From eq. (5.32),

$$\text{Size distribution of product from mill, } p = (0.281, 0.377, 0.342)^T \quad \text{----- (C.10)}$$

From eq. (5.28),

$$\text{Size distribution of oversize from classifier, } t = (0.427, 0.573, 0)^T \quad \text{----- (C.11)}$$

From eq. (5.35),

$$\text{Size distribution of product from classifier, } q = (0, 0, 1)^T \quad \text{----- (C.12)}$$

Case 2: Classifier set at 1.5 mm

For this case

$$C = \begin{bmatrix} 1 & 0 & 0 \\ 0 & 0 & 0 \\ 0 & 0 & 0 \end{bmatrix} \quad \text{----- (C.13)}$$

Following the similar procedure as above it is found that

$$R = 0.83 \quad \text{----- (C.14)}$$

$$p = (0.453, 0.219, 0.328)^T \quad \text{----- (C.15)}$$

$$t = (1, 0, 0)^T \quad \text{----- (C.16)}$$

$$q = (0, 0.4, 0.6)^T \quad \text{----- (C.17)}$$

It can be seen from the above that circulation ratio decreases as the classifier setting increases. The reason may be attributed to the assumption of grinding time as constant in the illustration. But in actual practice, a reduced R due to a larger classifier setting leads to greater grinding time in the mill which leads to production of more fines and further reduction of R .

11

Symbols and abbreviations

a	crack length measured in the y-direction [m]
a_1	initial crack length [m]
a_2	final crack length [m]
a_0	lattice constant [dimensionless]
a_s	surface area shape factor [dimensionless]
a_v	volume shape factor [dimensionless]
a^*	threshold value of crack length in change from a deformation-controlled to a fracture-controlled situation [μm]
A	area of particles [m^2]
A	cross sectional area of the sample in eq. (2.44) [m^2]
b	steepness constant [dimensionless]
b	remaining portion in front of crack in eq. (2.35) [m]
b	matrix with elements $b_{i,j}$
$=$	
b_{ij}	fraction material in j-th interval falling after breakage into i-th interval [dimensionless]
B	thickness [m]
B	brittleness in eq. (4.24) [$\mu\text{m}^{-1/2}$]
B	global strain displacement matrix in eq. (A.10)
B_{ij}	cumulative fraction material in j-th interval falling after breakage in less than size d_i [dimensionless]
c	radius of the specimen [m]
c	constant in eq. (4.6)
c_i	fraction of material in the i-th interval sent to oversize tailing by classifier
C	deflection [m]
C	diagonal matrix with diagonal elements c_i in eq. (5.28)
C	element elasticity matrix in eq. (A.14)
$C(a)$	specific compliance corresponding to crack length a [Pa m] ⁻¹
$C(o)$	critical compliance corresponding to crack length a_0 [Pa m] ⁻¹

C_j	parameter depending upon $d_{a,j}$ [μm]
C_v	heat capacity [$\text{J}/\text{m}^3\text{ }^\circ\text{C}$]
C_j	parameter depending upon $d_{a,j}$ [μm]
d	statistical mean particle size [μm]
d	global displacement vector in eq. (A.18)
d	diameter of the sample in eq. (4.19) [m]
d_j	maximum particle size in j-th interval [μm]
$d_{a,j}$	$(d_j d_{j+1})^{1/2}$ [μm]
dN	number of particles in a range [dimensionless]
dS/dV	local surface to volume ratio [m^{-1}]
dW/dV	local energy density [J/m^{-3}]
D	characteristic linear particle dimension diameter [m]
D	mill transformation matrix in eq. (5.30)
D	element strain displacement matrix in eq. (A.11)
D_{50}	geometric mean particle size [m]
D_{84}	particle size by volume or mass corresponding to 84% of the fracture particulate [m]
D	matrix in eq. (5.5) and (5.6)
$=$	
D_g	geometric mean diameter of the particle size distribution (by volume or mass) for the fracture particulate [m]
D_0	original diameter of the impacted body [m]
e	tensile strain [dimensionless]
e_v	volumetric strain [dimensionless]
E	Young's modulus of elasticity [Pa]
E	specific energy consumption in eq. (5.2) [kJ/kg]
f	maximum stress intensity [Pa]
\underline{f}	size distribution of mixed feed
f_i	fraction of feed material belonging to i-th interval [dimensionless]
f_H	surface constant

$f(x)$	density or frequency distribution in eq.(2.2)
F	force applied to a particle [N]
F	matrix with elements f_i in eq. (5.21)
F^*	threshold value of force in change from a deformation-controlled to a fracture –controlled situation [N]
$F(x)$	cumulative undersize fraction [dimensionless]
g	size distribution of fresh feed
g_i	size distribution of fresh feed in the i -th interval
$g(x)$	function of particle size in eq. (2.2)
$g(\bar{x})$	function of mean particle size in eq. (2.2)
G	fresh feed rate
G	elastic energy rate in eq. (2.27) [N/m]
G'	strain energy release rate [N / m]
G_c	critical energy release rate [N / m]
G_I	strain energy release rate in the absence of any fiber [N / m]
G_r	crack resistance [N / m]
H	hardness of a material [Pa]
I	moment of inertial [m ⁴]
I	identity matrix
$=$	
J	Jacobian matrix in eq. (A.9)
k	thermal conductivity [W/m°C]
k_H	volume constant for the particle in eq. (2.3)
K	global stiffness matrix in eq. (A.20)
K^e	element stiffness matrix in eq. (A.16)
K_c	toughness of a material [Pa m ^{1/2}]
K_t	stress intensity factor [dimensionless]
K_t	stress intensity factor in Mode I loading in eq. (2.23)
K_{t1}	stress intensity factor in Mode II loading in eq. (2.24)
K_{t2}	stress intensity factor in Mode III loading in eq. (2.25)
K_{tc}	mode I fracture toughness in eq. (2.37) [Pa m ^{1/2}]

L	length of the specimen [m]
L	lower triangular factorization of matrix K in eq. (A.22)
L_1	initial length of the specimen [m]
L_2	final length of the specimen [m]
m	vector with elements m_i
m	number of nodes connected by element e in eq. (A.4)
m_x	moment about the x-axis [N-m]
m_y	moment about the y-axis [N-m]
m_z	moment about the z-axis [N-m]
M	moment at centre point over the specimen [$N \times 10^{-3} \text{ m}$]
n	stages of binary cleavage of the equation $D/D_o = (1/2)^n$ [dimensionless]
n	uniformity index of distribution of the equation $\log_e \log_e [1/(1-F(x))] = n' (\log_e x - \log_e x'_R)$ [dimensionless]
n	exponent in the distribution function of eq. (5.8) [dimensionless]
n'	exponential index of the eq. (4.1)
n_f	flaw number of equation $(n_f + n_s) / 2$
n_s	shape number of equation $(n_f + n_s) / 2$
$N(D)$	cumulative number of particles (smaller than size D) in a sample of fracture particulate
N_n	total number of particles in a sample of particulate
p	size distribution of product from mill in the eq. (5.32)
p^e	force vector for element e
p_i	size distribution of product from mill in the i-th interval
p_i	generalized force vector at node point 'i' in eq.(A.5)
p_x	force in the x-direction [N]
p_y	force in the y-direction [N]
p_z	force in the y-direction [N]
P	diagonal matrix with diagonal elements P_{jj}
P	global force vector in eq. (A.19)

P	load applied in eq. (2.32) [kg]
P	perimeter of particle in eq. (4.7) [μm]
$P(u)$	cumulative normal probability function
$P(U_s)$	cumulative normal probability surface area function
$P(U_v)$	cumulative normal probability volume function
P	diagonal matrix with elements $P_{j,j}$
$=$	
P_{expt}	fraction of material remaining in the same interval after breakage = $P_{j,j} + b_{j,j} (1 - P_{j,j})$ [dimensionless]
$P_{j,j}$	fraction of material in j -th interval remaining unbroken [dimensionless]
q	size distribution of product from classifier
q	the number of elements in eq.(A.18)
q_i	size distribution of product from classifier in the i -th interval
Q	diagonal matrix with diagonal elements q_i
r	radius of curvature [m]
r	element coordinates in eq. (A.7)
r/c	ratio of radius of curvature to radius of specimen [dimensionless]
R	radius of force contact area in eq. (4.22) [m]
R	circulation ratio in eq. (5.33)
s	element coordinates
S_c	fracture stress [Pa]
S	initial loading slope [N m^{-1}]
$S(D)$	cumulative surface area of particles (smaller than size D) in a sample of fracture particulate [m^2]
S_n	total surface area of particles in a sample of particulate [m^2]
S_n / V_n	over all surface area of particles to volume [m^{-1}]
t_i	size distribution of oversize from classifier in the i -th interval
T	identity matrix
T	temperature in eq. (5.2) [$^{\circ}\text{C}$]
T_i	temperature at node i in eq. (2.45) [$^{\circ}\text{C}$]

T_j	temperature at node j in eq. (2.45) [$^{\circ}\text{C}$]
u	standard normal probability variable
u^e	vector of nodal displacements for element e
u_i	displacement vector for node point i
u_n	log-normal variate of the particle-size distribution by number
u_s	log-normal variate of the particle-size distribution by surface area
u_v	log-normal variate of the particle-size distribution by volume or mass
u_x	x - direction displacement degree of freedom
u_y	y - direction displacement degree of freedom
u_z	z - direction displacement degree of freedom
U	total strain energy [N-m]
U	upper triangular factorization of matrix K in eq. (A.22)
U_1	strain energy corresponding to initial crack length [N-m]
U_2	strain energy corresponding to final crack length [N-m]
v^e	element displacement vector
V	volume of particle in eq. (2.3) [m^3]
$V(D)$	cumulative volume of particles (less than size D) in a sample of fracture particulate [m^3]
V_n	total volume of particles in a sample of particulate [m^3]
W	width of sample [m]
W	energy required for crack surface formation in eq. (2.27) [J]
W_o	total input kinetic energy of impact [J]
W_o/V_n	overall energy density [J / m^3]
x	mean particle size [μm]
x	deflection due to the applied force in eq. (4.21) [m]
x	global coordinate in eq. (A.9)
x_{50}	median particle size [μm]
x'_G	parameter of the function $F(x) = (x/x'_G)^n$ [μm]

x_i	ratio of particle size in the i-th interval to particle size in j-th interval = (d_i / d_j)
x_m	mode of the distribution (= $c x_{50}$) [μm]
x'_R	parameter of the function $F(x) = 1 - \exp(-x/x'_R)^n$ [μm]
y	geometrical correction factor for the single edge notched turmeric sample piece [dimensionless]
y	global coordinate in eq.(A.9)
Y	column vector
Y	feed rate in eq. (5.3) [kg/h]
z	global coordinate
α	surface / volume shape factor (= a_s / a_v) [dimensionless]
α	material thermal diffusivity in eq. (A.13) [cm^2/sec]
α_o	indenter constant
α_{th}	thermal diffusivity [cm^2 / sec]
γ_A	specific surface energy [J / m^2]
γ_f	impact-strength parameter [J / m^2]
∂	displacement [m]
δa	incremental amount of extension of crack [μm]
Δa	incremental length of crack formed in eq.(2.28) [μm]
ΔT	temperature [$^{\circ}\text{C}$]
δL	change in length [m]
δu	incremental strain energy [N-m]
ε	energy efficiency factor [dimensionless]
ε^e	element strain vector
ε^o	vector of initial element strains
η_{EL}	elastic constant in eq. (2.35)
θ_x	x-direction rotational degree of freedom
θ_y	y-direction rotational degree of freedom
θ_z	z-direction rotational degree of freedom
θ^o	applied temperature difference
Φ^e	element shape function

ν	Poisson's ratio [dimensionless]
π	constant
ρ	material density [kg / m^3]
σ	applied stress [Pa]
σ	compressive stress in eq. (2.6) [Pa]
σ	tensile stress in eq. (4.11) [Pa]
σ	applied stress in eq. (5.1) [Pa]
σ	element stress vector of eq. (A.14) [Pa]
σ_{1c}	critical maximum principal stress in eq. (2.37) [Pa]
σ_g	ratio of 84% size to 50% size of the eq. $b = 1 / (2 \ln^2 \sigma_g)$ [dimensionless]
σ_g	geometric standard deviation of log normal particle-size distribution of fracture particulate in eq. (2.11)
σ_n	standard deviation, normal distribution
σ_{\max}	actual maximum stress [Pa]
σ_{nom}	nominal stress [Pa]
σ_{th}	theoretical fracture stress [Pa]
σ_{xx}	normal stress in the x-direction [Pa]
σ_{yy}	normal stress in the y-direction [Pa]
σ_{zz}	normal stress in the z-direction [Pa]
σ_{xy}	normal stress in the x-y plane [Pa]
σ_{xz}	normal stress in the x-z plane [Pa]
σ_{yz}	normal stress in the y-z plane [Pa]
ϕ	shape factor [dimensionless]
ϕ	temperature in eq. (2.44) [$^{\circ}\text{C}$]
μ	Poisson's ratio [dimensionless]
μ	mean of normal distribution in eq. (2.10)

Γ	fracture surface energy in eq. (2.22) [J / m ²]
ξ	parameter of the function $dF(x) = \xi \exp(-b \log_e^2(x/x_m)) dx$ (= $(b/\pi)^{1/2} \exp(-1/4b) / x_m$) [μm]
$\xi(a)$	function of $a = \sqrt{\text{crack length} / 2}$

Subscripts

i, j	sieve or interval numbers
N	total number of intervals

Aicher, S., Reinhardt, H.W.: Einfluss der Bauteilgroesse in Linearen und nichtlinearen Bruchmechanik, Holz Roh Werkst, 51, 215-220, 1993.

Allen, T.: Particle size measurement, 6th edition. (Chapman and Hall, London), 1997.

Anderson, T.L.: Fracture mechanics: fundamentals and applications, CRC Press, Florida, 1995.

Antunes, F.V., Ferreira, J.A.M., Beim, J.: Stress intensity factors based on the work of external forces, Int.J.Fracture, 98, 1-14, 1999

ASTM standard E 399, Standard test method for plane-strain fracture toughness of metallic materials, American Society for Testing and Materials, Philadelphia, 1995.

ASTM standard E 561-86, Standard practice for R curve determination, American Society for Testing and Materials, Philadelphia, 1995.

Atkinson, C., Craster, R.V.: Theoretical aspects of fracture mechanics, Prog. Aero.Sci. 31,1-12, 1995.

Austin, L.G., Trass, O.: Size reduction of solids: crushing and grinding equipment. In: Handbook of powder science and Technology, (Eds., Foyed M.E. and Otten, L.), Chapman and Hall, New York, 1997.

Bathe, K.J.: Finite element procedures in Engineering analysis, Prentice Hall Inc., Englewood Cliffs, New Jersey, 1996.

Bauermeister, J., Biller, E.: Die Zerkleinerung in der Verfahrenstechnik, Kakao und Zucker, 24 (11), 468-474, 1972.

Blumenauer, H., Pusch G.: Technische Bruchmechanik, Leipzig, VEB Deutscher Verlag fuer Grundstoffindustrie, Lipzig, Stuttgart, 1993.

Bourgeois, F., King, R.P., Herbst, J.A.: From single-particle fracture to complex size reduction processes, Presentation at SME Annual Meeting, Albuquerque, 1994.

Bridgewater, J.: Mixing, Powder Technology and Pharmaceutical Processes, (Eds., Chulia, D., Deleuil, M., and Pourcelot, Y.), Elsevier Science, Ch.10, 347-357, 1995.

Bridgewater, J.: Particle Technology, Chem.Eng.Sci. 50, (24), 4081-4089, 1995.

Brittain, H.G.: Particle size distribution, Part I: Representation of particle shape, size and distribution, Pharm.Tech. 38-45, 2000.

Buchen, G.D., Grewal, K.S., Robson, A. B.: Improved models of particle-size distribution: an illustration of model comparison techniques, Soil Sci.Soc.Am.J, 57,901-908, 1993.

Bush, M.B.: Simulation and contact induced fracture, Eng..Anal.Boundary Elements, 23, 59-66, 1999.

Carslaw, H.S., Jaeger, J.C.: Conduction of Heat in Solids, 2nd edition, Oxford University Press, London, 1996.

Cocks, A.C.F., Gill, S.P.A., Pan, J.: Modelling microstructure evolution in engineering materials, Adv. Appl. Mech. 36, 81-162, 1999.

Datta, A.K.: Heat and mass transfer in the microwave processing of food, Chem.Eng. Progress, June, 47-53, 1990.

DeBorst, R., Sluys, L.J., Muehlhaus, B., Famin, J.: Fundamental issues of finite element analysis of localization of deformation, Engg.Comput. 10, 99-121, 1993.

DeSavlo, G.J., Gorman, R.W.: Ansys Benutzerhandbuck, Band I and II Swanson Analysis Systems, Inc. Houston, Pennsylvania, U.S.A. 1989.

Dodds, J.A., Frances, C., Guigon, R., Thomas, A.: Investigations into fine grinding, Kona, 19, 113-124, 1995.

Dominique, C., Deleuil, M., Pourcelot, Y.: Powder Technology and Pharmaceutical processes, Elsevier Health Sciences, 1993.

Durnrn, T.F., Hogg, R.: Characterization of particle shape, Proceedings of International Symposium on Respirable dust in the mineral industries, SME, Littleton, CO, I, 283-288, 1990.

E.O.A. specification, Essential oil Association of USA. New York, No. 271, 1995.

- Erbe, M., Galanulis, K., Ritter, R., Steck, E.: Theoretical and experimental investigations of fracture by finite element and grating methods, *Eng. Frac. Mech.* 48, 103-118, 1994.
- Firus, S., Belter, A.: Energiesparende Zerkleinerung von Reisig, Rest- und Recyclingholz, *Wissenschaftliche Zeitung der Technischen Universität Dresden*, 48, 2, 96-101, 1999.
- Frank, M., Polke, R.F.: From the product and process requirements to the milling facility, *Powder Technology*, 105, 1, 2-13, 1999.
- Galai.: Operation manual of the computerized inspection system, CIS-100, Version 1.10, Galai Production Ltd., Haemark, Israel, 1994.
- Goepel, Schubert, H.: Zerkleinerung der Metallspäne, *Neue Huette*, 37, 3, 93-97, 1992.
- Govindarajan, V.S.: Turmeric, chemistry, technology and quality, *CRC Crit. Rev. Food Sci. Nutr.* 12, 199-301, 1990.
- Griffith, A.A.: The phenomena of rupture and flow in solids, *Phil. Trans. Royal Soc. A*, 221, 163-198, 1921.
- Griffith, A.A.: The theory of rupture, *Proceedings of the First International Congress for Applied Mechanics*, Delft, A, 1924.
- Gross, D. Hauger, W., Schnell, W., Wriggers, P.: *Technische Mechanik, Band 4; 3, Aufl;* Berlin u. Heidelberg, Springer-Verlag, 1999.
- Hawkins, A.E.: *The shape of powder-particles outlines*, Wiley, New York, comminution process, 1993.
- Herdan, G.: *Small particle statistics*, 2nd edn., Academic Press, New York, 1960.
- Hrsg., Pahl, M.H.: *Zerkleinerungstechnik Praxiswissen Verfahrenstechnik, Mechanische Verfahrenstechnik*, Verlag, TÜEV, Rheinland, 1991.
- Hutchinson, J.W., Evans, A.G.: Mechanics of materials: top-down approaches to fracture, *Acta Mater.* 48, 1, 125-135, 2000.
- Jia, C., Sun, D.W., Cao, C.W.: Mathematical simulation of temperature and moisture fields within a grain kernel during drying, *Drying Technology*, 18 (6), 1305-1325, 2000.
- Kachuru, C., Alam, R.: *Physio-chemical constituents and engineering properties of food crops*, Scientific Publishers, Jodhpur, 1994.

Kapur, P.C., Meloy, T.P.: Advances in size reduction: Fine and ultra grinding, Paper and course work material presented at the Powder and Bulk Solids Annual Conference, Chicago, Illinois, May 6-9, 1991.

Kaya, E., Hogg, R.: Control of particle characteristics in the production of fine powder by grinding, *Powder Technology*, 15 (2), 100-103, 1997.

Kaye, B.H.: The effect of shape of powder grains on the measured size distribution of a powder, *Powder Technology*, 15 (2), 83-87, 1997.

Kaye, B.H.: *Characterization of Powders and Aerosols*, John Wiley and Sons, 1999.

Khanna, N.M.: Turmeric: nature's precious gift, *Current Science*, 76 (10), 1351-1356, 1999.

Kirchner, J., Schubert, G., Jaeckel, H., Mueller, H.: Zerkleinerung von Metal/Kunststoff-Verbunden am Beispiel der Haushaltkleingeraete, *Chem-Ing.Techn.* 66, 9, 1199, 1994.

Kukla, R.J.: Understand your size reduction options, *Chem. Engg. Progress*, 5, 23-25, 1991.

Kumar, S.R.: *Characterization of particle shape*, M.S. thesis, Pennsylvania State University, 1996.

Lawn, B.R.: *Fracture of brittle solids*, 2nd edn., (Eds., Davis, E.A., Word, I.M.), Cambridge Solid State Science Series, 24-27, 1993.

Limpert, E., Stahel, W.A., Abbt, M.: Log normal distributions across sciences: Keys and clues, *Bioscience*, 51, 5, 341 – 352, 2000.

Max, B.: The essential pharmacology of herbs and spices, *Trends in Pharmacological Sciences*, 13, 15-20, 1992.

Meloy, T.P., Williams, M.C.: Single particle fracture model for slopes less than one, SME Annual Meeting, February, 14-17, Albuquerque, New Mexico, 1-4, 1994.

Mohsenin, N.N.: *Physical Properties of Plant and Animal Materials*, Vol.1, Structure, Physical Characteristics and Mechanical Properties, Gordon and Breach, London, 1986.

Morrissey, J.W., Rice, J.R.: Crack front waves, *Journal of the Mechanics and Physics of Solids*, 46, 471-487, 1998.

MSC-Pal 2.: Advanced stress and vibration analysis user's manual, The Mac Neal-Schwendler Corporation, Los Angeles, California, 1989.

Murakami, Y.: Stress intensity factors hand book, Committee on Fracture Mechanics, The Society of Material Science, Japan, Pergman Press, 1993.

Nash, W.A.: Schaum's outline of strength of materials, McGraw Hill, 4th edn., 1998.

Nussbaumer, M.: Buhler Diagram, 96, 19-24, 1990.

Ollett, A.L., Parker, R., Smith, A.C.: in Food Polymers, Gels and Colloids, edited by Dickinson, E (Royal Society of Chemistry, Cambridge), 537, 1991.

Otani, M., Minoshima, H., Uchiyama, T., Shinohara, K., Takayashiki, K., Ura, T.: The effect of particle shape on mechanical properties of powder bed, *J. Soc. Powder Technol., Jpn.* 32, 151-157, 1995.

Palmowski, L., Mueller, J., Schwedes, J.: Zerkleinerung Organische Feststoffe zur Erhoerung der Bioverfuegbarkeit, *Chem. Ing. Tech.* 72, 5, 483-487, 2000.

Perry, R.H., Green, D.W.: Perry's Chemical Engineers Handbook, 7th ed., McGraw Hill, New York, 20.11–20.13, 1997.

Peukert, W., Vogel, L.: Product Engineering am Beispiel des Zerkleinerns von Kunststoffen, *Chem. Ing. Tech.* 72, 9, 1022-1027, 2000.

Pradid., Moudgil., Brij, M., Kapur, P.C.: Particle science and technology in the 21st century, Special issue of *Int. J. of Mineral Processing*, 53 (1-2), 1-134, 1998.

Prasher, P.L.: Crushing and grinding process hand book, John Wiley and sons Ltd., New York, 1987.

Pruthi: Cryo milling – the latest technology of cold grinding of spices and condiments, Proceedings of symposium, AFST (I), New Delhi, 38, 1987.

Reichardt, Y.: Feinstzerkleinerung durch ein-und mehrfache Beanspruchung mit hohen Druck auf ein Gutbett, Ph.D Thesis, Universitaet Clausthal, 1994.

Rivas, E.O.: Food Powders: Part I, Characterization, Ch. 2.1-2.4, Aspen Publishers, U.S.A. 2001.

- Roberts, A. W.: Particle technology – reflections and horizons: an engineering perspective, *Trans. IChemE*, 76 A, 775-796, 1998.
- Rolland, T., Pons, M.N., Vivier, H., Thomas, A., Dodds, J.A., Guigon, P., Lecoq, O.: Quantitative analysis of particle shape during grinding, 5th World Congress of Chemical Engineering, 2nd Int. Particle technology forum, July, 14-18, San Diego, California, USA, Proceedings, Vol. V, 271-276, 1999.
- Ross, E., Seidenfuss, M., Kraaemer, D., Krolop, S., Eisele, U., Hindenlang, U.: Application and evaluation of different numerical methods for determining crack resistance curves, *Nuc. Eng.Design*, 130, 3, 1991.
- Rumpf, H.: Die einzelkorn zerkleinerung als Grundtechnischen zerkleinerung wissenschaft, *Chem.Ing.Tech.*, 37,3,187-202, 1965.
- Rumpf, H.: Physikalische aspekte der zerkleinerung, Aehnlichkeits gesetz der Bruchmechanik und Energieausnutzung der Einzelkorn zerkleinerung, *Aufbereitungs-Technik*, 14, 2, 59-71, 1973.
- Rumpf, H.: Particle technology (English edition), Powder Technology series, London, Chapman and Hall, 1990.
- San, B., Suo, Z., Yang, W.: A finite element method for simulating interface motion, I: Migration of phase and grain boundaries, *Acta Mater*, 45, 1907-1915, 1997.
- Salman, A.D., Gorham, D.A.: In Powder and Grains, 97, (Eds., Behringer, R., Jenkins, J), Balkema, 563-566, 1997.
- Salman, A.D., Gorham, D.A., Verba, A.: A study of solid particle failure under normal and oblique impact, *Wear*, 92-98,186-187, 1995.
- Schaub.: Zerkleinerung bei tieftemperaturen 2 teil, *Linde reports on Science and Technology*, 127-132, 1993.
- Schaub.: Feinmahlen mit dem cryogen kaltmahlverfahren, *Gasaktuel*, 45, 19-24, 1995.
- Schoenert, K.: Grundlagen zur Feinzerkleinerung, Preprints, GVC-Dezembertagung, Koeln, 1993.
- Schoenert, K.: Comminution from theory to practice, *Proc. 19th Int. Mineral Processing Congress*, San Francisco, Vol. 1, 7-14, 1995.

- Schoenert, K.: Comminution from theory to practice, Proc. 19th Int. Mineral Processing Congress, San Francisco, Vol. 1, 7-14, 1995.
- Schoenert, K.: Comminution, In: Comminution 94, (Ed., Forssberg, K.S.E), European symposium on comminution, Stockholm, 1994.
- Schoenert, K.: , Proc. 2nd Israel Conf. Conveying and Handling of Particulate Solids, Jerusalem, May, 1997.
- Schubert, G.: Zerkleinerungstechnik fuer das Recycling von Abfaellen und Schrotten, Freiburger Forschungsheft A 840, 12-32, 1997.
- Schubert, G., Hoberg, H.: Comminution techniques for the recycling of wastes, Proceedings SME Annual Meeting and Exhibition, February 24-27, Denver/Colorado, USA, 1997.
- Schubert, H.: Zur Energieausnutzung bei Zerkleinerungsprozessen, Aufbereitungs-Technik, 34,10, 495-505, 1993.
- Schwendig, G.: Versuche und betrachtungen zur Ueberwalzzerkleinerung einer mahlbettes, Aufbereit. Techn., 7, 489-492, 1966.
- Senna, M.: Finest grinding and mechanical activity of advanced materials, Proceedings 7th Europ. Symp. Comminution, 21-36, 1990.
- Seville, J., Tuzun, U., Roland, C.: Processing of particulate solids (Powder Technology Series), Chapman and Hall, 1997.
- Shen, M., Shen, M.H.: Direction of crack extension under general plane loading, Int. J. Mech. Min. Sci. and Geomech. 70 (1), 51-58, 1995.
- Smith, I., Chui, Y.H.: Factors affecting Mode I fracture energy of plantation-grown red pine, Wood Science and Technology, 28, 147-157, 1994.
- Steiss, M.: Mechanische Verfahrenstechnik, Band I, Springer-Verlag, Berlin, Heidelberg, New York, 1994.
- Strasser, S.: Aktueller Stand der Mahltechnik, KHD Symposium, 15-28, 1995.
- Szirtes, T., Rozsa, P.: Applied dimensional analysis and modeling, McGraw-Hill, 1997.
- Tada, H., Paris, P.C., Irwin, G.R.: The stress analysis of cracks hand book, 3rd ed., ASME Pres, American Society of Mech. Engrs. New York, 2000.

Theocaris, P.S.: Failure criteria for isotropic bodies revisited, *Engng. Fract. Mech.*, 51, 2, 239-264, 1995.

Thomas, P.P.: Spice exports, *Spice India* 13 (6), 10-11, 2000.

Timoshenko, S.P., Goodier, J.N.: *Theory of Elasticity*, 3rd Ed., McGraw-Hill, New York, 1987.

Tvergaard, V., Hutchinson, J.W.: The relation between crack growth resistance and fracture process parameters in elastic plastic bodies, *J. Mech. Phys. Solids*, 40, (6), 1377-1397, 1992.

Tvergaard, V.: Effect of void size difference on growth and cavitation instabilities, *J. Mech. Phys. Solids*, 44, (8), 1237-1253, 1996.

Viswanathan, K., Mani, B.P.: Theoretical expressions for the distribution function and experimental study of comminution kinetics, Paper presented at the Int. Conference on Recent advances in Particulate Science and Technology, Madras, Dec. 8-10, 339-343, 1992.

Wanibe, Y., Itoh, T.: New quantitative approach to powder technology, Ch.5, C.H.I.P.S., USA, 1999.

Weichert, R.: Anwendung von Fehlstellenstatistik und Bruchmechanik zur Beschreibung von Zerkleinerungsvorgaengen, *Zement-Kalk-Gips*, 45,1, 1-8, 1992.

Wigley, D.A.: *Mechanical properties of materials at low temperatures*, Plenum Pub. Corp., 1992.

Xia, S., Takezono, S., Tao, K.: A non local damage approach to the analysis of the fracture process zone, *Engg. Fracture Mechanics*, 48 (1), 41-51, 1994.

Zeng, K., Soderlund, E., Giannakopoulos, A.E., Rowcliffe, D.J.: Controlled indentation: A general approach to determine mechanical properties of brittle materials, *Acta Mater*, 44, 3, 1127-1141, 1996.

Zienkiewicz, O.C., Taylor, R.L.: *The Finite Element Method*, Butterworth, Heinemann, London, 2000.

Zimmermann, A., Carter, W.C., Fuller, E.R.: Damage evaluation during microcracking of brittle solids, *Acta Materlia*, 49, 127-137, 2001.

Zoga, P., Fetahu, K., Markollari, K.: Mass balance calculation for a complex grinding circuit, In: Changing scopes in Mineral Processing, (Ed., Kemal, M), Balkema, Rotterdam, 613-616, 1996.

Zwingelberg, H.: Moeglichkeiten und Grenzen beim Einsatz Prallmuehlen bei der Vermahlung von Weizen, Muehle + Mischfuttertechnik, 132, 21, 361-365, 1995.